University of Copenhagen

Niels Bohr Institute, Faculty of Science

Progress report concluding part A of the 4+4 Ph.D. program

Controlling the shape of subwavelength-diameter tapered optical fibers

Heidi Lundgaard Sørensen

August 2013

Academic supervisors:
Prof. Eugene S. Polzik
Assoc. Prof. Jürgen Appel

Master thesis

Heidi Lundgaard Sørensen

Controlling the shape of subwavelength-diameter tapered optical fibers

Towards a light-atom quantum interface

Danish National Research Foundation Centre for Quantum Optics (QUANTOP)
Niels Bohr Institute
Graduate School of Science
Faculty of Science
University of Copenhagen

Heidi Lundgaard Sørensen
Version 1.0 (disposition version),
Copenhagen, August 15, 2013

Principal academic supervisor:	Prof. Eugene S. Polzik
Additional academic supervisor:	Assoc. Prof. Jürgen Appel
Censor:	Prof. Ulrik L. Andersen
Thesis submitted:	15th of August 2013
Defence date:	20th of August 2013

Abstract

In this progress report we present a theoretical and experimental study of subwavelength-diameter tapered optical fibers. We have constructed an all-computer controlled heat-and-pull setup with which we can taper a standard optical fiber to a sub-micron waist size. The fiber diameter can thereby be decreased by a factor of 250 in a controlled way. The fibers are characterized according to their optical and spatial properties. The former are obtained by analyzing the transmission signal of light recorded during the pulling procedure, while the latter are carried out by analyzing CCD and SEM images of the fibers. To tailor the tapered fibers for specific applications it is important to have full control of the resultant fiber shape from the pulling procedure. We have therefore developed a model for the fiber shape consisting of the continuity equation of the fiber flow together with an axially varying fiber velocity profile dependent on the momentary fiber shape. While the continuity equation can be obtained from simple considerations of the fiber flow, the fluid dynamical properties of the fiber motion had to be analyzed to derive the velocity profile of the fiber. The model yields results in very good agreement with the measured fiber shape. By applying this model the fiber shape can thus be predicted for arbitrary pulling conditions.

Resume

I denne midtvejsrapport præsenterer vi et teoretisk og eksperimentelt studie af optiske fibrer hvis diameter er mindre end lysets bølgelængde. Til at fremstille dem har vi konstrueret en maskine der kan mindske diameteren af en fiber ved at trække i begge ender samtidig med at et lille område er opvarmet så det kan strækkes. Således kan vi på en kontrolleret måde trække en fiber til den er tyndere end en mikrometer, og dermed en faktor 250 mindre end til at starte med. De fremstillede fibrer er blevet karakteriseret både i forhold til deres optiske såvel som rumlige egenskaber. Førstnævnte er opnået ved at analysere lyssignalet gennem fibrerne detekteret under fremstillingen. Sidstnævnte er blevet udført ved at analysere billeder af fibrerne taget efterfølgende ved hjælp af et CCD kamera samt elektronmikroskopi. For at kunne specialfremstille fibrer til specifikke formål er det vigtigt at have fuld kontrol over den form de opnår under fremstillingen. Vi har derfor udarbejdet en model der kan beskrive denne resulterende form. Modellen består af en kontinuitetsligning for den flydende fiber samt en hastigheds profil af fiberen der afhænger af positionen langs fiber aksen samt fiberens øjeblikkelige form. Kontinuitetligningen kan udledes ved simple betragtninger af fiberens flydning. Derimod er det er nødvendigt at bruge fluid-dynamik til at analysere hvorledes fiberen flyder for at udlede hastighedsprofilen. Resultaterne fra modellen stemmer godt overens med den målte form af fiberen. Ved at anvende denne model kan formen af en fiber således forudsiges for vilkårlige fremstillings procedurer.

Publications

Peer reviewed

1. Stefan L. Christensen, Jean-baptiste Béguin, Heidi L. Sørensen, Eva Bookjans, Daniel Oblak, Jörg H. Müller, Jürgen Appel and Eugene S. Polzik.
"Toward quantum state tomography of a single polariton state of an atomic ensemble"
New Journal of Physics **15** (2013) 015002.

Contents

Chapter 1

Introduction

Ever since the sixties where Nobel laureate Charles K. Kau pioneered the field of optical fibers, they have been widely used due to their amazing properties as low loss light guides over long distances. Most known is perhaps their use in today's telecommunication schemes. Providing signals traveling with the speed of light optical fibers have significantly improved the field of information technology.

Figure 1.1: *Bundle of optical fibers.*

Recently, optical fibers have taken a step further up the ladder starting with the paper by [Tong *et al.* 2003]. Here it was demonstrated that low loss optical wave guiding can be maintained for optical fibers with a section drawn down to sub-wavelength diameters. At this section, called the nanofiber, a significant fraction of the light field transform into an evanescent wave exponentially decaying in the radial direction. During the past decade the properties and applications of nanofibers have been extensively explored and the fibers now play a main role in, for example, biosensing [Fan *et al.* 2008], single-mode lasing devices [Xiao *et al.* 2011], spectroscopy [Garcia-Fernandez *et al.* 2011], non-linear optics [Lee *et al.* 2012], optomechanics [Park *et al.* 2009], cavity optomechanics [Bahl *et al.* 2013], cavity quantum electrodynamics (cavity-QED) [Alton *et al.* 2010], and quantum optics with atomic ensembles [Vetsch *et al.* 2010; Goban *et al.* 2012]. Here, we will focus on the latter; nanofibers applied as a quantum interface for light-atom interactions.

Using nanofibers in the field of quantum optics is extremely interesting as it provides a strong coupling between light and atoms caused by the small mode volume of the evanescent light field. Atoms strongly coupled to a single spatial mode of a light field are a powerful tool in quantum science and can, for example, be used to realize the creation of highly non-classical states, a quantum memory for light, quantum entanglement, and quantum teleportation. Roughly speaking, there are two ways of how to obtain a strong coupling between light and atoms. Traditionally it is realized in cavity-QED experiments where single atoms or ions are trapped in a high finesse optical resonator allowing for many interactions with the same photons [Boozer *et al.* 2007; Wilk *et al.* 2007]. Another approach is to enhance the effective coupling by collective effects where many atoms interact with the light field simultaneously [Hammerer *et al.* 2010].

To establish an interface between light and atomic ensembles the atoms are typically trapped in a magneto-optical trap and thereafter transferred into a dipole trap. In [Ovchinnikov *et al.* 1991] it was first proposed to trap atoms near a dielectric-vacuum interface instead. This can be obtained by using the

dipole potential created by the evanescent light field of two laser beams inside the dielectric. Later, [Balykin *et al.* 2004; Le Kien *et al.* 2004] extended the idea and suggested using nanofibers as the dielectric. The scheme was experimentally realized in the groundbreaking work by [Vetsch *et al.* 2010]. Here it was shown that strong interactions are achievable by trapping atoms in a periodic dipole potential created by the evanescent field rising from two laser fields guided through a nanofiber. Using this technique a strong collective coupling with an optical density of approximately 10 was achieved with only a few thousand atoms. This is in stark contrast to trapped atoms in a far-off resonant optical dipole trap, where about 10^5 atoms are required to obtain the same order of magnitude for the optical depth [Appel *et al.* 2009].

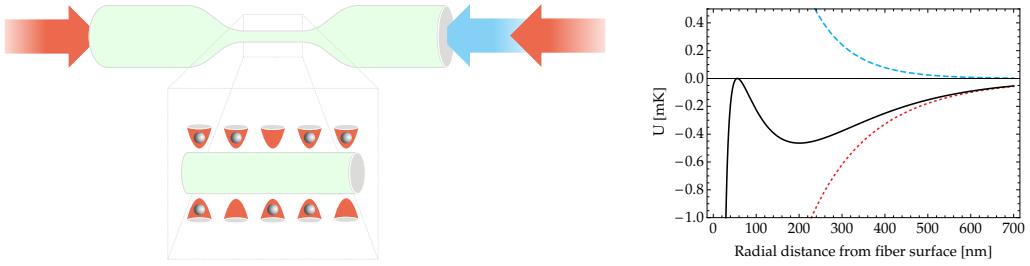

(a) (b)

Figure 1.2: *(a) Atomic nanofiber trap. (b) Black solid curve: Trapping potential along the x-direction at the axial position of an anti-node of the red-detuned standing wave. Blue dashed curve: Repulsive potential of the blue-detuned beam. Red dotted curve: Attractive potential provided by the red-detuned beam. (b) has been made by Jean-baptiste Béguin and shown here with his permission.*

In Fig. 1.2a a schematic drawing of the nanofiber is shown with the two-color trap configuration. One beam is red-detuned with respect to the atomic transition while the other is blue-detuned. Together with the van der Walls force the red-detuned beam provides an attractive potential for the atoms being strongest near the fiber surface, see Fig. 1.2b. To prevent the atoms from colliding into the fiber the blue-detuned beam is used to provide a repulsive potential. By choosing the red-detuned beam to be an x-polarized standing wave and the blue-detuned beam to be a y-polarized traveling wave this configuration effectively creates two 1D arrays of attractive potential wells at the antinodes of the red-detuned standing wave.

The above trapping scheme of an atomic ensemble along a nanofiber does not only provide a strong coupling for light-atom interactions. It also yields an all-integrated and scalable system of "fiber-coupled atoms". Optical fibers are already well integrated in today's telecommunication schemes. Having distributed stations of nanofibers with trapped atomic ensembles could be used to realize quantum information network over long distances [Cirac *et al.* 1997]. Together with the strong coupling provided by the nanofiber an integrated light-atom system is also an obvious candidate to use in hybrid systems. Here the atomic ensemble can be brought to interact with any other light interacting quantum system [Camerer *et al.* 2011].

However, before interesting research can be explored with these highly attractable nanofibers they have to be produced. This is thus the main objective in this thesis where the production and characterization of subwavelength-diameter tapered optical fibers are presented. Common for all applications using nanofibers is the required control of vital parameters such as the waist diameter and the tapered slopes. The work presented here provides a generalized model for the nanofiber

shape based upon the fiber fluid dynamical properties. This model can be used to design and optimize the specific fiber shape required for different applications.

This work

It is good custom to prepare the reader of what will be covered in a thesis. Here, we therefore list the main subjects:

- Description of the fiber pulling rig setup used to make nanofibers.
- Characterization of the optical properties of nanofibers using light transmission signals from both narrow- and broadband light sources as well as a frequency analysis of the former.
- Measurements of the fiber shape. This is important for future tailoring of the fiber shape, *e.g.*, to design the waist size and length, and to ensure adiabatic transitions between the ordinary fiber and the nanofiber.
- To model the fiber shape the fluid dynamics of the fiber pulling are analyzed. This results in two differential equations which can be solved numerically to yield the fiber shape. In order to do so, however, the viscosity profile of the fiber is needed. We have therefore developed a method to infer the viscosity using the stationary solution of the model.

Structure

The thesis is divided into two main parts; one describing the production and characterization of the fibers, and one deriving and analyzing the three models for the fiber shape. Below a chapter by chapter outline is given:

Chapter 1: Introduction to this work, motivation for working with nanofibers.

Chapter 2: A general introduction to step-index fibers and nanofibers is given, including a short recipe on how to make nanofibers as well as a description of the simple heat-and-pull model for the fiber shape.

Chapter 3: The fiber pulling rig is presented, and vital parts are described.

Chapter 4: The optical properties as well as the shape of the fibers are characterized.

Chapter 5: The simple heat-and-pull model is recapitalized and held up against the measured shape which it fails to reproduce. We conclude that the assumption of a linear velocity distribution of the fiber flow is not valid for our system.

Chapter 6: In the need of a more general model the fiber flow during the pulling procedure is considered. This results in the derivation of the continuity equation for the fiber shape. Afterwards the boundary conditions of the fiber flow are stated.

Chapter 7: From the continuity equation a recursion formula for an axially dependent but time-independent flow velocity profile is derived. The fiber shape is then modeled under the assumption of an axially dependent velocity profile stationary in time. The model performs better than the simple

heat-and-pull model and qualitatively reproduce the fiber shape. Quantitatively it fails, and we therefore conclude that the assumed time-independent fiber velocity profile is invalid.

Chapter 8: To model the fiber shape quantitatively the fluid dynamics of the fiber flow is included. The Navier-Stokes equations are solved in the limit of creeping flow of thin axisymmetric fibers. From this an axially- and shape-dependent velocity profile of the fiber flow is obtained. Together with the continuity equation from Ch. 6 the fiber shape is modeled showing good agreement with the measured data.

Chapter 9: A summary and conclusion of the presented work is given.

Chapter 10: Outlook of future implementations of the produced nanofibers.

Chapter 2

Optical fibers and nanofibers

In this chapter important concepts and variables are introduced in order to understand the properties of tapered optical nanofibers. It thereby provides the foundation of this work and will be referred to throughout the thesis. We start by briefly reviewing step-index optical fibers and their guided light modes. Afterwards a simple heat-and-pull model for making nanofibers is presented. For later analysis and characterization of the nanofibers the criteria of adiabatic taper transitions will be given in order to quantify the mode coupling between the ordinary fiber and the nanofiber. This is followed by a discussion of the guided modes in the nanofiber.

2.1 Step-index optical fibers

A step-index optical fiber is a long two-layered cylinder typically made of high-purity fused silica, *i.e.*, glass, see Fig. 2.1. The inner layer, denoted the core, is doped with germanium (Ge) to slightly increase the index of refraction n_{co} compared to the surrounding layer, the cladding, having index of refraction n_{cl}. In the frame of cylindrical coordinates, with basis vectors $\{\hat{\mathbf{e}}_\rho, \hat{\mathbf{e}}_\phi, \hat{\mathbf{e}}_z\}$, this is described as:

$$n(\rho) = \begin{cases} n_{\text{co}} & \text{if } \rho < a, \\ n_{\text{cl}} & \text{if } a < \rho < d, \\ n_0 & \text{if } d < \rho. \end{cases}$$

where $n_0 < n_{\text{cl}} < n_{\text{co}}$. From the principle of total internal reflection light can be guided in the core, confined by the core-cladding interface, see Fig. 2.2. If the angle θ of the internal light rays is smaller than the critical angle θ_{c}, light will leak out from the core into the cladding and be lost[1].

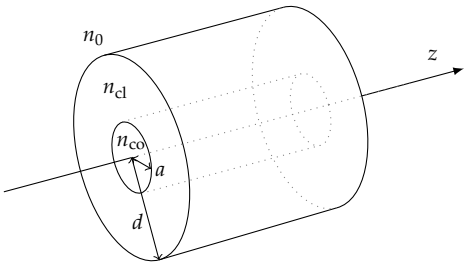

Figure 2.1: *Step-index fiber.*

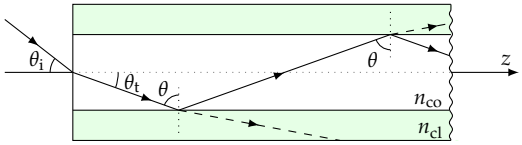

Figure 2.2: *Fiber longitudinal cross-section.*

By solving Maxwell's equations the propagating field modes can be calculated. This has been done in several textbooks and can be found in, *e.g.*, [Snyder *et al.* 1983] and [Ghatak *et al.* 1998]. Based on their work, the following will qualitatively cover the properties of fiber guided modes relevant for later discussions when characterizing

[1] The critical angle is found by Snell's law and given by; $\sin\theta_{\text{c}} = n_{\text{cl}}/n_{\text{co}}$ [Hecht 2002].

the nanofibers. Light will propagate in the core if the incident angle fulfills the inequality:

$$\sin\theta_{\mathrm{i}} \leq \sqrt{n_{\mathrm{co}}^2 - n_{\mathrm{cl}}^2}\,, \quad \text{for } n_0 = 1. \tag{2.1}$$

For step-index fibers; $n_{\mathrm{co}} \approx n_{\mathrm{cl}}$. Therefore only incident rays near parallel to the fiber axis will be sustained and the fibers are said to be weakly guiding. Within this regime the field can be assumed transverse to the fiber axis and its longitudinal components thus neglected. This yields approximative solutions to Maxwell's equations known as linearly polarized (LP_{lm}) modes.For each azimuthal index $l = 0, 1, 2, ...$ there exists a range of radial solutions $m = 1, 2, 3, ...$ corresponding to a discrete set of guided modes in the fiber. In Fig. 2.3 the intensity distribution for the four lowest order LP_{lm} modes is shown. The LP_{01} mode is seen to resemble a Gaussian distribution and therefore mainly this mode will be excited if the incident light is a Gaussian beam.

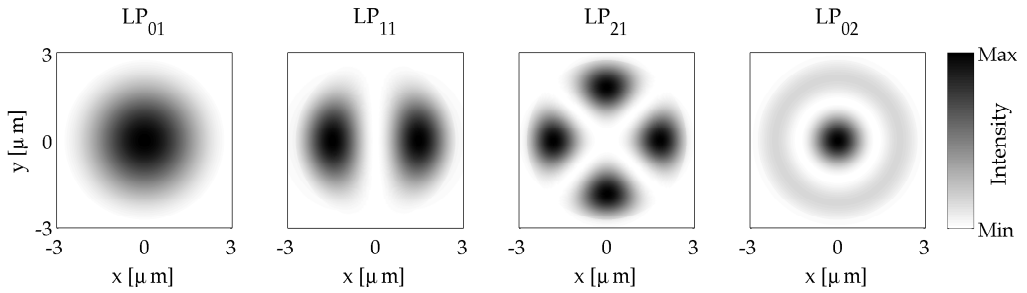

Figure 2.3: *Intensity distribution for the four lowest order LP_{lm} modes in a step-index fiber with parameters $2a = 5.5$ μm, $\lambda = 852$ nm, $n_{co} = 1.4650$, and $n_{co} = 1.4573$. The plot has been generated using open-source MATLAB code [Bojor 2005].*

Because of the different spatial distributions the modes are affected by the fiber boundaries differently. Therefore an unique axial propagation constant β exists for each mode defined such that the field mode can be written in the form [Cassany 2009]:

$$\mathbf{E}(\mathbf{r}) \propto \mathrm{e}^{-i\beta z}\,, \tag{2.2a}$$

$$n_{\mathrm{cl}} < \frac{\beta}{k_0} = n_{\mathrm{eff}} \leq n_{\mathrm{co}}\,. \tag{2.2b}$$

Here $\mathbf{E}(\mathbf{r}, t)$ is the electric field for a given mode at position $\mathbf{r}$, $\lambda = 2\pi/k_0$ is the free-space wavelength, and the effective index of refraction n_{eff} has been introduced as the normalized propagation constant. In Fig. 2.3 the LP_{01} mode is seen to be distributed around the core center. We therefore expect n_{eff} for this field mode to be closer to n_{co} than for any of the other modes. In Fig. 2.4 the different effective indices of refraction is plotted as a function of the V-number, also known as the waveguide parameter, given by:

$$V = \frac{2\pi a}{\lambda}\sqrt{n_{\mathrm{co}}^2 - n_{\mathrm{cl}}^2}\,. \tag{2.3}$$

We indeed see that n_{eff} for the LP_{01} mode, black solid line, is closer to n_{co} than the higher order modes. The V-number is related to the number of bound modes that can propagate in the fiber[2]. For $V < 2.405$, where the blue dashed line ends, the fiber is single-mode as only the LP_{01} mode can propagate in the fiber. This mode has no cut-off value and are thus said to be the fundamental mode in the fiber.

[2]For $V \gg 1$ the number of bound modes scales with V^2.

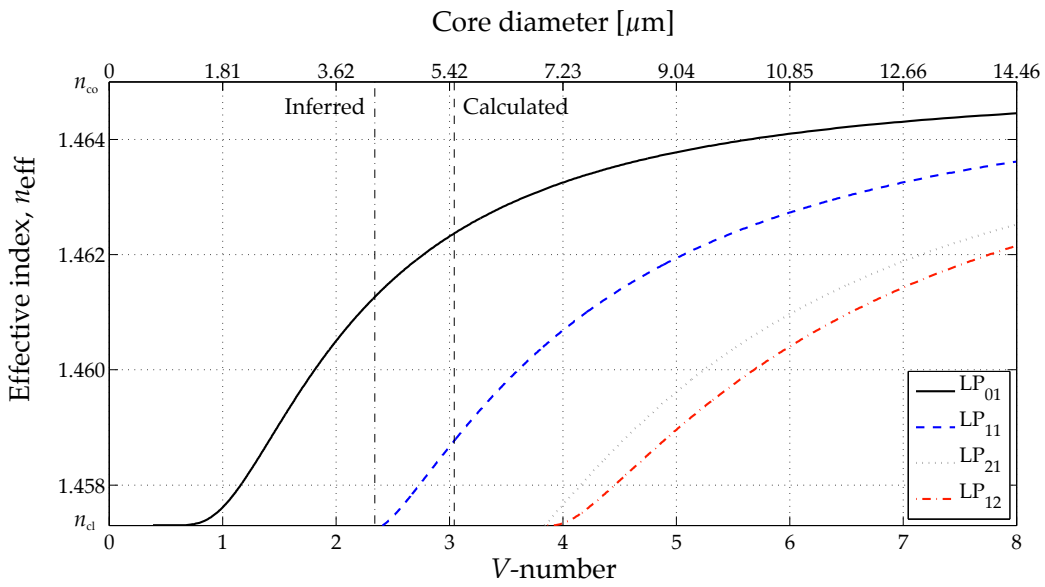

Figure 2.4: *Effective index of refraction for the four lowest order LP_{lm} modes as a function of the V-number (bottom axis) and core diameter (top axis) for $\lambda = 852$ nm. The vertical black dashed line indicates the calculated $V = 3.04$ for the fiber used in this work; $2a = 5.5$ μm, $\lambda = 852$ nm, $n_{co} = 1.4650$, and $n_{cl} = 1.4573$. The vertical black dashed-dotted line shows the inferred $V = 2.34$ and is located just below the single-mode cut-off at $V = 2.405$. The plot has been made with open-source MATLAB code [Karapetyan 2011].*

For the fiber used in this work we have calculated $V = 3.04$ for[3] $\lambda = 852$ nm. This is plotted as the vertical black dashed line, showing that the two lowest order modes, LP_{01} and LP_{11}, are sustained by the fiber. The two other modes plotted are cut-off at $V = 3.832$ since here the inequality in Eq. (2.2b) is no longer fulfilled. Although the V-number for our fiber predicts the single-mode cut-off to occur at $\lambda = 1077$ nm we have never observed the LP_{11} mode for $\lambda = 852$ nm. In Sec. 4.1.2 we show a spectrum plot of the transmission through the fiber from which we infer the single-mode cut-off to occur at $\lambda = 830$ nm. The fiber is therefore single-mode at $\lambda = 852$ nm with corresponding $V = 2.34$. This discrepancy is caused by the often used approximation for the fiber numerical aperture; $\mathrm{NA} = n_0 \sin(\theta_{\max}) \approx \sqrt{n_{\mathrm{co}}^2 - n_{\mathrm{cl}}^2}$, where $\theta_{\max}$ is the maximum angle of incidence for light rays fulfilling Eq. (2.1). This is generally valid for multi-mode fibers, but for single-mode fibers where diffraction effects can no longer be neglected, this approximation breaks down. For our fiber only the values for the measured numerical aperture and the index of refraction of the cladding n_{cl} are given, and we therefore obtained $V = 3.04$ by using the approximation for NA.

2.2 Simple heat-and-pull model

After reviewing step-index fibers we are ready to introduce the concept of tapered sub-wavelength diameter optical fibers, referred to as nanofibers. By heating a small section of an optical fiber and pulling the ends apart, as illustrated in Fig. 2.5, the fiber can be stretched and accordingly narrowed. The nanofiber is

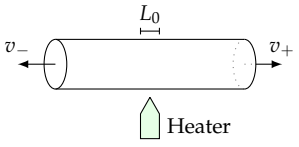

Figure 2.5: *The heater provides a uniform temperature of a small section with length L_0.*

[3] The 852 nm wavelength corresponds to the D2 line in caesium.

thus an integrated part of the original fiber connected by two tapered transitions.

The shape of the resulting fiber has been described in a simple heat-and-pull model developed by [Birks *et al.* 1992]. To avoid using involved fluid mechanics they impose two crucial constraints on the fiber pulling:

(i) The fiber is always heated uniformly.
(ii) The heated section is always cylindrical.

In general the temperature distribution of most heating devices, such as a flame or an open-sided oven, will be something resembling a Gaussian distribution, that is, having a peak-temperature near the center and decreasing outwards. Therefore (i) is mainly applicable for small heaters with a narrow temperature distributions that are better approximated with a box-shaped function than wide heaters. A uniform temperature distribution implies a uniform viscosity of the fiber. This means that the entire heated fiber section will be stretched according to a constant viscosity of the fiber, whereas fiber outside the section will be frozen. Note, that it is assumed that the fiber is heated sufficiently to stretch it, but not so much that it starts to deform under its own weight.

The simplest way to ensure (ii) is to pull the fiber-ends apart with equal and opposite speeds relative to the heater, *i.e.*, symmetrically elongate the fiber, such that $v_- = -v_+$ in Fig. 2.5. Assuming mass conservation of the pulled fiber also the volume will be conserved. This is well justified as evaporation of a molten glass fiber is low.

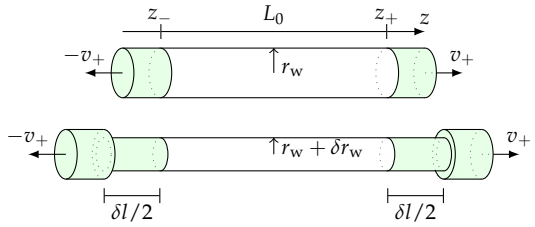

Figure 2.6: *Fiber symmetrically stretched by δl. The cylindrical shape is preserved when uniformly heated.*

The two constrains together with volume conservation means that the heated fiber shrinks uniformly over the hot zone[4] with length L_0, thereby preserving the initial cylindrical shape, as shown in Fig. 2.6. The change in radius δr_w for a given extension δl can be found by equating the fiber volume before and after the small pull:

$$\pi r_w^2 L_0 = \pi (r_w + \delta r_w)^2 (L_0 + \delta l)\,. \tag{2.4}$$

Taking the limit $\delta l \to 0$, and thus neglecting higher order terms, we arrive at the differential equation:

$$\frac{\mathrm{d}r_w}{\mathrm{d}l} = -\frac{r_w}{2L_0}\,. \tag{2.5}$$

The width of the hot zone may vary during the pull and thus be a function of the pull length l; $L_0 = L_0(l)$. However, in this work we exclusively apply the model by [Birks *et al.* 1992] for symmetric pulls; $v_- = -v_+$, where the hot zone is kept stationary; $L_0 =$ constant. The solution for the fiber waist radius are then readily found to be:

$$r_w(l) = r_0 \exp\left(-\frac{l}{2L_0}\right), \tag{2.6}$$

for the initial fiber radius $r_0 = r_w(0)$. In this limiting case the shape of the tapered transitions is also easily obtained. The radius $r(z)$, at a given point z on the fiber

[4]The heated section will be referred to as either the hot zone or the oven throughout the thesis.

taper after the pull, must be equal to the radius $r_w(l)$ when this point was pulled out of the hot zone. From this the fiber shape is found to[5]:

$$\frac{r(z)}{r_0} = \begin{cases} 1 & \text{for } z < \tilde{z}_-, \\ e^{-(z-\tilde{z}_-)/L_0} & \text{for } \tilde{z}_- < z < z_-, \\ e^{-l/(2L_0)} & \text{for } z_- < z < z_+, \\ e^{-(\tilde{z}_+ - z)/L_0} & \text{for } z_+ < z < \tilde{z}_+, \\ 1 & \text{for } \tilde{z}_+ < z. \end{cases} \tag{2.7}$$

The solution is shown graphically in Fig. 2.7 with marked limits $z_\pm$ and $\tilde{z}_\pm$, and different fiber sections labeled for future reference. The length of each exponential taper is given by half the total elongation length of the fiber. The waist is uniform within the length of the hot zone. It is clear that the solution exaggerates the shape of the fiber. In reality we do not expect the beginning of the taper transitions, at $\tilde{z}_\pm$, to be as sharp as predicted by the model, because of a more smooth temperature distribution.

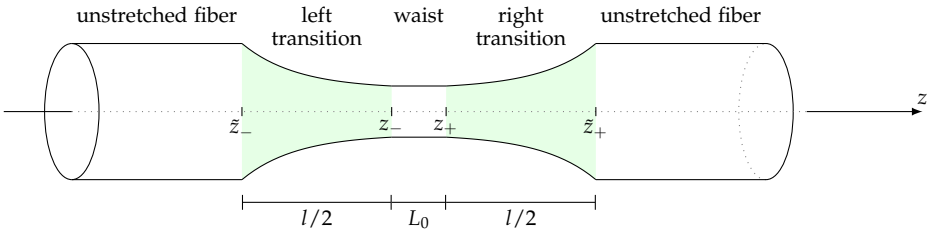

Figure 2.7: *Sketch of a nanofiber with exponential taper transitions predicted by the simple heat-and-pull model for symmetric pulls.*

The fiber shape model presented here has the big advantage that no fluid dynamics is required but it is limited to the special case where the temperature distribution of the heater is well approximated by a box-shaped profile. More general theories for the fiber shape, which include the fluid dynamics, do exist [Eggers *et al.* 1994; Baker *et al.* 2011] but for now it suffices to think of the fiber pulling in these simplified terms. However, we shall see later that the model by [Birks *et al.* 1992] does not describe the shape of our fibers made with a rather wide heater; $L_0 \approx 3$ mm. To model the fiber shapes we have therefore extended the existing theories by indirectly measure the axial profile of the fiber viscosity. This will be shown in Ch. 8.

2.2.1 Linear flow

To conclude the theory of the simple heat-and-pull model for the fiber shape we note that it predicts a linear velocity profile of the fiber along the z-axis during the pull. This will be important for the analysis carried out in Ch. 5–8. We consider a symmetric pull as shown in Fig. 2.8 where we have divided the fiber into small cylindrical blocks. The $N+1$ interfaces of the blocks inside the hot zone is labeled from left to right;

$$n = -\frac{N}{2}, -\left(\frac{N}{2}-1\right), ..., 0, ..., \left(\frac{N}{2}-1\right), \frac{N}{2} \tag{2.8}$$

for positive and even N. During a time Δt the fiber is symmetrically stretched by Δl. From the uniform viscosity and conserved volume assumptions we find that

[5] For more details the reader is referred to the paper by [Birks *et al.* 1992].

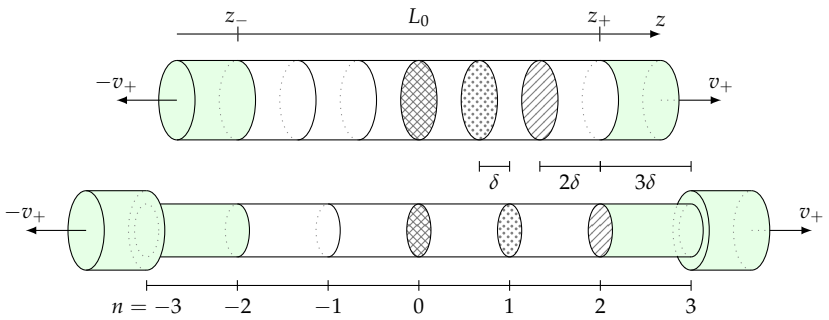

Figure 2.8: *Illustration of the fiber motion during a symmetric pull according to the simple heat-and-pull model, drawn for $N = 6$. In the center the velocity is zero and the disc at $n = 0$ do not move.*

each block gets evenly elongated by δ. The n'th interface has therefore moved a distance:

$$\Delta z_n = n\delta = n\frac{\Delta l}{N}\,. \tag{2.9}$$

Note, that the end-interfaces, $n = \pm N/2$, moved a distance $\Delta l/2$, from where $\delta = \Delta l/N$ is found. Eq. (2.9) leads to a linear velocity of the blocks:

$$v_n = \frac{\Delta z_n}{\Delta t} = \frac{n}{N}\frac{\Delta l}{\Delta t}\,. \tag{2.10}$$

Taking the limit $\Delta t \to 0$ we obtain:

$$v(z) = \begin{cases} -v_+ & \text{if } z \le z_-, \\ \frac{2v_+}{L_0}(z - z_c) & \text{if } z_- < z < z_+, \\ v_+ & \text{if } z_+ \le z, \end{cases}$$

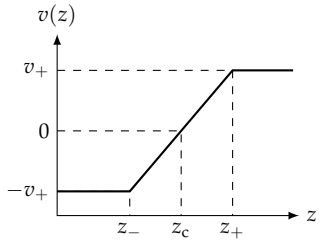

showing that the velocity of each fiber point along the fiber axis interpolates linearly between the end-velocities inside the hot zone. Here z_c denotes the center of the hot zone.

2.3 Tapered optical nanofibers

When the fiber is stretched and the tapers begin to form, it is no longer cylindrical symmetric. As we saw in Fig. 2.4 the field modes' effective index of refraction decreases with decreasing core radius. It therefore varies locally along the tapers. At some point it will become equal to the cladding index; $n_{\text{eff}} = n_{\text{cl}}$, and a core- to cladding-mode transition of the fundamental mode takes place [Love *et al.* 1991]. This happens at $V \approx 0.8$ for our fiber values, inferred from Fig. 2.4. For smaller radii the light will now be guided by the cladding-air interface instead of the core-cladding interface. Air can thus be considered as the cladding of the nanofiber, whereas the nanofiber core will be a weighted average of the untapered fiber core and cladding refractive indices; $\tilde{n}_{\text{co}} = 1.45732$.

To ensure a high coupling of the fundamental mode into the nanofiber it is physically intuitive that the tapers should only change gradually over the length scale of the taper. This is stated as the adiabatic criteria in the work by [Love *et al.* 1986] and more elaborately in [Love *et al.* 1991]. In the following we go through their results in order to establish a framework for understanding the light transmission through our produced nanofibers.

2.3.1 Adiabatic transition

Power loss from the fundamental mode can be assigned to the excitation of higher order cladding modes. If the taper transitions are axisymmetric, only modes with the same azimuthal symmetry can be excited; $LP_{01} \rightarrow LP_{0m}$, with the highest coupling to the nearest mode LP_{02}. This is intuitively what we would expect from examining Fig. 2.3 where we see that the LP_{01} mode has a high spatial overlap with the LP_{02} mode compared to the two other modes with $l > 1$. If the tapers are non-axisymmetric, *e.g.*, if the fiber is bending, coupling can also occur to modes with $l > 1$ and most likely to the lowest order modes with propagation constants closest to the fundamental mode, see Fig. 2.4.

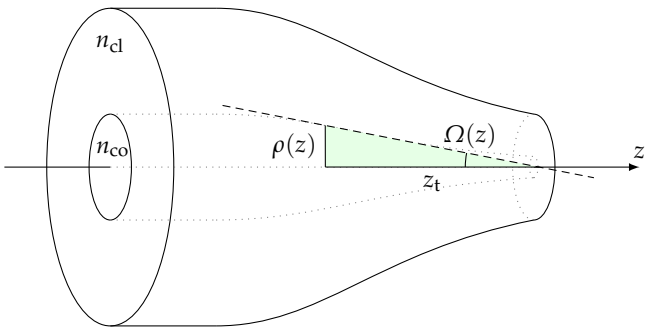

Figure 2.9: *Fiber taper. The dashed line is tangent of the core slope at point z where the local core radius is $\rho(z)$. The local taper angle $\Omega(z)$ it the angle between the tangent and the fiber axis. The local taper length z_t is given by the horizontal line in the green triangle spanned by $\rho(z)$, the tangent, and the fiber axis.*

In order to quantify a slowly varying taper transition we consider the relevant length scales of the taper, shown in Fig. 2.9. At point z the local taper angle is given by:

$$\Omega(z) = \arctan\left(\frac{\rho(z)}{z_t}\right) \approx \frac{\rho(z)}{z_t}, \tag{2.11}$$

for the local core radius $\rho(z)$ and the local taper length z_t. For adiabatic tapers; $\Omega(z) \ll 1$, and the approximation is justified. Excited higher order modes will interfere with the fundamental mode. To define a local coupling length between the modes the beat wavelength is used given by:

$$z_b = \frac{2\pi}{\beta_1(z) - \beta_i(z)}. \tag{2.12}$$

Here β_1 is the propagation constant for the fundamental mode and β_i the propagation constant for the i'th higher order mode. When the local taper length is long compared to the local coupling length; $z_t \gg z_b$, the mode can follow the surrounding variations in the boundary conditions with negligible coupling to other modes. The taper transitions are then said to be adiabatic as almost no power is lost from the fundamental mode. If instead; $z_t \ll z_b$, power will leak out from the fundamental mode to higher order modes that are now being excited. This is analogous to the single-slit diffraction experiment. Here geometrical optics is valid only when $\lambda \ll a$, for the characteristic length scale a of the slit. If $\lambda \gtrsim a$ diffraction effects occur and the wave nature of light has to be considered. Already for single-mode fibers, with core diameters ~ 10 μm, geometric optics is insufficient to describe the field and modal analysis is needed. Decreasing the core diameter makes the light mode-volume expand rather than compress due to diffraction effects, and part of the field mode will propagate in the cladding. If tapering happens on a short length scale the mode might get distorted and coupling to other modes occurs.

By equating the local taper length with the local coupling length; $z_b = z_t$, an upper bound can be placed on the local taper angle. This is used to quantify the adiabatic criteria and from Eq. (2.11) and Eq. (2.12) we obtain:

$$\Omega(z) \leq \frac{\rho(z)}{2\pi}\left(\beta_1(z) - \beta_i(z)\right). \tag{2.13}$$

In Fig. 2.10a the upper bound on $\Omega(z)$ as a function of the normalized core radius $\rho(z)/\rho_0$ is shown as the thick solid line[6]. Surprisingly, it is not a monotonically increasing function with the radius.

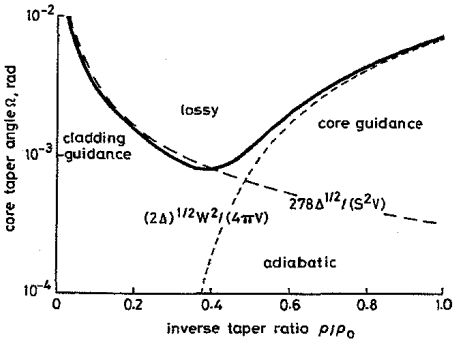

(a) Variation of the $\Omega(z)$ upper bound with the normalized core radius ρ/ρ_0, with $\rho_0 = a$. The plot is taken from [Love *et al.* 1991] and was calculated for $n_{cl}(\lambda) = 1.450588$, $n_{co}(\lambda) = 1.45376$, and $\lambda = 1.3$ μm.

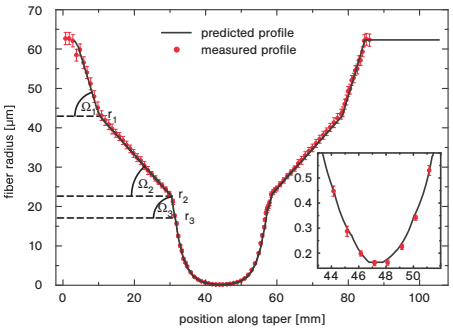

(b) Fiber radius as a function of the position along the fiber axis. Three linear sections are shown as an approximation of the optimal shape predicted by (a). This figure is taked from [Stiebeiner *et al.* 2010].

Figure 2.10: *The upper bound on the taper angle from the adiabatic criteria is shown in (a) from which fiber shape (b) can be optimized to ensure high coupling through the tapers.*

In fact, the taper section near the fiber waist can be as steep as that near the unstretched fiber. The observed minimum is close to the core- to cladding-mode transition for the fundamental mode. This is indicated by the two dashed lines which show the approximated solutions for the local taper angle at the limits; $\rho/\rho_0 \to 0, 1$, where the fundamental mode is guided by cladding-air and core-cladding interfaces respectively. For $\Omega(z)$ smaller than the solid line the tapers will be adiabatic.

The whole taper profile can of course be made with angles underneath the minimum. But this is a very impractical approach because it will produce long tapers exposing the un-coated fiber to environmental damages, such as scratching and dust particles. In most application it is therefore desired to have as short tapers as possible. From Fig. 2.10a we see that the optimal taper shape will be steep in both taper ends and flat in the center. In the group of Rauschenbeutel they have approximated this shape by three linear sections [Stiebeiner *et al.* 2010], as shown in Fig. 2.10b. Here transmissions above 70%, for a fiber waist radius of 160 nm, and for wavelengths in the range 470 to 690 nm were measured. In a later paper they report values for the transmission to be up to 98.7%, for $\lambda = 850$ nm and a waist radius of 250 nm, using the same fiber profile with three linear sections [Garcia-Fernandez *et al.* 2011].

[6]This plot is taken from [Love *et al.* 1991] and shows $\Omega(z)$ for their fiber parameters. For future optimizations of our nanofiber tapers we plan to calculate the curve ourselves with accordingly relevant parameters.

2.3.2 Guided modes

Until now we have described the light modes using the approximate linearly polarized (LP) modes. This was justified because the longitudinal component of the field is usually very small for normal step-index fibers, as explained in Sec. 2.1. When the fiber becomes sufficiently thin this is no longer an adequate description. Because of the now big differences in the core (=glass) and cladding (=air) refractive indices the fiber is no longer weakly guiding. The modes can therefore not be regarded as mainly transversal, and a significant z-component is now present. In order to understand the light-atom interactions it is therefore necessary to use the exact solutions of Maxwell's equations for the light description. Knowledge of the exact modes are also important in the analysis of the light transmission through the nanofiber when quantifying the adiabaticity of the transitions. In this section we therefore briefly present the exact modes in the nanofiber, again following the literature by [Snyder *et al.* 1983] and [Ghatak *et al.* 1998].

The exact solutions for the bound field modes are usually divided into two subgroups; hybrid modes and transverse modes. The hybrid modes contain both electric (E) and magnetic (H) field components along the fiber axis and are denoted HE (EH) when E_z is smaller (larger) than H_z. For the transverse modes, the longitudinal component of either the electric or magnetic field is zero and the modes are thus said to be transverse electric (TE) or transverse magnetic (TM).

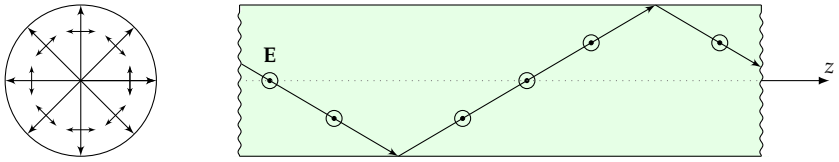

(a) TE_{01} mode. $E_\phi, H_\rho, H_z \neq 0$, $E_\rho = E_z = H_\phi = 0$.

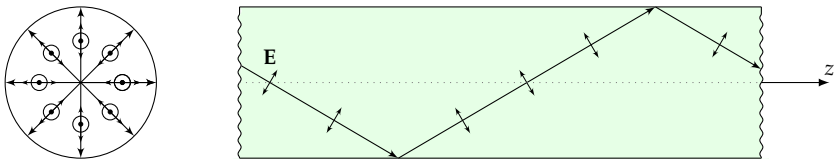

(b) TM_{01} mode. $E_\rho, E_z, H_\phi \neq 0$, $E_\phi = H_\rho = H_z = 0$.

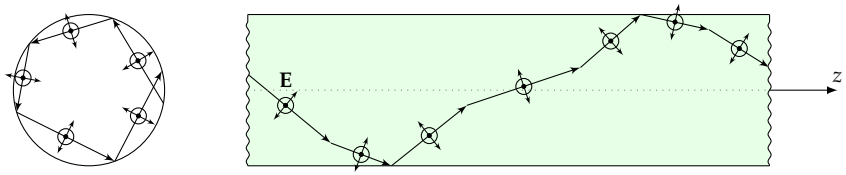

(c) Hybrid mode. $E_\rho, E_\phi, E_z, H_\rho, H_\phi, H_z \neq 0$.

Figure 2.11: *Propagating light rays in the fiber. The transverse cross-section of the fiber is shown to the left, while the longitudinal cross-section is shown to the right with a green background. Note that only the vertical light rays are shown in the longitudinal cross-section for (a) and (b), while several directions is contained in the transverse cross-section. Inspired by [Cassany 2009, Figs. 1.3 and 1.4], and [Snyder* et al. *1983, Fig. 11-2].*

To get a feeling for the nature of the exact modes it is helpful to consider the schematic light ray drawings shown in Fig. 2.11. The transverse modes always intersect the fiber axis effectively causing either the electric (a) or magnetic (b) field to be purely transverse. The TE_{01} only has circular fields lines for the electric field, while the TM_{01} electric field lines are perpendicular and parallel to the fiber axis. In contrary to the transverse modes the hybrid modes circulate around the

fiber axis without ever passing through it. This is what gives rise to the non-zero components of both the electric and magnetic field in all directions.

The LP modes are linear combinations of the exact modes and grouped according to:

$$\mathrm{LP}_{0m} : \mathrm{HE}_{1m} \tag{2.14a}$$
$$\mathrm{LP}_{1m} : \mathrm{HE}_{2m}\,,\ \mathrm{TE}_{0m}\,,\ \mathrm{TM}_{0m} \tag{2.14b}$$
$$\mathrm{LP}_{lm} : \mathrm{HE}_{l+1,m}\,,\ \mathrm{EH}_{l-1,m}\,, \quad \text{for } l \geq 2\,. \tag{2.14c}$$

As an example we consider Fig. 2.12. Here the TE_{01} and HE_{21} modes are combined to make the $\mathrm{LP}_{11} = \mathrm{TE}_{01} \pm \mathrm{HE}_{21}$ mode for two different spatial and polarization configurations. The green shaded regions indicate the intensity distribution similar to what was shown in Fig. 2.3. Two more polarization configurations exist for the LP_{11} mode[7]. These are obtained by combining the TM_{01} and HE_{21} modes and gives similar intensity distributions to the ones shown but with the polarization lines rotated by 90°. Like the LP modes each exact mode is described

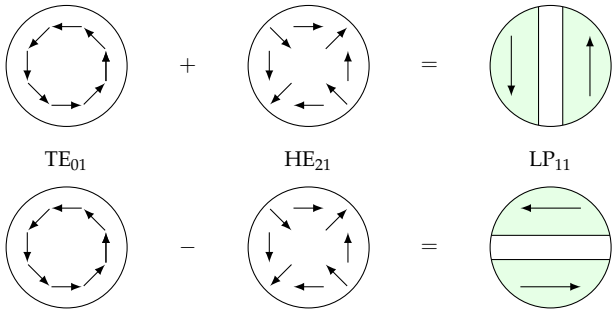

Figure 2.12: *Combining the TE_{01} and HE_{21} modes forms the LP_{11} mode for two different polarization and spatial configurations. Only the transverse polarization in the fiber cross-section is shown thus neglecting the z-component of the hybrid mode. Inspired by [Snyder* et al. *1983, Fig. 14-5(d)].*

by their propagation constant $\beta = k_0 n_{\mathrm{eff}}$. These are shown for some of the few lowest order modes as a function of the fiber diameter in Fig. 2.13. As in Fig. 2.4 the propagation constants monotonically increase with the fiber diameter. Only the HE_{11} mode can be guided by the nanofiber for arbitrary diameters and is thus (still) the fundamental mode. The modes can still be grouped according to the LP modes but are no longer degenerate, as evident when the cut-off point for the modes are considered, see Table 2.1. When analyzing the transmission through the nanofiber, in Sec. 4.1, it is therefore necessary to use the mode-drops of the exact modes rather than for the approximate LP modes.

[7] For all $l > 1$ modes there exist four independent combinations of the polarization and intensity distribution. For $l = 0$ modes only two independent combinations exist because of their circular symmetry.

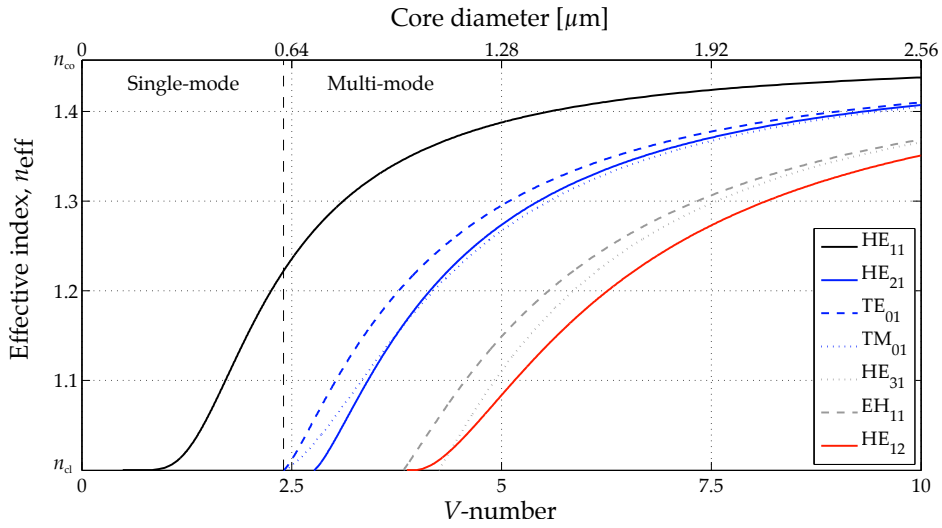

Figure 2.13: *Effective index of refraction of the exact fiber modes as a function of the V-number (bottom) nanofiber diameter (top) for $\lambda = 852$ nm. The plot is made using; $n_{cl} = n_{air} = 1$, and $n_{co} = \tilde{n}_{co} = 1.45732$ being the weighted average of the original core and cladding indices. The modes are color grouped according to the LP_{lm} modes; black: LP_{01}, blue: LP_{11}, gray: LP_{21}, and red: LP_{02}. The vertical black dashed line at $V = 2.405$ and $d_w = 0.615$ μm indicates the boundary between the fiber being single- or multi-mode.*

Table 2.1: *Few lowest order exact modes and their respective cut-off diameter for $\lambda = 852$ nm inferred from Fig. 2.13. The modes are grouped according to the LP modes.*

Exact modes	Approximate modes	Cut-off diameter [μm]
HE_{11}	LP_{01}	NaN
HE_{21} , TE_{01} , TM_{01}	LP_{11}	0.71, 0.62, 0.62
HE_{31} , EH_{11}	LP_{21}	1.09, 0.98
HE_{12}	LP_{02}	0.99

2.4 Summary

In the preceding sections we have introduced important concepts that will be applied throughout the thesis. We started by making a general description of step-index optical fibers, Sec. 2.1. From this the basic principles behind producing tapering optical nanofibers, using the heat-and-pull technique, were introduced as well as the fiber shape model by [Birks *et al.* 1992], Sec. 2.2. In this model a uniform temperature distribution of the fiber is assumed which gives a linear profile of the longitudinal velocity of the fiber during the pull, Sec. 2.2.1. This will become important later when a more generalized fiber shape model is developed. To ensure a high coupling between the ordinary fiber and the nanofiber the adiabatic criteria by [Love *et al.* 1986; Love *et al.* 1991] were stated as an upper bound on the taper slopes, Sec. 2.3.1. Finally, we reviewed the guided modes in the nanofiber. These depends on the geometry of the fiber and for $\lambda = 852$ nm the nanofiber becomes single-mode when the waist size is $d_w \leq 615$ nm, Sec. 2.3.2. From this we are now ready to explain in greater details how the nanofibers are produced. This is the subject of the next chapter.

Part I

Making and characterizing nanofibers

Chapter 3

Fiber pulling rig

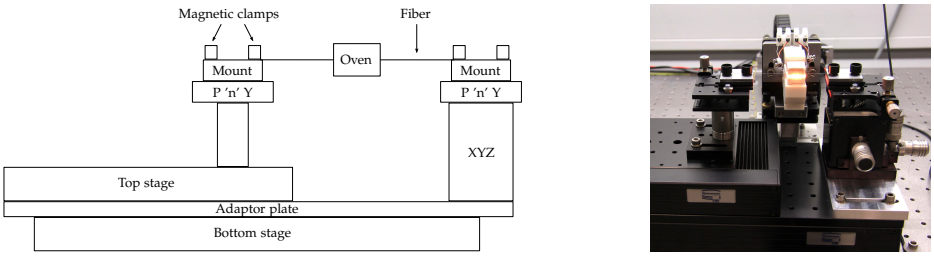

Figure 3.1: *Fiber pulling rig.*

To produce tapered optical fibers a simple heat-and-pull setup, shown in Fig. 3.1, has been build. The fiber is clamped down on two mounts placed on either side of an oven that provides localized melting of the fiber. Using two pitch and yaw translation stages (P 'n' Y) and a single XYZ linear translation stage a five-axis alignment is provided for the fiber. The two mounts are placed on a pair of stacked motorized translation stages. Here the bottom stage provides an overall translation of the fiber system with respect to the oven while the top stage effectively does the pulling. In the next sections each vital element in the fiber pulling rig will be discussed with emphasis put on the motorized stages and the oven as these elements are the heart of the fiber pull rig.

3.1 The stages

To perform the positioning and pulling of the fiber we use two motorized stages[1]. The stages are stacked on top of each other to be able to translate and position the fiber by only moving the bottom stage, instead of having to synchronously move both stages if they were placed in succession of each other. Another solution is to mount the oven on a translation stage moving along the fiber axis. However, stacking the stages is not only simpler it also improves the stability of the pulling procedure by preventing air currents to carry heat away from the oven [Warken *et al.* 2008]. The travel range for the bottom stage is 150 mm while it is 50 mm for the top stage.

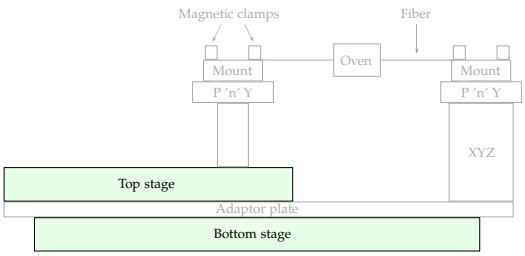

Figure 3.2: *Fiber pull rig with the motorized translation stages highlighted.*

[1] PMT-160-150-DC05-R and PMT-160-050-DC38-R from Steinmeyer FMD.

Both stages are driven by servo motors with a PID[2] controller[3] for the position and velocity of the stages. This is more precise than an open-loop control (used in stepper motors) because the measured position of the stages is being compared to the commanded position during the whole motion. From the specs the accuracy in position is ± 10 μm and the repeatability is ± 0.5 μm for both stages. The position is measured by an incremental rotary encoder from which two square waves in quadrature are being output. From the specs of the stages the conversion factors from encoder counts (cts) to millimeters for the bottom and top stage are given by:

$$c_\mathrm{b} = 2000 \text{ cts/mm}\,, \tag{3.1a}$$

$$c_\mathrm{t} = 290370 \text{ cts/mm}\,, \tag{3.1b}$$

respectively. It is crucial for the production and modeling of the fiber shape to know how much the fiber was pulled. We have therefore estimated the relative error on the stage calibration. For this the same CCD camera was used as for measuring the shape of the fiber (see Sec. 4.2 for more details on the CCD imaging). With the camera focused onto the top stage fiber mount an image was recorded. The bottom stage was then set to move x mm to the right and the top stage correspondingly to the left after which a second image was recorded. Unless both stages have the same systematic error in the positioning, the error on the conversion factors can be now estimated by comparing the overlap of the two images. These were found to differ by $\epsilon_\mathrm{p} \sim 37$ pixels. To get the error in mm we moved the bottom stage by $x_\mathrm{b} = 200$ cts $= 0.1$ mm and measured the pixel distance x_p between a point in the two images taken before and after this move. From this the pixel to millimeter conversion factor is estimated to be:

$$c_\mathrm{p} = \frac{x_\mathrm{p}}{x_\mathrm{b}} \approx \frac{(807 - 504) \text{ pixels}}{100\ \mu\text{m}} \approx 3.03 \text{ pixels}/\mu\text{m}\,. \tag{3.2}$$

For $x = 30$ mm we thus found the relative error of the stage calibration to be:

$$\epsilon = \frac{\epsilon_\mathrm{p}/c_\mathrm{p}}{x} = 3 \cdot 10^{-4}\,. \tag{3.3}$$

This is a very small error and even within this crude estimation we can safely use the conversions between encoder counts and millimeters as they are given in the specs for the two stages.

The stages come installed with electrical limit switches to ensure that they do not drive into the hard stop, *i.e.*, the end of the stage, which would mechanically damage the stages. Unfortunately, one of the limit switches in the bottom stage was misplaced from the factory and located too close to the hard stop. We have therefore additionally programmed software limit switches. If one of the stages enter the region between the software stop and hardware stop it is forced to stop and only allowed to move out of this region away from the hard stop. In order to work properly, the activated limit switch should not only stop the motion of the stage, but also set the deceleration to maximum to shorten the travel distance. This has therefore also been included in the software limit switch routine.

3.2 The oven

The fiber heating is a crucial ingredient in making tapered nanofibers, and a hot zone needs to be established. Here several options are available, *e.g.*, gas/liquid

[2] Proportional-integral-derivative.
[3] Galil DMC-2143.

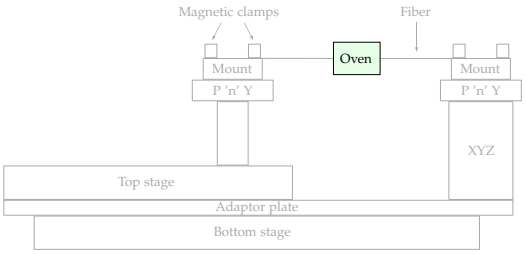

(a) Fiber pulling rig with the oven highlighted.

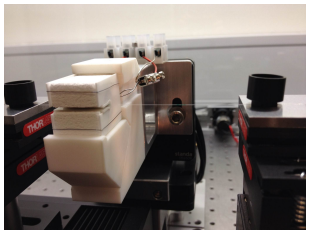

(b) Oven held in a mount made of MACOR®.

Figure 3.3: *Fiber pulling rig and the oven.*

burners, CO_2 laser beams and electrical heaters, just to mention a few [Tong *et al.* 2010]. Each of these heating devices has advantages and disadvantages in applicability and performance, and it is therefore necessary to weigh these against the desired parameters of the nanofiber (waist diameter, adiabaticity, *etc.*).

Hydrogen or a saturated hydrocarbon, such as butane or propane, supplied with oxygen is most commonly used as fuel for the flame produced by gas burners [Garcia-Fernandez *et al.* 2011; Kenny *et al.* 1991; Frawley *et al.* 2012; Brambilla *et al.* 2004; Graf *et al.* 2009]. Hydrogen constitutes a very clean flame with only water vapor resulting from the combustion, whereas hydrocarbons need to be mixed with plenty of oxygen to prevent making soot from incomplete combustion that would contaminate the fiber. The width of the flame is typically on the order of a few millimeters which makes it suitable for producing sub-micron fibers with a short waist. If a longer waist is needed the flame can be swept back and forth along the fiber, effectively increasing the hot zone length [Birks *et al.* 1992].

Flame-based heating devices work quite well in producing adiabatic fibers with reported light transmission of up to 98.7% of a 850 nm laser for a 500 nm diameter fiber [Garcia-Fernandez *et al.* 2011]. However, air currents can make the flame unstable as well as lift the fiber during the taper process. Effectively, this might change the hot zone length in an unpredictable way and was thus observed to reduce the fiber pulling reproducibility in the work by [Frawley *et al.* 2012]. A way to avoid this problem would be to heat the fiber using a CO_2 laser beam focused onto the fiber instead. As the fiber would now be directly heated by absorbing the laser radiation any issues regarding the cleanness of the fiber due to combustion is also removed. However, this method constitutes a lower limit on the attainable fiber diameter d as the radiative heating scales with the fiber volume, $\sim d^2$, while the convective cooling scales with the fiber surface area, $\sim d$. Therefore, a critical diameter exist for which the fiber cools faster than it heats [Grellier *et al.* 1998]. Of course, cranking up the laser power can lower this critical value but for as high power as 25 W only final diameters of 3-4 μm could be obtained in the group of Síle Nic Chormaic making this method highly impractical for producing submicron diameter fibers [Ward *et al.* 2006]. A solution to this was shown in [Sumetsky *et al.* 2004] where they surrounding the fiber by a sapphire tube and heated the latter with a CO_2 laser. This provided a furnace and the fiber could be indirectly heated, as when using a flame, making it possible to taper it to a submicron diameter.

An even simpler solution would be to use an electric heater as a micro-furnace [Shi *et al.* 2006; Ding *et al.* 2010; Lee *et al.* 2011; Fujiwara *et al.* 2011; Baker *et al.* 2011]. The temperature is set by controlling the current through a resistive load making it an easy-to-operate device. We have chosen to use an electric ceramic

micro-heater[4], denoted the oven, see Fig. 3.4. The resistive load is embedded in a $20 \times 19 \times 25$ mm^3 porous ceramic casing that can withstand high temperatures and via a 2 mm wide slit a fiber can be inserted into the oven center.

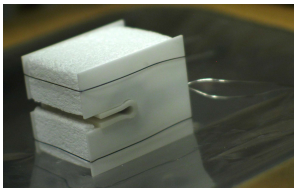

Figure 3.4: *The oven.*

To hold and position the oven we have designed a mount in collaboration with the mechanical workshop at the Niels Bohr Institute, see Fig. 3.3b. During the fiber pull it is important to keep the oven as stable as possible. Therefore we chose to make the mount of MACOR®. This material is mechanically stable up to 1000 °C since it has a low thermal expansion coefficient which makes it stay in shape during large temperature changes. Besides from this, MACOR® is also a very good electrical and thermal insulator effectively isolating the oven from the surrounding environment.

3.2.1 Heating the oven

When operating the oven care has to be taken because the heating element is very sensitive to sudden changes in the temperature. The current through the oven should therefore be ramped slowly when heating and cooling the oven. To ensure this we have programmed an ATmega168P microcontroller chip for measuring and controlling the oven current. We have also installed a battery[5] to prevent any fatal power failures.

In Fig. 3.5 a simplified circuit of the oven is shown, the full circuit diagram can be found in Appendix A. All the resistors have known values except from the

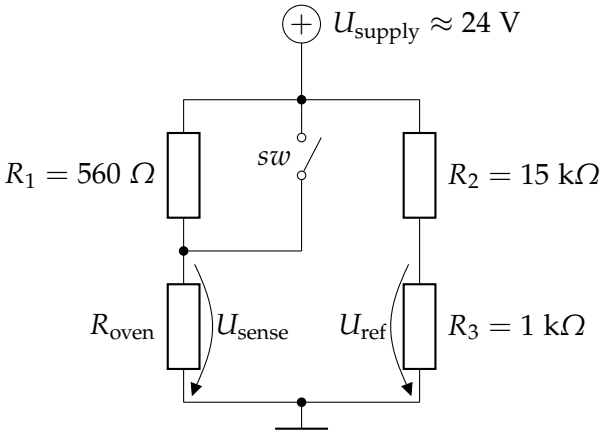

Figure 3.5: *Simplified circuit diagram of the oven. When the switch is connected the circuit is shorted to bypass R_1.*

oven resistance R_{oven} as this depends on the oven temperature. U_{supply} provides a nominally 24 V supply voltage and U_{sense} and U_{ref} measure the voltage drop over R_{oven} and R_3 respectively. From the circuit diagram we find the following important relations:

$$sw \text{ disconnected:} \qquad U_{\text{sense}} = \frac{R_{\text{oven}}}{R_1 + R_{\text{oven}}} U_{\text{supply}}\,, \tag{3.4a}$$

$$sw \text{ connected:} \qquad U_{\text{supply}} = R_{\text{oven}} I_{\text{oven}}\,, \tag{3.4b}$$

$$U_{\text{ref}} = \frac{R_3}{R_2 + R_3} U_{\text{supply}}\,. \tag{3.4c}$$

[4]Ceramic micro heater, CMH-7019 from NTT Advanced Technology Corporation.
[5]SITOP power battery module 24 V/12 Ah from SIEMENS.

Where I_{oven} is the current through the oven. In order to measure U_{supply} and U_{sense} an analog-to-digital converter (ADC) on the microcontroller is used as shown in Fig. 3.6. Although the nominal voltage of U_{supply} is known in principle it is still measured in order to have a more precise value, which is important for controlling I_{oven}. This would be particularly crucial if a power failure occurs. In this case the system automatically switch to the battery supply voltage which could differ significantly from U_{supply}.

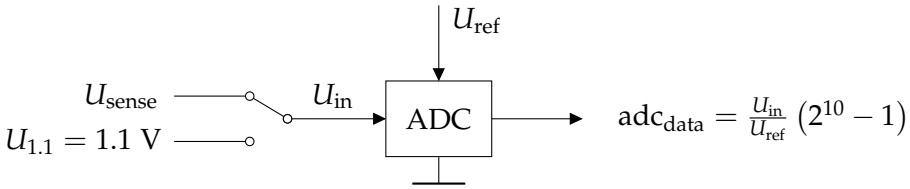

Figure 3.6: *Simplified circuit diagram for the analog-to-digital conversion used to measure U_{supply} and U_{sense}.*

The output of the ADC, adc_{data}, is given as the ratio of an input voltage U_{in} to a reference voltage U_{ref} stored as a 10-bit value. After every second ADC measurement the switch in Fig. 3.6 is changed thereby changing the input U_{in} such that we alternate between measuring U_{sense} and $U_{1.1}$. Combining this with Eq. (3.4) we find:

$$R_{\text{oven}} = \frac{R_1}{r\left(\frac{2^{10}-1}{\text{adc}_{\text{sense}}}\right) - 1}\,, \tag{3.5a}$$

$$U_{\text{supply}} = r\left(\frac{2^{10}-1}{\text{adc}_{1.1}}\right) U_{1.1}\,. \tag{3.5b}$$

The oven heating power is controlled by pulse-width modulation with a switching frequency of 400 Hz. In each cycle of period $T = 2.5$ ms current is supplied to

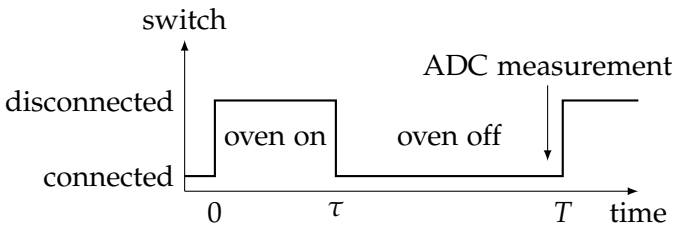

Figure 3.7: *Timing diagram of the oven current control and the ADC measurements.*

the oven during a time τ by closing *sw* in Fig. 3.5. Rather than measuring the instantaneous current through the oven we thus measure the average current given by:

$$\langle I_{\text{oven}} \rangle_T = \frac{U_{\text{supply}}}{R_{\text{oven}}} \frac{\tau}{T}\,, \tag{3.6}$$

and controlled by setting the length of the duty cycle $T_{\text{duty}} = \tau/T$. In the off time, $T - \tau$, the switch is disconnected and the ADC measurement of either U_{sense} or $U_{1.1}$ is performed.

The recommended heating rate of the oven is 0.1 A/min. In a slow 6 s loop the current is therefore increased (decreased) in steps of $\delta I = \pm 10$ mA until a target current I_{target} is reached, see Fig. 3.8. In the mean time a fast loop, set by T, measures U_{supply} and R_{oven} as described above such that T_{duty} can be adjusted accordingly.

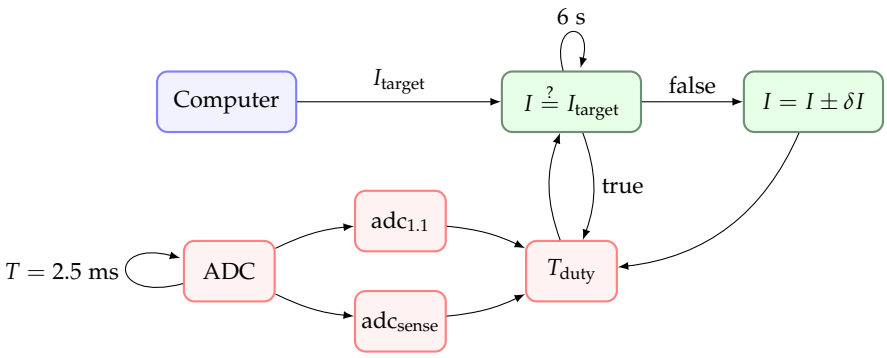

Figure 3.8: *Diagram of the oven current control. When operating the oven in power-mode the same diagram is used with all $I \rightarrow P$.*

Combining Ohm's law with Joule's heating law the power dissipated in the oven is given as; $P_{\text{oven}} = U^2_{\text{supply}}/R_{\text{oven}} = I^2_{\text{oven}}R_{\text{oven}}$. The dissipated power scales directly with the heat transferred to the oven. We have therefore chosen to control P_{oven} in steps of $\delta P = \delta I^2 R_{\text{oven}}$ rather than the current. This is not only more sensitive due to the square relation between the power and the current, but it also provides a more intuitive measure of the oven as the dissipated power is directly linked to the oven temperature.

3.2.2 Moving the oven

As mentioned in the previous section the oven needs to be heated and cooled slowly in order not to damage the heating element. For the temperature required to melt the fiber sufficiently enough to be tapered and not slip underneath the clamps it takes about 40 minutes to reach the operating power of 100 W. To speed up the production rate the oven is therefore placed on a motorized rail clamped down on the optical table, see Fig. 3.9. With this the hot oven can be driven away from the fiber pulling rig at a safe distance isolated from the rest of the setup. This enables us to both image the fiber right after the pulling procedure (more on this in Sec. 4.2), and to prepare and insert a new fiber rather fast in the pulling rig between consecutive pulls without having to turn on and off the oven.

Besides the apparent practical purpose of being able to move the oven in and out of the setup the oven-mover also provides a major advantage with respect to the reproducibility of the pulled fiber shapes. The fiber shapes depend inherently on the temperature distribution of the hot zone and it is therefore important to have the oven positioned at exactly the same point for consecutive pulls. The oven-mover is therefore designed to run into a hard stop instead of a programmed software stop. To avoid backlash of the oven, which occurs when turning the motor off, we keep driving the motor at a low current thus pushing and keeping the mover at the same position at the hard stop. Everything is controlled using a second microcontroller connected to the stages encoder via I/O ports, such that the mover is controlled by the same program that we use for the stages.

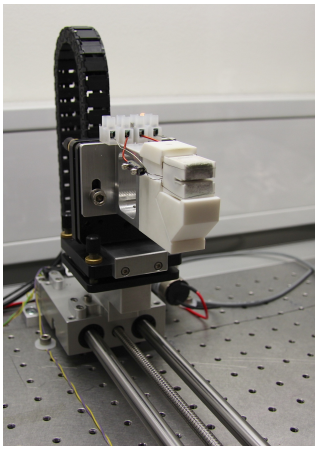

Figure 3.9: *Oven mounted on a motorized rail.*

3.3 The fiber

We use a single-mode step-index fiber[6] as described in Sec. 2.1. The fiber has a 5.5 ± 0.5 μm diameter core and a 125 ± 2 μm diameter cladding with refractive indices $n_{co} = 1.465$ and $n_{cl} = 1.4573$ respectively. The fiber is coated with a buffer of acrylate polymer to protect it from moisture and scratching. Before pulling the fiber roughly 6 cm of the buffer is stripped off. It is then cleaned with ethanol and inserted into the fiber pulling rig.

3.4 The fiber mounts and alignment

To keep the fiber in place during the pull process we attach each end of it onto a fiber mount[7], see Fig. 3.10. Here the fiber is clamped down in V-shaped grooves by using strong rubber padded magnets. It is important to clean the grooves before placing the fiber, as we have observed that any dirt in the grooves might give rise to a transverse tension in the fiber causing it to bend.

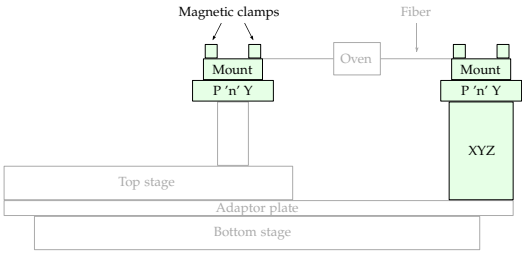

Figure 3.10: *Fiber pulling rig with the mounts and translation stages highlighted.*

Both mounts are placed on top of analog pitch-and-yaw stages[8] and one of these is additionally mounted on an XYZ translation stage. The fiber is aligned such that the tension in it is mainly along the fiber axis, *i.e.*, the V-grooves are made to be both parallel and in level. This is important to ensure axisymmetric fiber tapers necessary for adiabatic coupling between the ordinary fiber and the nanofiber.

3.5 The flowbox

The fiber pulling rig is placed inside a flowbox[9] to keep the setup in a dust free environment. This is extremely important as any dust particle on the nanofiber surface will act as a scatterer and/or absorber of the evanescent light field and thus effectively decrease the light transmittance. It has been suggested that the degree of humidity might also affect the nanofiber lifetime, as the water adsorption onto the fiber might induce cracks [Brambilla 2010]. However, in the work done by [Fujiwara *et al.* 2011] it was shown that the degradation of the fiber is mainly due to dust particles while the effect from the humidity level was within the uncertainty of the measured light transmittance and thus negligible. They also found that the degree of transmission degradation due to dust particles is severely high in a normal laboratory environment. For a 460 nm waist nanofiber they measured the transmittance to drop by 40% already after only 4 hours and after 10 hours the transmittance was below 20%. While in a class 10 clean-room they measured no deterioration of the transmittance over one week within a relative noise level of ± 0.02.

[6] LIEKKI™ Passive-6/125.
[7] Thorlabs HFV001.
[8] Thorlabs APY001.
[9] Schilling Engineering® RF-LFBV-1990-AL-ME.

3.6 Summary

In this chapter we have presented vital parts of the fiber pulling rig used to produce tapered optical fibers. The pulling is based on the simple principle of heating and melting a small section of the fiber while pulling its ends apart. Using two stacked motorized stages stable and reproducible pulling is provided. To heat the fiber we have chosen to use an electric ceramic micro-heater since it is a stable and easy-to-operate device. The drawback is, however, that the temperature distribution provided by the heater is not well-approximated by a box-shaped profile as will become evident in Ch. 5. This means that a flow model generalized to all axial positions and times is needed in order to predict the fiber shape from given boundary conditions. Such a model is developed in Ch. 8. The oven is held very stable using a special designed mount made of MACOR®. Placing it on a motorized rail the oven can thus be reproducible positioned at the same location for every pull. The temperature provided by the oven is set by controlling the dissipated power in the resistive heater using a microcontroller. Here special safety has to be taken to prevent abrupt changes of the temperature. Therefore a battery has been connected to the oven circuit and the microcontroller programmed such that the oven will switch to battery voltage supply in the event of a power failure. It has been shown that the fiber is mounted such that a five-axis alignment is provided to ensure minimal transverse tension in the fiber during the pull. Tapered fibers are very sensitive to dust particles and the whole pull rig is therefore placed inside a flowbox providing vertical laminar flow of clean air to prevent any dust to stick to the fiber. With this fiber pulling rig we can produce subwavelength diameter tapered optical fibers. This is shown in the next chapter where some of the main properties of the produced nanofibers will be characterized.

Chapter 4

Characterizing the fiber

When using a nanofiber as light-atom quantum interface several things have to be taken into account. First, the nanofiber has to be thin enough to have a sufficient evanescent light field for trapping and probing the atoms, and the waist should be long in order to trap as many atoms as possible. Secondly, the tapered fiber transitions should be gradual to obtain a high light transmission through the nanofiber. Finally, the spatial light modes should be controllable and often only consist of the fundamental mode. Common for all three is the importance of the tapered fiber shape. This chapter is devoted to the characterization of the fiber properties such that the above criteria can be ensured. We start by quantifying the adiabaticity of the fiber. This is done by measuring and analyzing the light transmission through the fiber while pulling. Here we will see how different spatial modes can be identified. In the last two sections the fiber shape will be characterized both by CCD imaging and by scanning electron microscopy.

4.1 Light transmission

To quantify the adiabaticity we measure the light transmission of a 852 nm single-mode external cavity diode laser[1] while pulling the fiber, see Fig. 4.1. At the fiber end-faces light can either be transmitted or reflected[2]. This effectively makes the fiber behave as an optical resonator and introduces length sensitive oscillations in the transmitted light signal due to interference. To reduce this noise we angle-polished one of the fiber end-faces thereby decreasing the reflection. This gives a significant improvement of the transmission quality reducing the fluctuations from about 10% to 1%.

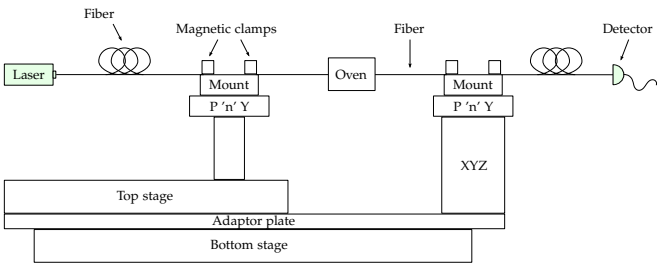

Figure 4.1: *Fiber pulling rig with the laser and photodetector highlighted.*

In Fig. 4.2 a typical transmission signal during a symmetric pull is shown[3]. After elongating the fiber by about 7 mm the detected power starts to oscillate with an increasing frequency. This indicates that cladding modes are being exited

[1] Axcel Photonics M9-852-0150-S50.

[2] Rougly 4% of light gets reflected at a glass-air interface.

[3] By sending an output compare pulse from the stages encoder to the same USB data acquisition device (LabJack U3-HV) used to collect the detected light signal, we obtain the transmission as a function of the elongation length instead of time.

as explained in Sec. 2.3.1. The fiber is then no longer single-mode and beating between the modes occurs. The constructive interference reaches near 100%

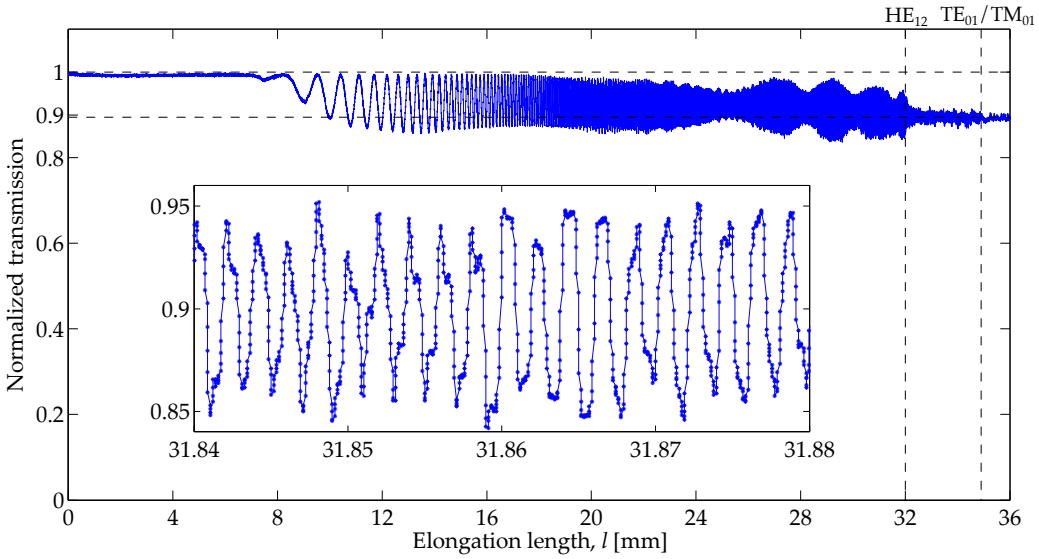

Figure 4.2: *Normalized transmission signal through the fiber as a function of the fiber elongation length. The signal was obtained with a* 2.5 kHz *sampling rate during a symmetric pull with speeds* $v_{\pm} = \pm 50$ μm/s. *The elongation length was triggered every* 25 μm. *The two vertical dashed lines indicate the measured mode-drops at* 32.0 mm *and* 34.9 mm. *The inset shows a zoom of the transmission near the first mode drop and the oscillations are seen to be well resolved.*

transmission for elongation lengths up to 29 mm. After this point it starts to decrease slightly and at 32 mm a big drop in the oscillation amplitude is observed. Later a smaller drop is seen at 34.9 mm. Both drops are indicated by vertical dashed lines. In Fig. 2.13 we saw that the support of higher order modes in the nanofiber depends on the diameter and in Table 2.1 we listed the cut-off diameter for the six lowest order modes. We therefore infer the drops to be caused by the loss of two higher order modes exited in the fiber at the tapered transitions. From Sec. 2.3.1 we know that the fundamental mode HE_{11} in the fiber most likely will excite the HE_{12} mode due to their high spatial overlap. We therefore attribute the strong mode-drop at 32 mm to be the loss of this mode. The TE_{01} and TM_{01} modes are the longest living higher order modes and their azimuthal index l only differs by one from the fundamental mode. The last weaker mode-drop is thus inferred to be the loss of both or either one of these modes. Therefore the fiber tapers must be non-axisymmetric because modes with azimuthal index different from the fundamental mode cannot otherwise be exited. In Sec. 4.3 the fibers are observed to bend when pulled to very small diameters supporting the inferred excitation of the TE_{01} and TM_{01} modes.

From the above analysis we are lead to conclude that the fiber tapers are non-adiabatic for symmetric pulls. No other severe loss mechanisms, such as dust particles or cracks in the fiber, seem to be present as the signal oscillates around the final transmission of 90% throughout the pull. This is further supported by the fact that transmission signals for symmetric pulls always display the same signatures as here, *i.e.*, increased oscillations during the pull and mode-drops near $l = 32$ mm and $l = 35$ mm consistently causing about 10% loss. If there would be losses caused by environmental influences they should be random in character and expected to give a different transmission signal with different degree of loss. According to the adiabatic criteria it should therefore be possible to minimize the losses by optimizing the taper shapes.

4.1.1 Gabor transform

To confirm the inferred mode-drops in the transmission, Fig. 4.2, it is helpful to do a frequency analysis of the signal. This can be done by performing a short-time Fourier transform of the signal $T(z)$ with a Gaussian window, a so-called Gabor transform [Ding *et al.* 2010]:

$$G(l,k) = \int_{-\infty}^{\infty} \mathrm{e}^{-\alpha(l-z)^2} \mathrm{e}^{ikz}\, T(z)\, \mathrm{d}z\,, \tag{4.1}$$

where the free parameter α adjusts the resolution, l is the fiber elongation length, and k the beat wavenumber. The Gabor transform is here written in terms of the pull length and wavenumber equivalent to time and frequency[4]. The short-time Fourier analysis is used instead of the conventional Fourier transform because the frequency components change during the pull. The Gabor transform shows which frequency components are present at a given time and, more importantly for our application, when they die out, that is, when the nanofiber becomes single-mode.

In Fig. 4.3 the Gabor transform of the transmission signal in Fig. 4.2 is shown. Two frequency components arise at elongation lengths of about 15 mm and 20 mm. The first component suddenly vanishes at 32.0 mm, while the second component splits into two and then vanishes at 33.8 mm and 34.9 mm respectively. Furthermore, a fourth component appears at $l = 28$ mm and thereafter vanishes

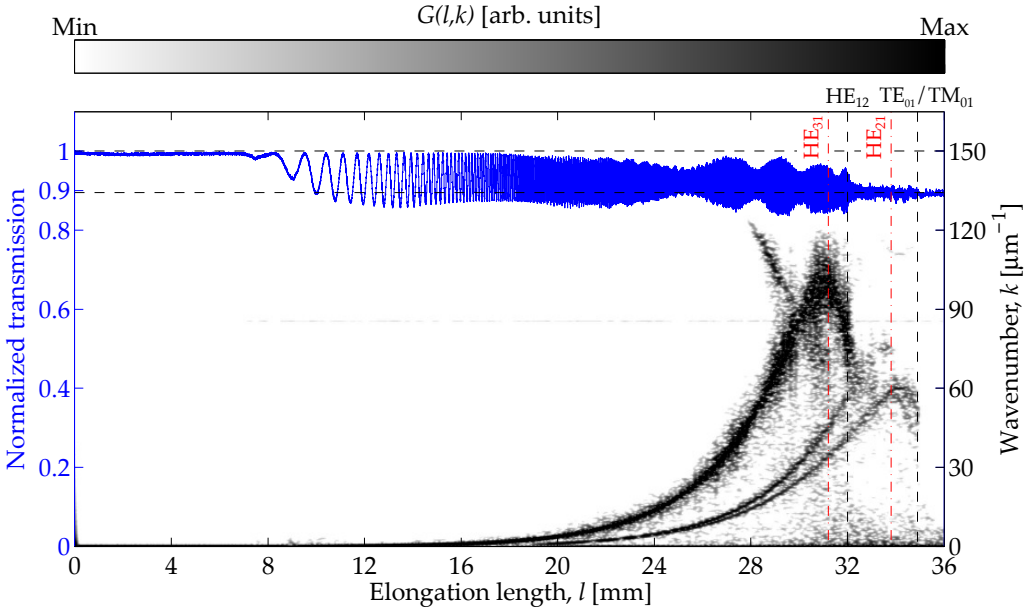

Figure 4.3: *Gabor transform (black) of the same transmission signal (blue) as in Fig. 4.2. The black dashed lines indicate the mode-drops of the HE_{12} mode, and the TE_{01} and TM_{01} modes, at* 32.0 mm *and* 34.9 mm*, respectively, similar to the ones inferred in the transmission plot. The red dashed-dotted lines, at* 31.2 mm *and* 33.8 mm*, indicate two additional mode-drops inferred from the Gabor transform and are assigned to be the loss of the HE_{31} and HE_{21} modes, respectively.*

at 31.2 mm. All four drops of the frequency components are indicated in the figure by the vertical lines. The two black dashed lines coincide with the observed drops in transmission signal thereby supporting the inferred losses to be caused by the mode-drops of the HE_{12} mode and the TE_{01} and TM_{01} modes. The two red

[4]Knowing the pull speeds, $v_\infty = v_+ - v_-$, we have; $l = v_\infty t$ and $k = 2\pi\nu/v_\infty$, for time t and frequency ν.

dotted-dashed lines mark the observation of two other mode-drops now visible due to the Gabor transform. From the known cut-off diameters of the higher order modes in Table 2.1 these additional components are inferred to be the losses of the HE_{31} and HE_{21} modes.

4.1.2 White light transmission

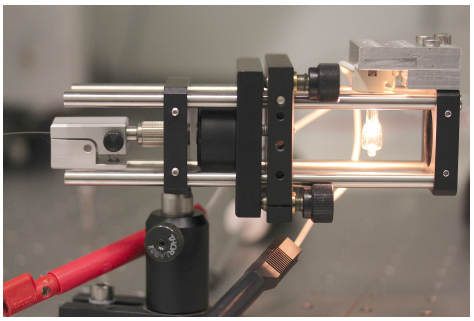

Figure 4.4: *Halogen light bulb mounted in front of a fiber coupler.*

So far we have only considered the transmission of a single wavelength. It is also instructive to see the wavelength dependency of the mode-beating and mode-drops. This can be done using a 20 W halogen light bulb as a white light source, and by coupling it into the fiber instead of the laser, see Fig. 4.4. A spectrometer[5] is used to measure the transmission for different wavelengths in the range 400-1000 nm with 1 nm resolution.

In Fig. 4.5 two spectra of the halogen light bulb are shown. The blue curve is the spectrum of the light transmitted through an unstretched fiber whereas the red curve shows the spectrum without the fiber. In the wavelength range 800 nm to 830 nm the blue curve is considerably steeper than the red. The two profiles should however be similar. The big drop in intensity of the blue curve can be explained if the fiber is multi-mode for wavelengths shorter than about 830 nm and conversely single-mode for longer wavelengths, indicated with the black dashed line. In this case the intensity is greater in the multi-mode

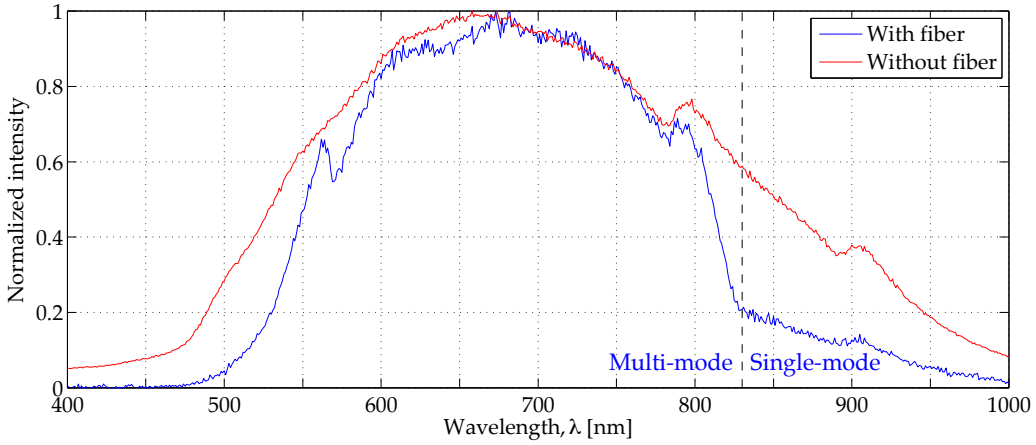

Figure 4.5: *Halogen light bulb spectra. Each curve is normalized with respect to the maximum intensity.*

regime due to the presence of more modes. It thereby gives the impression of a different distribution of present wavelengths in the halogen spectrum than observed without the fiber. With the inferred single-mode cut-off at 830 nm, the 852 nm laser used for characterizing the light transmission in the previous section is single-mode in the fiber.

In Fig. 4.6 the transmission during symmetric pulling of the fiber for various wavelengths in the range 780 nm to 940 nm is plotted. After elongating the fiber by $l = 3$ mm, wavelengths shorter than 830 nm start to strongly oscillate,

[5] Ocean Optics USB650 Red Tide Spectrometer.

whereas longer wavelengths show no oscillatory behavior at this point. This supports the inferred single-mode cut-off to be near 830 nm. At $l = 10$ mm

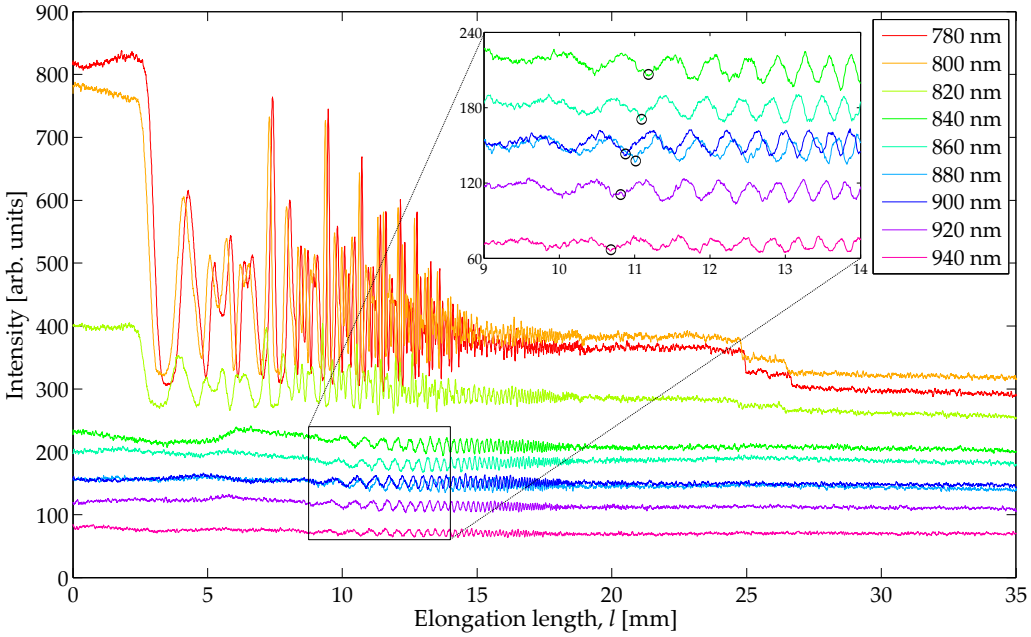

Figure 4.6: *Transmission during symmetric pulling of the fiber for various wavelengths in the range* 780 nm *to* 940 nm. *The signal was recorded with a* 20 Hz *sample rate and pulls speeds* $v_{\pm} = \pm 50$ μm/s. *The elongation length might differ by* ± 1 mm *since the recording and the pulling were not synchronized.*

the single-mode wavelengths starts to oscillate due to interference with exited higher order cladding modes. It is observed that the longer wavelengths start oscillating before the shorter wavelengths, indicated with the black circles in the inset. This can be explained by the V-number dependency on the wavelength; $V \propto 1/\lambda$, such that V is smaller for longer wavelengths. When the decreasing V-number has reached a certain limit a core- to cladding-mode transition of the fundamental mode takes place, as explained in Sec. 2.3, and thus happens for longer wavelengths first.

4.2 CCD imaging

In Sec. 4.1 it became clear that the fiber tapers are non-adiabatic. We therefore need to measure the fiber shape such that the tapers can be optimized according to the adiabatic criteria in Sec. 2.3.1. Obtaining the fiber shape is also important in order to measure important parameters of the fiber, such as the waist length and diameter. For interfacing light with atoms the most optimal shape would be a long homogeneous waist and short steep tapers. This is not fully compatible with adiabatic tapers and in general a trade-off between the two has to be made. Having a complete model of the fiber shape for different pulling procedures is therefore desirable. In Ch. 6–8 such a model is developed and for this it also becomes necessary to measure the fiber shape. Not only to compare the modeled results with the measured but, perhaps more importantly, to optimize the model for our particular boundary conditions.

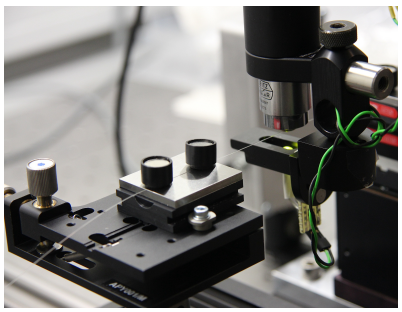

Figure 4.7: *Zoom of camera setup. The microscope objective is above the fiber and the LED is below.*

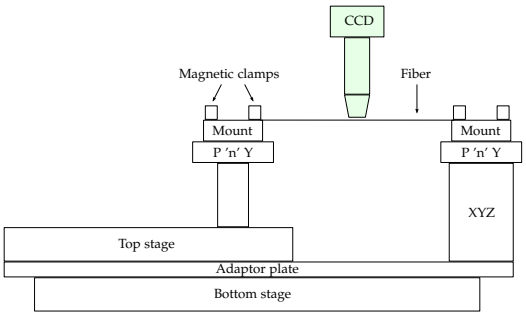

(a) Fiber pull rig with the CCD camera setup highlighted.

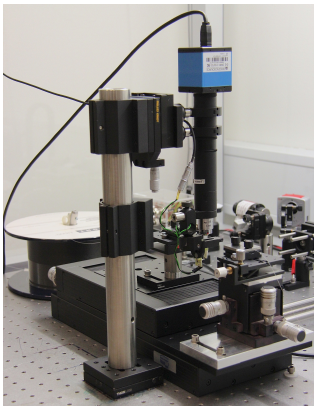

(b) Fiber pull rig with the CCD camera (blue).

Figure 4.8: *The CCD camera is mounted on a vertical post via an extension tube and a translation stage used to adjust the focus. At the end of the extension tube a microscope objective is mounted above the fiber with a magnification of $M = 25$. Using a flip mount a standard green light emitting diode (LED) is positioned to illuminate the fiber from below. Both the objective and the LED is placed only a few millimeters from the fiber. The vertical post is easily positioned and removed using a magnetic kinematic base.*

To measure the fiber shape we image it with a 1024×768 pixel CCD camera[6]. The camera is easily and reproducibly positioned above the fiber using a magnetic kinematic base[7], see Fig. 4.8b and Fig. 4.7 for a zoom at the fiber. A typical image of a stripped un-pulled fiber is shown in Fig. 4.9a. The background has been subtracted to increase the contrast of the fiber edges, but a bright spot from the illuminating LED is still visible. Each image has a width of $(\text{pixel width} \cdot \#\text{ of pixels})/M = 0.14$ mm. To image the whole fiber we use the bottom translation stage to move the fiber in steps of $s = 0.1$ mm with respect to the camera. For every step an image is recorded and by stacking them afterwards

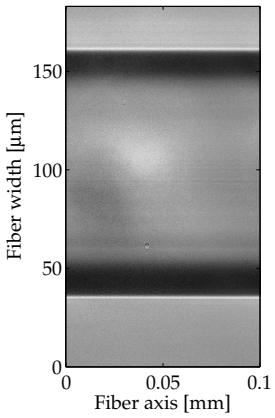

(a) Single CCD image of a stripped un-pulled fiber.

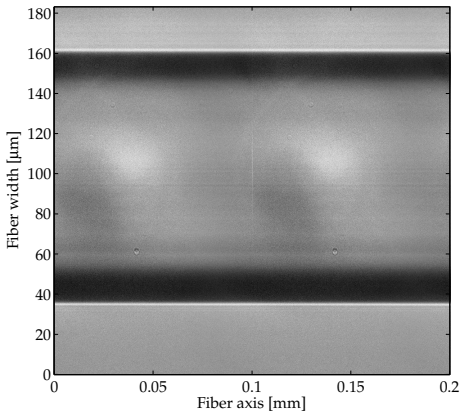

(b) Two partially overlapped CCD images of a stripped un-pulled fiber.

Figure 4.9: *Examples of CCD images of the fiber.*

we obtain the whole fiber profile. Note that the images are actually wider than the step distance of the fiber. We have therefore written an algorithm to linearly interpolate between the images where they overlap. This method of overlapping the images is done to smear out aberration effects that might be in the imaging.

[6] FireWire 400 Monochrome Camera with pixel size (4.65×4.65) μm^2.
[7] Thorlabs KB75/M.

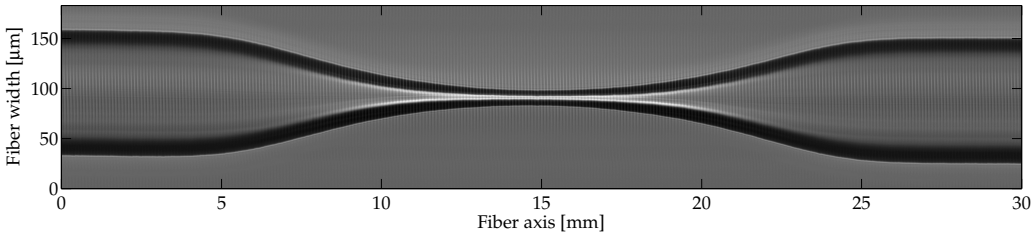

Figure 4.10: *1024 × 165300 square pixel image of the whole fiber after stacking 300 single CCD images. Both tapers and the $d_w = 15$ µm waist are clearly seen. The fiber was elongated symmetrically by $l = 15$ mm. The aspect ratio is not to scale.*

The result is seen for two images in Fig. 4.9b and for the whole fiber in Fig. 4.10. When the waist size of the fiber is smaller than ~ 10 μm air flow makes the fiber vibrate and the images blur. We therefore turn off the flowbox while imaging thin fibers. This potentially causes dust particles to stick to the fiber. However, when the pulling procedure for the optimal fiber shape has been found, imaging is no longer necessary and the fiber can be transferred directly into the experimental setup after pulling if its transmission is good.

4.2.1 Detecting the fiber edges

Having obtained an image of the whole fiber, we can measure its shape. For this we have written an edge detection algorithm in MATLAB. Each column in the whole fiber image, Fig. 4.10, is convolved with a kernel that resembles the contrast between the background and the fiber edge. This increases the contrast between the edges from the rest of the image. In order to choose a proper kernel for the

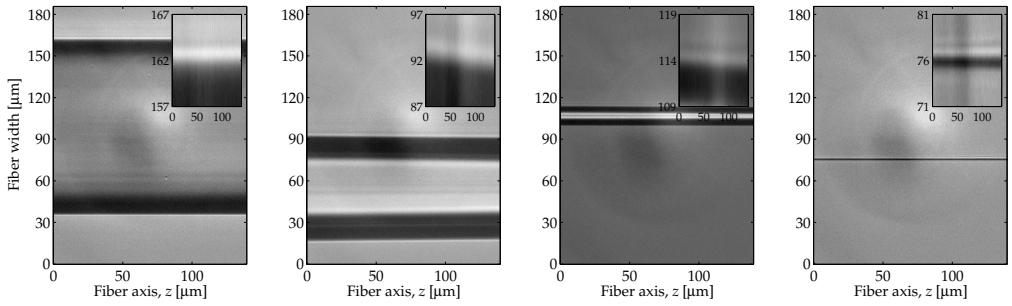

(a) $d = 125$ μm. (b) $d = 75$ μm. (c) $d = 15$ μm. (d) $d \approx 1$ μm.

Figure 4.11: *Examples of the imaging for decreasing fiber diameter. The insets show a zoom in the y-axis with the same scale near the background fiber boundary.*

convolution we consider the fiber-background boundary. In the inset in Fig. 4.11a a white rim between the gray background and the black area is observed. The pixel values thus first increase (white rim) and then decrease (black area) with respect to the gray background.

Over the whole range of varying diameters for the fiber the width of the white rim stays roughly constant as evident from the insets in Fig. 4.11. To mimic the behavior at the boundary a piecewise step-function can be used for the kernel. However, it turns out to give better results using the differential of a Gaussian function which is basically just a smooth version of a step function, see Fig. 4.12.

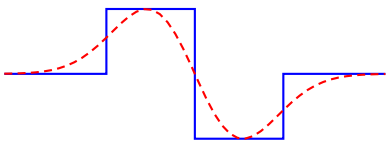

Figure 4.12: *Blue: Piecewise step-function. Red: Differentiated Gaussian function.*

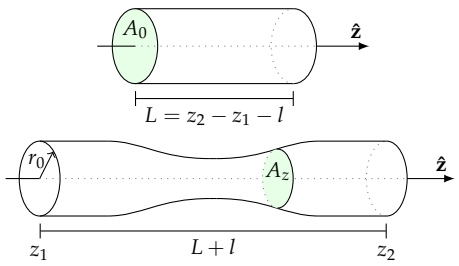

Figure 4.13: *Top: Unstretched fiber. Bottom: Fiber elongated by l, here $A_z = A(z)$.*

To locate the edges[8] we impose volume conservation as a constrain on the edge detection scheme. We know the initial fiber volume to be $V_0 = A_0 L$ as seen in Fig. 4.13. After elongating the fiber by l the volume is; $V_1 = \int_{z_1}^{z_2} A(z)\,\mathrm{d}z$. From volume conservation we have; $V_1 = V_0$, and the initial cross-sectional area (given in pixels squared) can therefore be expressed as:

$$A_0 = \pi r_0^2 = \frac{1}{L}\int_{z_1}^{z_2} \pi r^2(z)\,\mathrm{d}z\,. \tag{4.2}$$

To ensure this equality we increase or decrease the distance between the edges accordingly by adding a constant offset r_{off} to the detected edges $r_{\text{det}}(z)$:

$$r(z) = r_{\text{det}}(z) + r_{\text{off}}\,. \tag{4.3}$$

That is, we choose r_{off} such that:

$$(r_{\text{det}}(z_1) + r_{\text{off}})^2 \overset{!}{=} \frac{1}{L}\int_{z_1}^{z_2} (r_{\text{det}}(z) + r_{\text{off}})^2\,\mathrm{d}z\,. \tag{4.4}$$

It is reasonable to assume the offset to be constant over the whole fiber range since the width of the white rim stays unchanged. This constrain typically moves the edges with a few percent or less with respect to where they were originally located at the unpulled section of the fiber. It should be noted that this procedure only corrects the edges globally. Meaning that local variations of the boundary along the fiber might cause a systematic error such that we either over- or underestimate the fiber diameter over the whole fiber range. In Fig. 4.14 the fiber from Fig. 4.10 is shown with detected edges marked in red.

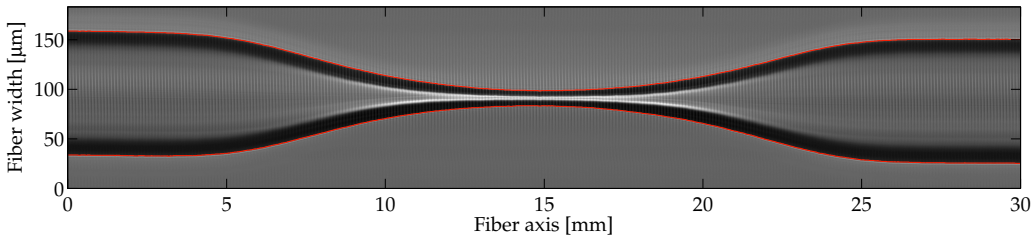

Figure 4.14: *Stacked CCD images of whole fiber with edges marked in red.*

As an example of local variations of the fiber boundary we consider the four fiber images for decreasing diameters shown in Fig. 4.11. All the way to $d = 15$ μm the white rim is still clearly visible on both sides of the fiber. But when the diameter becomes very small we see in Fig. 4.11d that the white rim is only visible on one side of the fiber. This makes the edges detection performance less stable and is observed to generally cause an overestimation of the thin fiber diameter. When employing volume conservation a local overestimation of the fiber diameter tend to move the edges closer together causing systematic errors over the whole fiber range. For reasons explained in section Sec. 4.2.2, the volume conservation constraint is, however, not imposed on fibers with waist diameters smaller than 10 μm. Having found that the edge detection works very well for

[8] Are the edges located at the white rim background interface or rather where the white and black meet?

larger diameters, and locate the edges within a few percent of what is expected from volume conservation, we assert that only thin sections with $d \lesssim 10$ μm have a significant systematic error.

We obtain the fiber diameter by subtracting the edges. To get it in SI units we define a conversion factor from pixels to μm as:

$$c_\mathrm{t} = \frac{d_0}{2\sqrt{A_0/\pi}}\,, \tag{4.5}$$

using the known initial fiber diameter; $d_0 = 2r_0 = 125 \pm 2$ μm. The subscript t indicates the conversion factor to be along the transverse direction of the fiber. Since we know the fiber step size in millimeters between each image, as well as the images width and overlap in pixels, the conversion factor can also be calculated along the longitudinal direction as:

$$c_\mathrm{l} = \frac{\text{step size}}{\text{image width} - \text{overlap}}\,. \tag{4.6}$$

The two conversion factors should be identical. Any discrepancy between them might either indicate distortion of the images caused by aberration effects in the objective, or uncertainties in, *e.g.*, the estimated partial overlap of the images or the inherent uncertainty on the initial fiber diameter. For the fiber in Fig. 4.14 the conversion factors are found to be:

$$c_\mathrm{t} = 0.181 \pm 0.004\ \mu\mathrm{m/pixels}\,, \tag{4.7a}$$
$$c_\mathrm{l} = 0.182 \pm 0.001\ \mu\mathrm{m/pixels}\,, \tag{4.7b}$$

and are seen to lie well within their uncertainties given by propagating errors from the quantities used to calculated the conversion factors, see Appendix B.

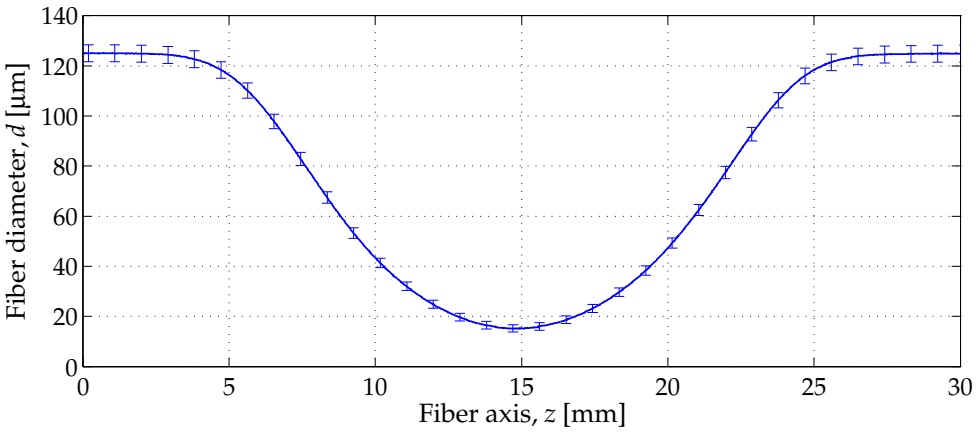

Figure 4.15: *Measured diameter for the fiber shown in Fig. 4.14. The fiber was symmetrically elongated $l = 15$ mm to a waist diameter of $d_w = 15$ μm.*

The measured diameter of the fiber shown in Fig. 4.14 is plotted in Fig. 4.15. The errorbars originates from propagating errors on the inherent fiber diameter; $\sigma_d = \pm 2$ μm, the estimated error on the edge detection; $\sigma_e = \pm 5$ pixels; the pull length $\sigma_l = \pm 10$ μm, and the longitudinal conversion factor; $\sigma_{c_\mathrm{l}} = \pm 1$ μm/pixel. The systematic error on the thin fiber section is also added[9] by setting it to scale inversely proportional with the diameter; $\sigma_\mathrm{sys} = \kappa/d$, where κ is chosen such that the systematic error is 1 μm at $d = 1$ μm; $\kappa = 1$ μm^2. The reader is referred to Appendix B for more details on the error analysis. The errorbars are only shown for selected points in order not to clutter the plot.

[9] $\sigma_d^2 = \sigma_\mathrm{prop}^2 + \sigma_\mathrm{sys}^2$, where σ_prop is the propagating error.

4.2.2 Limitations on the CCD imaging

The optical imaging works very well for fibers thicker than 10 μm. For thinner fibers, however, several things make it more complicated. In Fig. 4.11d it became evident that a systematic error on the edge detection of thin fibers is present caused by a diameter dependent change in the fiber and background boundary. This is caused by the limited optical resolution given to be 0.18 μm/pixels in Eq. (4.7a). For aimed fiber diameters of 0.5 μm the image is thus only about 2.5 pixels wide. While this can partly be taken into account in the diameter analysis, by estimating the error, we also face another issue for thin fibers.

When the fibers become thinner than $\sim$ 10 μm they start to bend as shown in Fig. 4.16. This causes problems in the CCD imaging in two aspects. First, the fiber might bend so much that it simply moves out of the image region of the CCD chip. It therefore becomes necessary to do the imaging several times to cover the whole fiber profile. Second and even worse, the fiber might bend in and out of the imaging plane thereby causing the images to blur. This is not only highly impractical but might also introduce additional systematic errors on the edge detection scheme as the boundary between background and fiber now vary in an unpredictable way over the fiber profile. The fiber shown here stays in

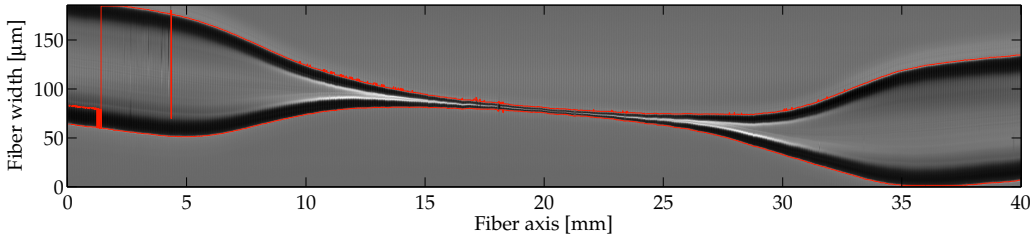

Figure 4.16: *Image of a bend fiber. The fiber was symmetrically elongated $l = 25$ mm to a waist size $d_w \approx 5$ μm.*

focus and mainly within the image region of the CCD chip, but this is seldom the case for longer elongation lengths. The edge detection scheme works well in this example but the constrain on the volume conservation cannot be imposed here since measured edges along the whole tapering profile are needed for this (the edge detection fails around 35 mm where the fiber is very close to the border of the CCD chip image region).

Unfortunately, the origin of the fiber bending is still not fully understood. When we first started seeing this effect we believed it was caused by transverse tension in the fiber. A big effort was therefore spend in aligning the fiber mounts. After some investigation we found that irregularities and dirt in the fiber mount V-grooves induce the sought-after transverse tension and cause the fiber to bend. By cleaning the grooves and placing the rubber-padded magnets differently we could get rid of this effect. However, recently the fiber bending has occurred again regardless of the magnet position and the cleanness of the V-grooves.

The bent fibers cause both practical and physical limitations. The transmission through the fibers is generally 90% for symmetric pulls, Fig. 4.1.1, with the 10% loss inferred to be the mode-drop of the HE_{12}, HE_{21}, HE_{31}, TE_{01}, and TM_{01} modes. Only the HE_{12} mode with the same azimuthal symmetry as the fundamental mode can be exited for axisymmetric fibers. It should therefore be possible to increase the coupling from the untapered fiber into the nanofiber by making the fibers bend less.

4.2.3 Reproducibility of the fiber pulling

To test the reproducibility of the fiber pulling we have made four fibers with the same pulling procedure, Table 4.1 and parameters; $l = 15$ mm, $v_{\pm} = \pm 50$ μm/s, $t_{\text{wait}} = 5$ s, and $P_{\text{oven}} = 100$ W. The measured fiber shapes are shown in Fig. 4.17.

Table 4.1: *Pulling procedure.*

Step	Procedure
(i)	Drive oven in when temperature at "P_{oven}".
(ii)	Wait a time t_{wait} for fiber to thermalize.
(iii)	Start pulling with constant speeds $v_{\pm}$.
(iv)	After pulling a distance l stop stages.
(v)	Drive oven back.

The small horizontal shift between the four curves is most likely due to the positioning of the camera which is not very precise compared to the positioning of the stages and the oven. On the blue dashed-dotted and cyan dotted curve we

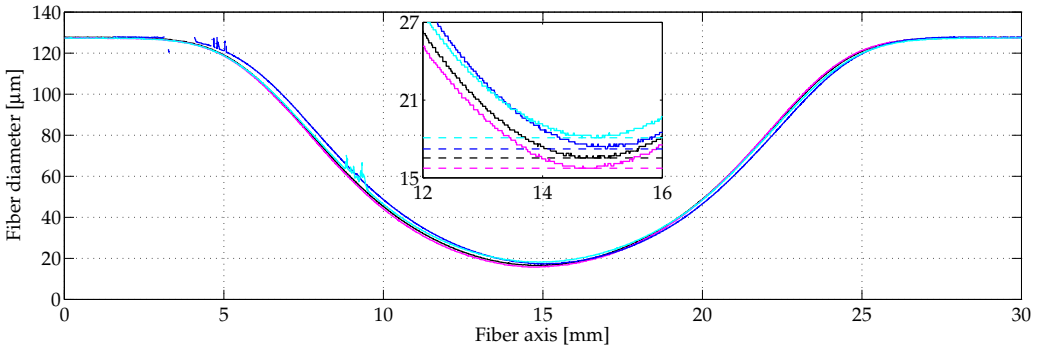

Figure 4.17: *Plot of four fiber shapes made with the same pulling procedure and parameters. The inset shows a zoom at the fiber waist with dashed horizontal lines indicating the minimum waist for all four fibers.*

observe glitches at positions 5 mm and 9 mm. These are caused by marks that were put on the fibers with a waterproof pen for position reference between the CCD images and scanning electron microscopy images of the fiber. The latter is described in Sec. 4.3. The fiber for the cyan dotted curve is shown in Fig. 4.18 where the mark is clearly seen.

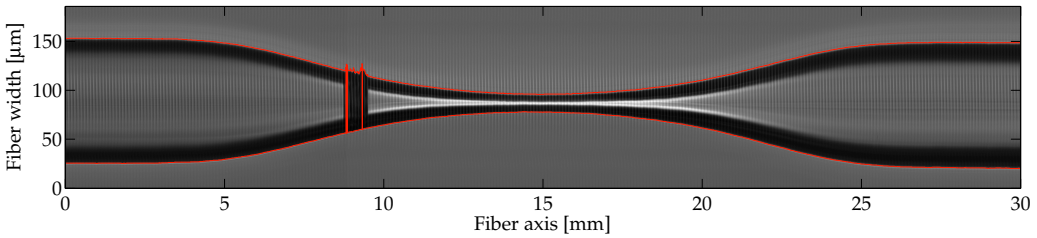

Figure 4.18: *Fiber marked with waterproof pen at position 9 mm. The two red curves indicates the detected edges. The fiber diameter is given by the cyan curve shown in Fig. 4.17.*

The waist sizes of the four curves are measured to:

$$\text{cyan:} \quad d_w = 18.1 \pm 1.3\ \mu\text{m}, \tag{4.8a}$$
$$\text{blue:} \quad d_w = 17.2 \pm 1.4\ \mu\text{m}, \tag{4.8b}$$
$$\text{black:} \quad d_w = 16.5 \pm 1.3\ \mu\text{m}, \tag{4.8c}$$
$$\text{magenta:} \quad d_w = 15.7 \pm 1.3\ \mu\text{m}, \tag{4.8d}$$

with uncertainties given according to the errorbars shown in Fig. 4.15. They all lie within the uncertainties and the fiber pulling is reproducible.

4.2.4 Oven power dependence

The fiber shape depends on the temperature of the hot zone provided by the oven. In Sec. 3.2.1 we explained how the oven is operated by controlling the power. Following the pulling procedure given in Table 4.1 we have measured the fiber shape for varying oven powers keeping the other parameters constant; $l = 15$ mm, $v_\pm = \pm 50\ \mu$m/s, and $t_{\text{wait}} = 5$ s, see Fig. 4.19. For high oven power

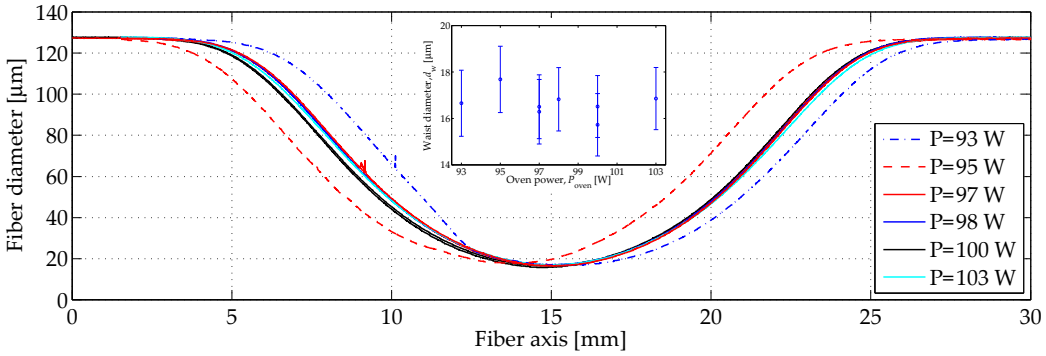

Figure 4.19: *Measured fiber shape for various P_{oven} in the range* 93 W *to* 103 W. *All fiber were symmetrically elongated by $l = 15$ mm, $v_\pm = \pm 50\ \mu$m/s, and $t_{wait} = 5$ s. Inset: waist size d_w as a function of the oven power P_{oven}.*

above $P_{\text{oven}} = 97$ W all the curves follow each other closely. While for lower oven powers the corresponding blue dashed-dotted curve and red dashed curve are seen to deviate substantially. This suggests that the glass fiber was not sufficiently molten at these temperatures. When the pulling starts the fiber therefore partially slips underneath the magnetic clamps and partially stretches. This results in an asymmetric fiber especially observed for the fiber made with the lowest oven power $P_{\text{oven}} = 93$ W. Unless otherwise stated all fibers used in this thesis have been obtained for $P_{\text{oven}} = 100$ W.

4.3 Scanning electron microscopy

To confirm the results for the fiber shape obtained by the CCD imaging, and especially to measure the fiber diameter when it is smaller than 10 μm, we have measured a subset of the fibers using scanning electron microscopy (SEM), see Fig. 4.20a. The diameter is obtained by using the scale given in each SEM image. In Fig. 4.21 and Fig. 4.22 a comparison between the CCD imaging (blue curves) and SEM imaging (red curves) is shown for two fibers symmetrically elongated by $l = 15$ mm and $l = 36$ mm respectively. Unfortunately the calibration of the SEM imaging is not known, so the errorbars come solely from an estimated read-off error on the images. It should also be noted, that the fiber axis is not an absolute scale for the blue and the red curves: for the SEM imaging, only the

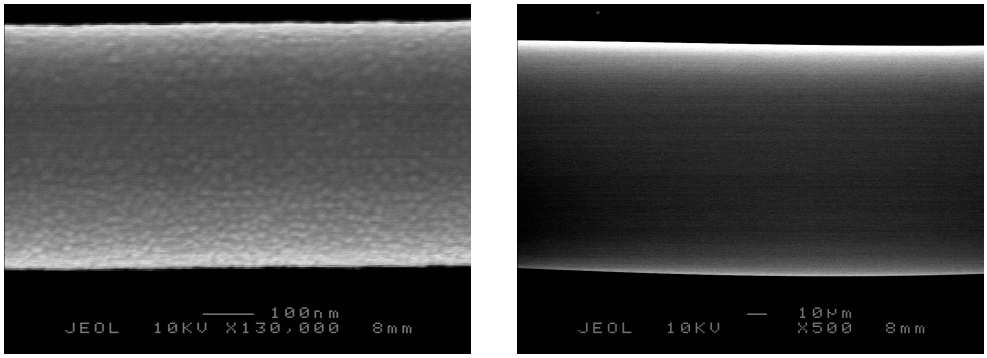

(a) Typical SEM image of the fiber. (b) Distorted SEM image.

Figure 4.20: *(a) The waist size is measured to* $d_w = 480$ nm *for a symmetric elongation of* $l = 36$ mm*. The spots on the fiber originate from a 30 nm gold layer sputtered on the fiber to keep it from charging up during the SEM scan. This extra layer has not been taken into account and the actual fiber diameter might therefore be smaller than the measured. (b) Depending on where the diameter is measured we obtain either* 115 μm *or* 118 μm *for an expected* 125 μm *diameter fiber.*

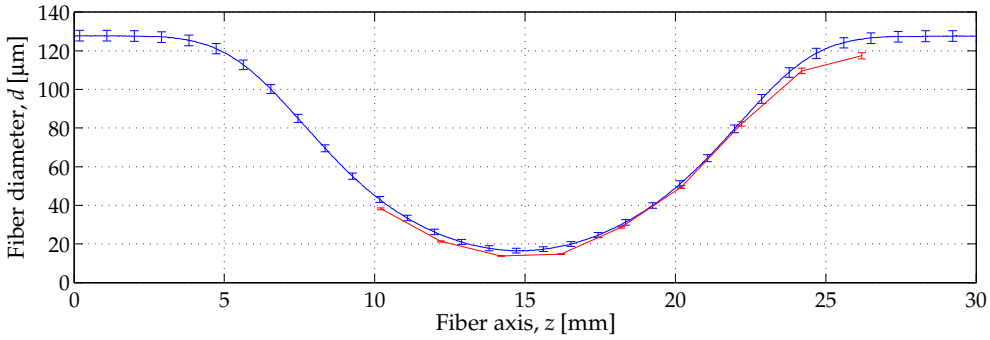

Figure 4.21: *Blue lines: Fiber diameters measured using CCD imaging. Red line: SEM Measured diameters using SEM imaging. The fiber was symmetrically elongated* $l = 15$ mm *to a waist diameter of* $d_w = 15$ μm*. The CCD images of the fiber is shown in Fig. 4.10.*

relative distance between measured fiber diameters is known[10]. In general, the SEM imaging yields fiber diameters smaller than what is obtained by the CCD imaging. Furthermore, near the beginning of the tapered section, at $z = 25$ mm in Fig. 4.21, the two curves deviate slightly more than over the rest of the fiber profile. This suggests that a systematic error is present in either the CCD or SEM imaging, causing the shape to be expanded or compressed. It is hard to judge which of the two is the case. It should be noted that the SEM images were slightly distorted for thick fiber diameters $d \gtrsim 100$ μm which could explain some of the deviation between the two curves, see Fig. 4.20b.

In Fig. 4.22, the overestimation by the CCD imaging of the thin fiber sections is clearly evident. At $z = 26$ mm the measured diameter obtained with the CCD imaging has a small kink with should not be present. Apart from this, we conclude the CCD imaging to work well in measuring the fiber diameter.

[10]The fiber shown in Fig. 4.18 was marked in order to actually have an absolute scale between the CCD and SEM imaging. But unfortunately these marks could not be observed on the SEM images.

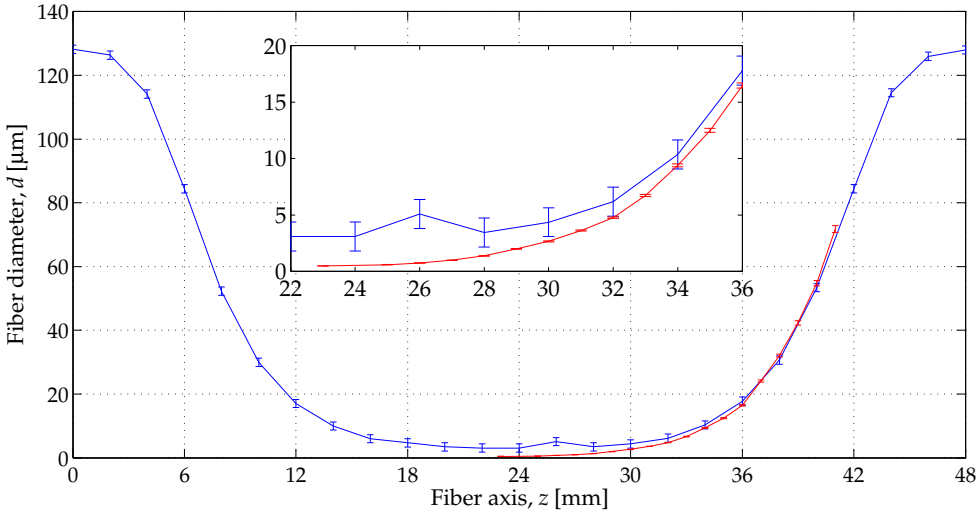

Figure 4.22: *Blue lines: Fiber diameters measured using CCD imaging. Red line: SEM Measured diameters using SEM imaging. The fiber was symmetrically elongated* $l = 36$ mm *to a waist diameter of* $d_w = 480$ nm. *The SEM image of the waist is shown in Fig. 4.20a.*

4.4 Summary

In this chapter we have characterized the optical and spatial properties of the fiber. During the pulling procedure the transmission signal of a single-mode laser was recorded and analyzed in both the time- and frequency domain. From this we inferred the excitation of higher-order cladding modes during the core-cladding transition of the fundamental mode about 10% loss of the light transmission. We therefore concluded that the tapers are non-adiabatic and could be improved by applying the adiabatic criteria by [Love *et al.* 1986; Love *et al.* 1991].

To characterize the spatial properties of the fiber we have analyzed both CCD and SEM images of the fiber. For the CCD images an edge detection algorithm has been written and shown to reliably measure the fiber diameter down to waist sizes of about 10 μm. For thinner fibers the optical resolution limits the imaging and the fiber starts to bend out of the image plane of the CCD camera. This generally cause the edge detection to overestimate the diameters in this limit. In Sec. 4.2.3 we showed that we can make highly reproducible nanofibers using the constructed fiber pulling rig. The shape dependence on the oven power where measured in Sec. 4.2.4. It was found to have a significant influence when below 97 W, whereas oven powers above this value consistently yield the same fiber shape. The measured diameters from the CCD imaging technique were confirmed by SEM images in Sec. 4.3. The latter was found to give consistently smaller values for the fiber diameter than obtained by the former. Especially for thick fiber diameters above 100 μm the two method yields different results. This can partially be explained by the slightly distorted images obtained from the SEM imaging in this limit. The consistently smaller diameters found by the SEM imaging could be caused by a wrong calibration of the SEM or an unknown systematic error in the edge detection algorithm of the CCD images of the fiber. In this and the preceding chapter we have now shown how to produce nanofibers and characterized some of their main properties. To optimize the fiber properties for specific applications the remaining thesis is devoted to the modeling of the fiber shape. Here the measured shape of the fiber will be seen to play a vital role.

Part II

Modeling the fiber shape

Chapter 5

Simple heat-and-pull model

Having characterizing the fibers we are now ready to model our results for the measured fiber shape. In this chapter we will compare it with the simple heat-and-pull model by [Birks *et al.* 1992], described in Sec. 2.2. We start by recapitulate the main assumptions behind the model:

(i) The fiber is always heated uniformly.
(ii) The heated section is always cylindrical.
(iii) The fiber mass and volume is conserved.

In Sec. 2.2.1 we found that (i)-(iii) implies the longitudinal velocity profile of the fiber to be linear inside the hot zone $L_0 = z_+ - z_-$. For symmetric pulls this leads to a fiber shape described by exponential transitions and a uniform waist with the length given by L_0, Eq. (2.7):

$$\frac{r(z)}{r_0} = \begin{cases} 1 & \text{for } z < \tilde{z}_-, \\ e^{-(z-\tilde{z}_-)/L_0} & \text{for } \tilde{z}_- < z < z_-, \\ e^{-l/(2L_0)} & \text{for } z_- < z < z_+, \\ e^{-(\tilde{z}_+ - z)/L_0} & \text{for } z_+ < z < \tilde{z}_+, \\ 1 & \text{for } \tilde{z}_+ < z. \end{cases} \tag{5.1}$$

Shown graphically in Fig. 5.1.

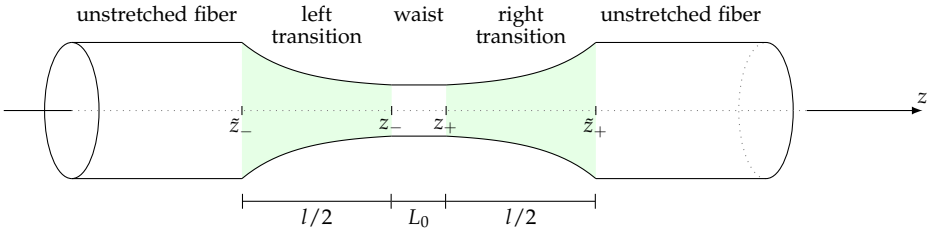

Figure 5.1: *Fiber shape according to the model by [Birks* et al. *1992].*

5.1 Shape analysis

In Fig. 5.2 the fiber shape from this simple heat-and-pull model (red dashed line) is plotted against the measured diameter (blue solid line)[1]. The hot zone length

[1] Using the fiber from Fig. 4.10.

required in Eq. (5.1) is taken to be the solution of Eq. (2.6):

$$d_{\mathrm{w}}(l) = d_0 \exp\left(-\frac{l}{2L_0}\right). \tag{5.2}$$

For the initial fiber diameter $d_0 = 2r_0 = 125$ μm, and the measured waist size $d_{\mathrm{w}} = 15$ μm, this yields; $L_0 = 3.6$ mm. The expected shape from the simple

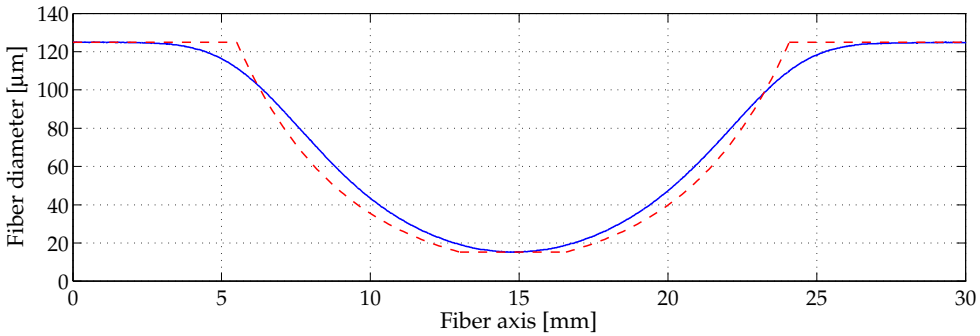

Figure 5.2: *Blue solid line: Measured diameter of a fiber symmetrically elongated by $l = 15$ mm to a waist diameter of $d_w = 15$ μm. Red dashed line: Fiber shape predicted by the simple heat-and-pull model.*

heat-and-pull model deviates substantially from the measured curve. Near $z = 8.5$ mm and $z = 21.5$ mm the measured curve is observed to have a sign change in the curvature in stark contrast to the modeled shape. At the beginning of the transitions the measured diameter starts out rather smoothly whereas the model predicts sharp edges. Considering the simple assumptions the model is based on this is not surprising. The length of the oven is 20 mm with an effective hot zone length around $3-4$ mm. Flames used as heating device typically have a width of $1-2$ mm. The temperature profile of the relatively large oven is therefore more likely to have some Gaussian-like shape, rather than being uniform, compared to more narrow heaters. Intuitively, this fits with the observed smoothness of the measured diameter.

The pulling procedure suggested by [Birks *et al.* 1992] is easy to implement and seen to give fairly adiabatic taper transitions in Sec. 4.1. For many applications the final waist size is the important parameter. In this respect several groups have shown that the model works reasonably well and therefore rely on it when characterizing their fibers [Brambilla *et al.* 2004; Ward *et al.* 2006; Ding *et al.* 2010]. Note that the modeled shape in Fig. 5.2 was forced to have the same waist size as the measured. If Eq. (5.2) should be tested it is of course necessary to make a series of measurements of it for varying pull lengths[2]. On the other hand, if optimized coupling into the nanofiber is needed, or a special design of the tapers and waist are desired, the model is not sufficient for our wide heater. We therefore need a generalized flow model which can take a larger non-uniform hot zone into account. This is the subject of the remaining chapters 6–8.

[2]Eq. (5.2) can also be tested using the inferred mode-drops in Sec. 4.1.1.

Chapter 6

Fiber flow

In Ch. 5 it became evident that the simple heat-and-pull model developed by [Birks *et al.* 1992] does not describe the shape of our nanofibers. We therefore seek a more general model not limited to heaters where a uniform temperature distribution, and thus a linear velocity profile of the fiber flow, can be assumed. In this chapter general considerations of the fiber flow will be given. From this we will obtain a continuity equation for the fiber shape depending on its longitudinal velocity profile. Thereafter the boundary conditions of the fiber are given in Sec. 6.1.1. Both sections will be applied throughout the remaining chapters 7−8.

6.1 Continuity equation

We start by considering the geometry of the cylindrical fiber as shown in Fig. 6.1. This can be described by its cross-sectional area $A(z,t)$, where t denotes time and z the fiber axial coordinate. For a small section of the fiber ranging from position

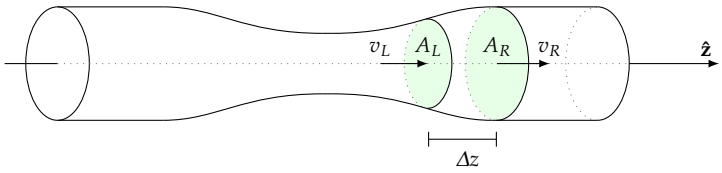

Figure 6.1: *Sketch of the fiber geometry with cross-sectional areas;* $A_L = A(z,t)$, $A_R = A(z+\Delta z,t)$, *and longitudinal velocities;* $v_L = v(z,t)$ *and* $v_R = v(z+\Delta z,t)$.

z to $z+\Delta z$ the mass is given by:

$$m = \int_V \varrho \, \mathrm{d}V = \int_z^{z+\Delta z} \varrho A(\zeta,t) \, \mathrm{d}\zeta \approx \varrho A(z,t)\Delta z \,. \tag{6.1}$$

Here we assume that the fiber is an incompressible fluid, thus neglecting thermal expansion and compression, such that the mass density ϱ of the fiber is constant. During the pull mass can flow into and out of the section z to $z+\Delta z$. Let $v(z,t)$ denote the position and time dependent longitudinal velocity component. Per time interval $\mathrm{d}t$ the mass $\varrho v(z,t)A(z,t)\mathrm{d}t$ flows into the section through the left disk in Fig. 6.1 and the mass $\varrho v(z+\Delta z,t)A(z+\Delta z,t)\mathrm{d}t$ leaves it through the right disk:

$$\mathrm{d}m = -\varrho\big(v(z+\Delta z,t)A(z+\Delta z,t) - v(z,t)A(z,t)\big)\mathrm{d}t \,. \tag{6.2}$$

By equating Eq. (6.1) and Eq. (6.2) and taking the limit $\Delta z \to 0$ we obtain the continuity equation:

$$-\frac{\partial}{\partial t}A(z,t) = \frac{\partial}{\partial z}\Big(A(z,t)\,v(z,t)\Big) \,. \tag{6.3}$$

Solving this linear differential equation for proper boundary conditions lets us determine the fiber shape for all times and positions along the fiber. An analytic solution for $A(z,t)$ exists if the fiber velocity profile is a separable function in space and time. In Ch. 7 we will therefore consider the specific case of a time-independent velocity profile $v(z,t) = v(z)$. For this and the following chapter, where the more general case $v(z,t)$ is considered, the boundary conditions of the fiber flow will be very important. These are therefore presented in the following.

6.1.1 Boundary conditions

In this section the boundary conditions of the fiber flow is given. Outside the hot zone the fiber is frozen and moves uniformly. The longitudinal fiber flow $v(z,t)$ for regions on either side of the hot zone are therefore constant and we have:

$$v(z,t) = \begin{cases} v_- & \text{for } z < z_-, \\ v_+ & \text{for } z > z_+, \end{cases} \tag{6.4}$$

where z_- and z_+ are the positions for the boundary between the hot zone and the surroundings, see Fig. 6.2, with the hot zone length given by:

$$L_0 = (z_+ - z_-)\,. \tag{6.5}$$

Inside the hot zone $v(z,t)$ is described by an unknown function, dependent on the temperature distribution of the fiber and the constant pull speeds $v_\pm$. The

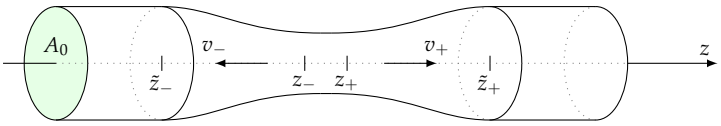

Figure 6.2: *Sketch of the boundary conditions of the fiber.*

boundary between each taper and the unstretched fiber is marked by $\tilde{z}_\pm$. Outside the tapered sections, $z < \tilde{z}_-$ and $z > \tilde{z}_+$, we have A_0 for the cross-sectional area of the initial uniform fiber. We introduce the convenient variables;

$$v_\infty = v_+ - v_-\,, \tag{6.6a}$$

$$l_\pm = v_\pm t = \tilde{z}_\pm - z_\pm\,, \tag{6.6b}$$

where $l_\pm$ are the pull lengths on either side of the oven.

Chapter 7

Stationary velocity profile

In this chapter we will focus on the special case where the fiber velocity is constant in time; $v(z,t) = v(z)$. This serves two purposes. First, by having an analytic solution for $A(z,t)$, for some unknown function of $v(z)$, it is possible to invert the equation and obtain a solution for $v(z)$ as a function of $A(z,t)$ instead. Since we can measure $A(z,t)$, described in Sec. 4.2, we are therefore able to infer the longitudinal fiber flow $v(z)$. This can then be used in the solution for the fiber shape and we can thus obtain $A(z,t)$ without using any involved fluid dynamics. Second, if $v(z)$ is chosen explicitly to be a linear function in z we can sanity check the continuity equation, which, in this particular case, should yield the same fiber shape as that predicted by Birks and Li's simple heat-and-pull model in Ch. 5.

7.1 Unknown velocity profile

We start with the situation where $v(z)$ is an unknown time-independent function inside the hot zone but known outside according to the boundary conditions in Sec. 6.1.1:

$$v(z) = \begin{cases} v_- & \text{if } z \leq z_-, \\ ? & \text{if } z_- < z < z_+, \\ v_+ & \text{if } z_+ \leq z. \end{cases}$$

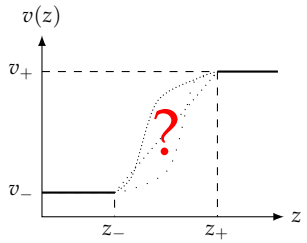

With this velocity profile we seek a general solution of the continuity equation:

$$-\frac{\partial}{\partial t} A(z,t) = \frac{\partial}{\partial z}\Big(A(z,t)\, v(z)\Big)\,. \tag{7.1}$$

For $v(z)$ time-independent the differential equation is considerably simplified and we find for the general solution[1]:

$$A(z,t) = \frac{1}{v(z)}\, \mathcal{F}\left(\int_{z_0}^{z} \frac{1}{v(\zeta)}\, \mathrm{d}\zeta - t\right), \tag{7.2}$$

where $\mathcal{F}(z,t)$ is an arbitrary function depending on the boundary conditions. Assuming an initially uniform fiber; $A(z,0) = A_0$, an explicit form can be given:

$$A(z,l) = A_0\, \frac{\partial}{\partial z}\Big(q^{-1}\big(q(z) - l\big)\Big)\,, \tag{7.3a}$$

$$q(z) \equiv \int_{z_0}^{z} \frac{v_\infty}{v(\zeta)}\, \mathrm{d}\zeta\,, \tag{7.3b}$$

[1] Obtained both in Mathematica and by using the method of characteristic curves [Riley *et al.* 2006]

for arbitrary z_0. $A(z,l)$ has here been written in terms of the more relevant variable $l = v_\infty t$; the total elongation length of the fiber. It should be noted that $q^{-1}(\cdot)$ is the inverse function of $q(z)$; $q^{-1}(q) = z$, and not $1/q(z)$. Both the general and particular solution, Eq. (7.2) and Eq. (7.3a), can be directly verified by differentiation, and the calculations leading from the former to the latter can be found in Appendix C.1.

In order to apply Eq. (7.3a) and obtain the expected fiber shape we need the longitudinal velocity profile of the fiber flow $v(z)$. This can be obtained by inverting the function 7.3a to yield a solution for $v(z)$. From a measured shape and known boundary conditions, $A(z,l)$ and $v_\pm$ respectively, $v(z)$ can thus be inferred using the following recursion formula:

$$v\big(y(z,l)\big) = \frac{A(z,l)}{A_0} v(z)\,, \tag{7.4a}$$

$$y(z,l) = -\int_z^{\tilde{z}_+} \frac{A(\zeta,l)}{A_0}\,\mathrm{d}\zeta + z_+\,. \tag{7.4b}$$

The derivation can be found in Appendix C.2.

7.1.1 Interpreting $y(z,l)$

Before inferring the velocity profile from the recursion formula we will consider the introduced function $y(z,l)$. This can be interpreted as the old coordinate axis for the fiber, before it was elongated by l, expressed in terms of the new fiber coordinate z after the pull. If the fiber was not stretched we expect to have $y(z,0) = z$. Checking with Eq. (7.4b) this is indeed true, since the argument inside the integral will be equal to one and $\tilde{z}_+ = z_+$.

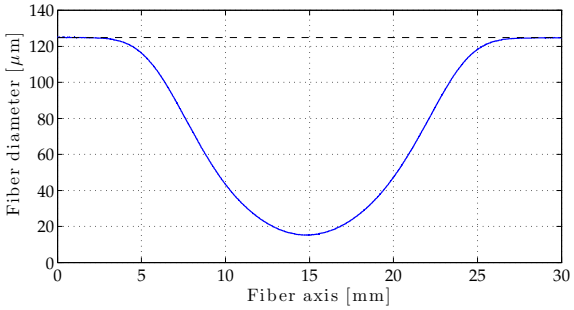

(a) Blue solid line: Fiber diameter used to calculate $y(z,l)$. The fiber was symmetrically elongated $l = 15$ mm. The black dashed line indicates the initial fiber diameter $d_0 = 125$ μm.

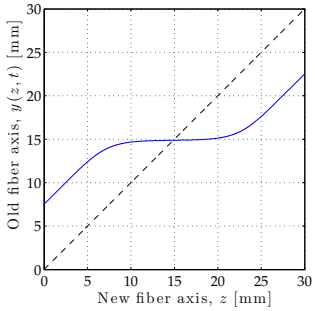

(b) Blue solid line: Old fiber axis $y(z,l)$ as a function of the new fiber axis z. Black dashed line: $y(z,0) = z$.

Figure 7.1: *(a) Measured diameter of a symmetrically elongated fiber by $l = 15$ mm. (b) Calculated $y(z,l)$ using Eq. (7.4b) with the measured diameter in (a)*

To illustrate the form of $y(z,l)$ it has been calculated using the measured diameter of a symmetrically pulled fiber in Eq. (7.4b). Both the diameter and $y(z,l)$ are shown in Fig. 7.1. We see that the point $z = 0$ mm, located on the pulled fiber, was at position $y = 7.5$ mm on the un-pulled fiber, relative to the new fiber axis. That is, this particular point has moved a distance -7.5 mm during the pull. In Fig. 7.1a we see that this particular point is outside the tapered fiber region. It must therefore have been outside the oven when the pulling started, such that is has moved $l_- = v_- t = -l/2$.

Points near $z = 15$ mm must have been near the oven center at the beginning of the pull. This is also implied by Fig. 7.1b since these point are located at almost

the same position after the pull (z) as before the pull (y). Because the pull speeds, for this fiber, were $v_\pm = \pm v_\infty/2$, this makes good sense as the speed near the oven center must be close to zero.

7.1.2 Recursion formula for $v(z)$

To appreciate the recursion formula we shall, as an example, consider the "+" side of the fiber, *i.e.*, the range $z_+ < z < \tilde{z}_+$ in Fig. 7.2. For this specific interval we

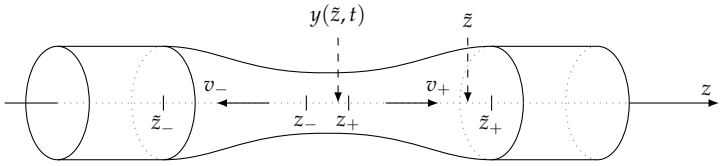

Figure 7.2: *Sketch illustrating how far the point $y(\tilde{z},t)$, of the up-pulled fiber, has moved after elongating the fiber by $l = v_\infty t$. The new point is denoted by $\tilde{z}$.*

can readily calculate the right hand side (RHS) of Eq. (7.4a), since $v(z > z_+) = v_+$ is known from the boundary conditions, Sec. 6.1.1, and the fiber cross-sectional area $A(z,t)$ can be measured for all z as shown in Sec. 4.2. From Eq. (7.4b) we note that:

$$y(z,t) < z_+ \text{ for } z_+ < z < \tilde{z}_+ \,. \tag{7.5}$$

because the integral is always positive. This means that the velocity can be inferred at point y, further inside the oven. However, for pulls where a zero point of the velocity exists inside the oven, the above recursion only yields $v\big(y(z,t)\big)$ for points where $y(z,t) < z$. For the symmetric pull considered in Fig. 7.1b, the velocity is zero at the oven center z_c, and the corresponding range is $z > z_c = 15$ mm. From symmetry the recursion can of course be applied from the "-" side as well, and it is therefore possible to obtain $v(z)$ for all z. Note, if the temperature distribution is symmetric around z_c, the flow will also be symmetric around this point and it would be enough to measure $v(z)$ from one side only.

Employing the recursion formula we find $v(z)$ for the same fiber as used in Fig. 7.1. For details the reader is referred to Appendix C.3. The result is shown as the blue curve in Fig. 7.3. Note that the z-axis has the same absolute scale as in Fig. 7.1. The black dashed-dotted line is the predicted linear velocity profile

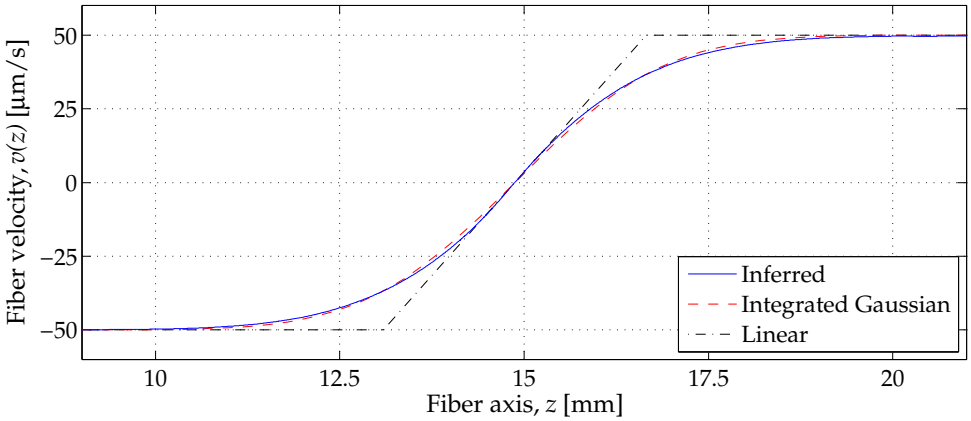

Figure 7.3: *Inferred stationary longitudinal velocity profile of a fiber symmetrically elongated by $l = 15$ mm. The constant pulls speeds outside the oven were $v_\pm = \pm 50$ µm/s. Also plotted is an integrated Gaussian distribution with $\sigma = 1.7$ mm, and the linear velocity profile following from Birks and Li's model using $L_0 = 3.6$ mm.*

from Birks and Li's model using the hot zone length $L_0 = 3.6$ mm obtained in Eq. (5.2), see Sec. 2.2.1. To no surprise we see that this deviates substantially from the measured velocity. It thus fits well with what we saw in Fig. 5.2 where their model failed in reproducing the measured fiber shape.

The linear velocity profile was obtained by assuming an uniform temperature distribution of the fiber, which implies a uniform viscosity of the fiber; infinity large at the frozen fiber section and finite inside the hot zone. Noting that a linear function is the integral of a constant function, it is interesting to see if an integrated Gaussian distribution for the inverse viscosity yields the same velocity profile as the measured. In the figure this is shown as the red dashed line using a width of $\sigma = 1.7$ mm in the Gaussian distribution. It follows the measured curve very closely and it seems reasonable to conclude that the inverse viscosity profile of the oven is very close to a Gaussian distribution with an effective hot zone length given by the width of the Gaussian roughly corresponding to the linear part of the velocity profile near the oven center at $z_c = 15$ mm.

7.2 Linear velocity profile

We now consider the special case of a linear velocity profile as in the simple heat-and-pull model by [Birks *et al.* 1992]. It is useful to see that the continuity equation yields the same result for the fiber shape when applying the same assumptions. We have:

$$v(z) = \begin{cases} v_- & \text{if } z \le z_-, \\ \frac{v_\infty}{L_0}(z - z_c) & \text{if } z_- < z < z_+, \\ v_+ & \text{if } z_+ \le z, \end{cases}$$

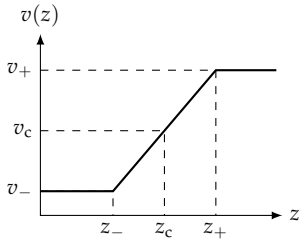

for the center point inside the hot zone $z_c = (z_+ - z_-)/2$. Chosing $z_0 = z_+$ in Eq. (7.3b) for the q-function we have:

$$q(z) = \begin{cases} \frac{v_\infty}{v_-}(z - z_-) + q(z_-) & \text{if } z \le z_-, \\ L_0 \ln\left(\frac{z - z_c}{z_+ - z_c}\right) & \text{if } z_- < z < z_+, \\ \frac{v_\infty}{v_+}(z - z_+) & \text{if } z_+ \le z. \end{cases} \tag{7.6}$$

We will now determine the fiber shape for the linear velocity profile using the formula introduced in Eq. (7.3a):

$$\frac{A(z,l)}{A_0} = \frac{\partial}{\partial z}\Big(q^{-1}\big(q(z) - l\big)\Big)\,. \tag{7.7}$$

From the boundary conditions, Fig. 6.2, we know that

$$\frac{A(z,l)}{A_0} = 1\,, \text{ for } z < \tilde{z}_- \text{ and } z > \tilde{z}_+. \tag{7.8}$$

In the following we will consider the range $z_- < z < \tilde{z}_+$, *i.e.*, the shape of the waist and right transition of the fiber. From Eq. (7.6) we find:

$$q^{-1}(x) = \begin{cases} (z_+ - z_c)\,\mathrm{e}^{x/L_0} + z_c & \text{if } x < 0, \\ \frac{v_+}{v_\infty}\,x + z_+ & \text{if } x \ge 0. \end{cases} \tag{7.9}$$

The sign of the argument in Eq. (7.7); $x = q(z) - l$, is negative for all $z_- < z < \tilde{z}_+$. Inserting Eq. (7.9) for $x < 0$ in Eq. (7.7) gives:

$$\frac{A(z,l)}{A_0} = \frac{\partial}{\partial z}\left(z_+ \, \mathrm{e}^{\,(q(z)-l)/L_0}\right) = \frac{q'(z)}{2} \, \mathrm{e}^{\,(q(z)-l)/L_0}\,, \tag{7.10}$$

where we used $z_+ - z_c = L_0/2$. In Sec. 2.2 we obtained the fiber shape for the specific case of symmetric pulls where $v_- = -v_+ < 0$ and $v_\infty = 2v_+ > 0$. Using this in Eq. (7.6) for $q(z)$ and solving the above equation we obtain the shape for the waist and right taper of the fiber:

$$\frac{A(z,l)}{A_0} = \begin{cases} \mathrm{e}^{-l/L_0} & \text{if } z_- < z < z_+, \\ \mathrm{e}^{-2(\tilde{z}_+ - z)/L_0} & \text{if } z_+ < z < \tilde{z}_+, \end{cases} \tag{7.11}$$

with $\tilde{z}_+ = z_+ + l/2$. The analysis is similar for the left transition, and will therefore not be repeated. Using; $r(z)/r_0 = \sqrt{A(z,t)/A_0}$, Eq. (7.11) yields exactly the same result as the model by [Birks *et al.* 1992], see Eq. (2.7). Thus encouraged we are ready to model our fiber shapes using the model developed in Sec. 7.1.

7.3 Shape analysis

In Sec. 5.1 we saw that the fiber shape is not well described by the simple heat-and-pull model assuming a linear velocity profile of the fiber flow. In the preceding sections we have therefore generalized the model resulting in the continuity equation. In order to solve for the fiber shape we have assumed the velocity profile to be time-independent but let it depend on the axial coordinate of the fiber contrary to the simple heat-and-pull model. In the following sections we compare the obtained model with the measured fiber shape. To recapitalize, the generalized flow model of the fiber shape $A(z,l)$ for stationary $v(z,t) = v(z)$ is given by Eq. (7.3) and Eq. (7.4);

$$A(z,l) = A_0 \, \frac{\partial}{\partial z}\left(q^{-1}\big(q(z) - l\big)\right), \tag{7.12a}$$

$$q(z) \equiv \int_{z_0}^{z} \frac{v_\infty}{v(\zeta)} \, \mathrm{d}\zeta\,, \tag{7.12b}$$

$$v\big(y(z,l)\big) = \frac{A(z,l)}{A_0} v(z)\,, \tag{7.12c}$$

$$y(z,l) = -\int_{z}^{\tilde{z}_+} \frac{A(\zeta,l)}{A_0} \, \mathrm{d}\zeta + z_+\,. \tag{7.12d}$$

7.3.1 Symmetric pull

We begin by comparing two velocity profiles obtained by applying the recursion formula (7.12c) for two different fibers, see Fig. 7.4. Both fibers were symmetrically pulled with speeds; $v_\pm = \pm 50$ μm/s. The fiber used to obtain the blue solid line was pulled by $l = 15$ mm, whereas the red dashed line was obtained from a pull with $l = 2$ mm. The two profiles are seen to match reasonably well. The blue curve is slightly more steep than the red. Apart from that the two curves follow each other very closely as expected from a time-independent velocity profile, *i.e.*, independent of the fiber elongation length.

Using the inferred velocity profile for the short, $l = 2$ mm, pulled fiber we now apply Eq. (7.12a) and Eq. (7.12b) to obtain the expected diameter of the fiber pulled by $l = 15$ mm; $\tilde{d}(z,l) = 2\sqrt{A(z,l)/\pi}$. This is plotted as the red dashed line in Fig. 7.5 with the measured fiber diameter given as the blue solid line. In

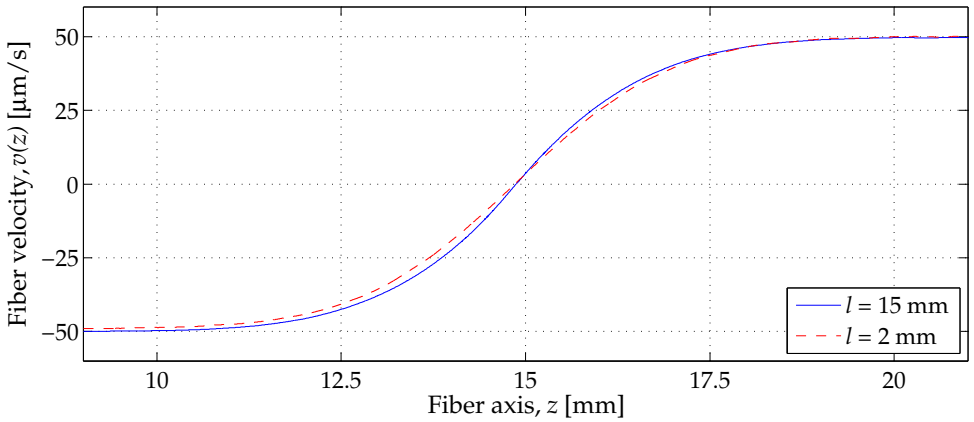

Figure 7.4: *Inferred velocity profiles of two symmetrically elongated fibers with measured shapes $A(z, l)$.*

contrary to the exponential tapers predicted by the simple heat-and-pull model, Sec. 5.1, this generalized model performs significantly better and qualitatively predicts the shape of the fiber. However, it fails severely in predicting the final

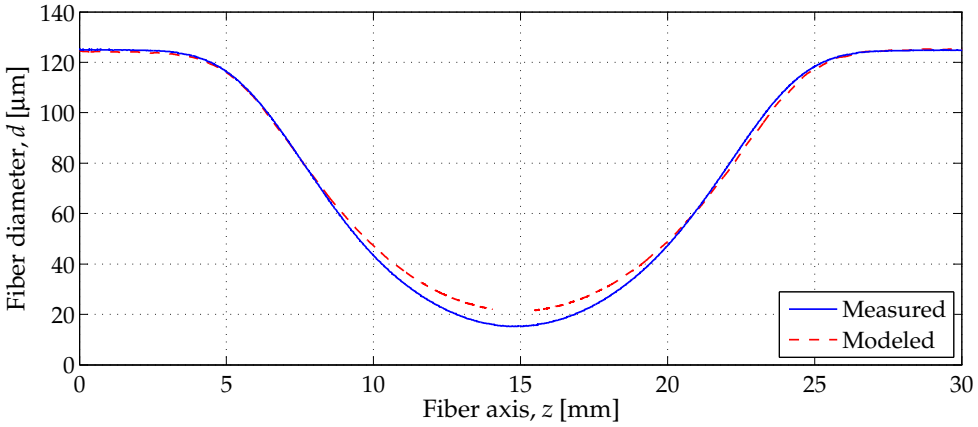

Figure 7.5: *Measured fiber diameter and the diameter predicted by the continuity equation for a time-independent velocity profile.*

waist size. Here the model yields $\tilde{d}_w \approx 20$ μm, about 30% above the measured value $d_w = 15$ μm. From Fig. 7.4 we found the long pull to give a steeper velocity profile than the short. This suggests that the effective hot zone length inside the oven shrinks during the pull, matching with the measured diameter being smaller than the modeled[2]. If this is the case, $v(z)$ cannot be regarded as independent of time, that is, independent of the changing fiber shape inside the hot zone. From the conservation of mass, the overestimated waist results in the tapered region to be longer in the modeled shape than observed in the measured.

For symmetric pulls $v(z)$ has a zero point inside the hot zone, see Fig. 7.4. This means that the q-function in Eq. (7.12b) has a singularity in that point. When calculating it we overcome this by setting the arbitrary zero-point z_0 to be explicitly at the singular point, such that $q(z = z_0)$ evaluates to zero instead of infinity. However, the calculation is of course still a bit unstable around this particular point. The two red dashed curves for the modeled shape do therefore

[2]Near the oven center the velocity profile can be approximated by a linear function. For the waist diameter we can thus apply the formula (2.6); $d_w = d_0 \exp\left(l/(2L_0)\right)$. A shorter hot zone L_0 therefore yields a smaller waist for a given pull length.

not meet at the waist. This might also explain why the model overestimates the waist size.

7.3.2 Asymmetric pull

Throughout the thesis we have so far only considered symmetrically elongated fibers. For optimizing the adiabaticity of the tapers, discussed in Sec. 2.3.1 and 4.1, as well as for tailoring the fiber shape according to any desired application, it is necessary to also consider more general pulling procedures, *i.e.*, $v_- \neq -v_+$, referred to as asymmetric pulls. An example of such a tapered fiber is shown in Fig. 7.6. Here the pull speeds were set to $v_- = 10$ μm/s and $v_+ = 100$ μm/s.

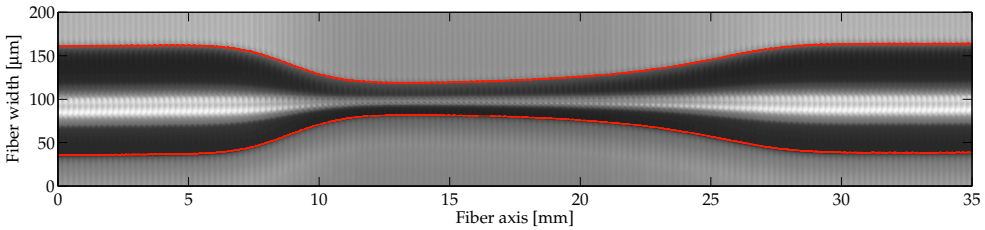

Figure 7.6: *Stacked CCD images of an asymmetrically elongated fiber. The two red curves are the detected fiber edges.*

Note that; $v_- > 0$, the fiber was thus pushed into the hot zone from the left and pulled out on the right with v_+, see Fig. 7.7. The total elongation length was $l = 15$ μm and fiber waist size was measured to $d_w = 38.6$ μm. The left taper is

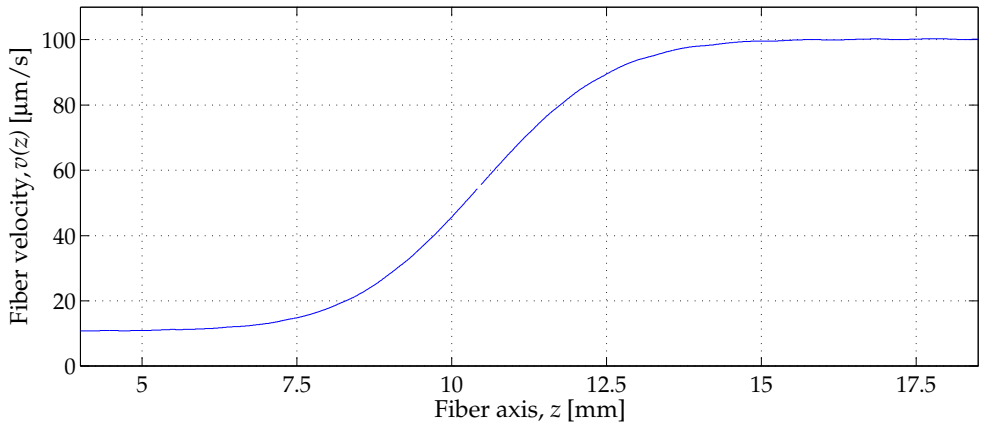

Figure 7.7: *Velocity profile used to model the shape of the asymmetric pulled fiber in Fig. 7.6. The boundary conditions $v_\pm$ have been imposed on the inferred $v(z)$ for the short pull in Fig. 7.4, by vertically translating and shrinking it. The horizontal translation are made to fit the fiber axis of the asymmetric fiber such that the minima for the measured and modeled diameters are located at the same axial position. The longitudinal axis for the symmetric and asymmetric fibers is thus not an absolute scale. Note that it can easily be made an absolute scale by recording the position of the camera when imaging the fiber and the position of the stages when pulling.*

observed to be much steeper and shorter than the right taper in agreement with the fiber being pushed in from the left side. Using the velocity profile in Fig. 7.7, in the equations for the fiber shape, (7.12a) and (7.12b), we obtain the red dashed curve in Fig. 7.8. As for the symmetric case, the modeled shape qualitatively matches the measured but fails in predicting the waist size and the length of the tapered region. With a modeled waist size of $\tilde{d}_w = 47.7$ μm it is thus off by 24% compared to the measured. Since both pull speeds where chosen positive; $v_\pm > 0$,

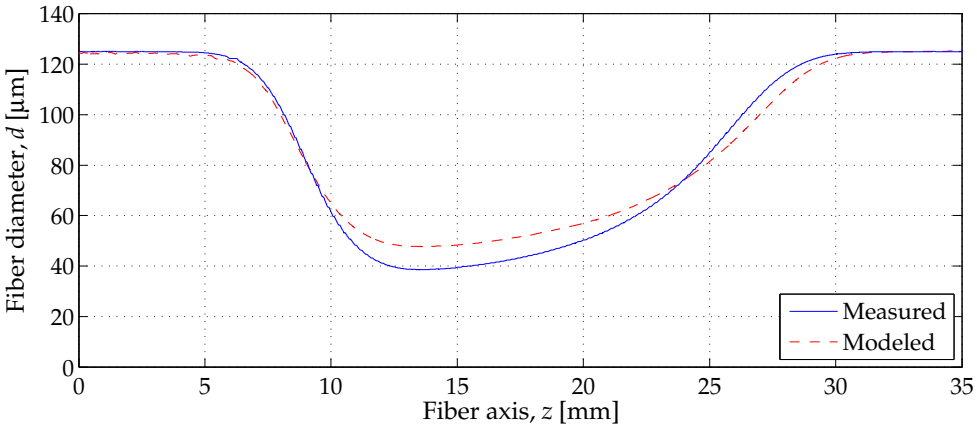

Figure 7.8: *Measured fiber diameter for an asymmetric pull and the corresponding predicted diameter by the continuity equation for a time-independent velocity profile.*

the velocity profile do not have any zero-crossing as evident from Fig. 7.7. This means that the q-function, Eq. (7.12b), is continuous for all z in contrary to the symmetric pull considered in Sec. 7.3.1. Because of the singularity in q for the symmetric pull it was hard to judge if the discrepancy between the modeled and measured waist was caused numerical instabilities or by invalid assumptions in the model. With a continuous q the model again overestimates the waist. This tendency has been observed consistently. It therefore seems that the quantitatively failure of the model is caused by the assumption of a time-independent axial fiber velocity rather than numerical instabilities. A flow model extended to include a time-dependent velocity profile thus seems to be required in order to model the fiber shape properly.

7.3.3 Asymmetric pull velocity profile

The continuity equation for stationary $v(z)$ has now been observed to yield qualitatively agreeing results of the measured fiber shape of two fibers pulled with different boundary conditions. However, quantitatively the model performance fails and cannot be used to, *e.g.*, infer the fiber waist size for a given pull length. The two examples considered in Sec. 7.3.1 and 7.3.2 used a velocity profile inferred from a short symmetric pull of the fiber. We have also seen that the velocity profiles obtained from two symmetrically pulled fibers with different pull lengths gave almost the same $v(z)$, Fig. 7.4.

It is interesting to see what an asymmetrically pulled fiber yields for the velocity profile. We therefore apply the recursion formula Eq. (7.12c) for the asymmetric fiber in Fig. 7.6. The result is shown in Fig. 7.9. As explained in Appendix C.3 the recursion formula can be applied from both the "+" (here right) side of the fiber, or the "-" (left) side. We can therefore obtain two curves for the inferred velocity profile of the asymmetric fiber. The red solid line was calculated from the "+" side, whereas the black dashed line was calculated from the "-" side. The blue dashed-dotted line is plotted as a reference of what was obtained from the short symmetrically pulled fiber. It is clear that the above results for $v(z)$ are wrong. The (push and) pull speeds are definitely known to be constant outside the hot zone; $v_- = 10$ μm/s and $v_+ = 100$ μm/s, whereas the model predicts oscillating velocities along the whole fiber axis.

The total pull length of the fiber were $l = 15$ mm. Together with $v_\pm$ this gives $l_- = 1.67$ mm and $l_+ = 16.67$ mm for the pull lengths on either side of the hot

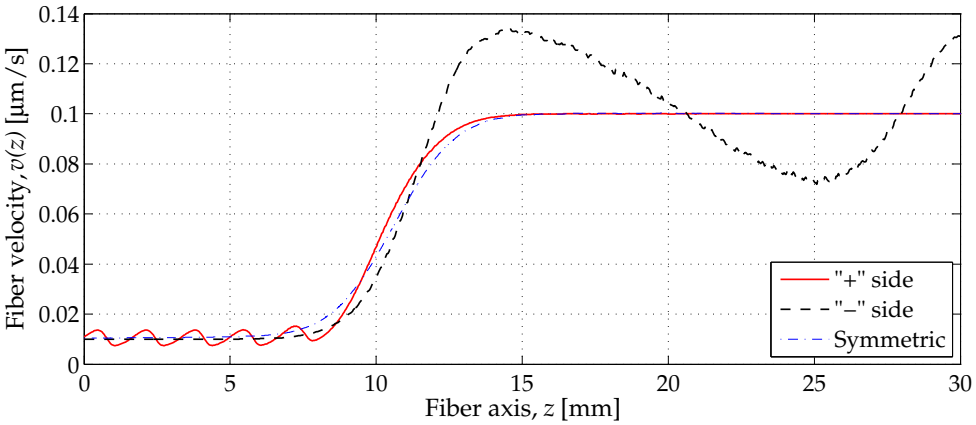

Figure 7.9: *Inferred velocity profile of an asymmetrically elongated fiber.*

zone[3]. This is observed to match the oscillatory frequency of the two inferred curves for the velocity profile. For a long time this lead us to believe that the un-physical results for $v(z)$ in Fig. 7.9 were caused by numerical instabilities rather than the time-independent assumption for $v(z)$ being wrong. In the following chapter we will show how to extend the model for an axially- and time-varying velocity profile of the fiber flow.s

7.4 Summary

In this chapter we have considered the continuity equation for time-independent but axially varying fiber velocity profile to model the resulting fiber shapes after a pull. In Fig. 7.4 the inferred velocity profiles for two different pull lengths were seen to slightly deviate from each other with the longer pulled fiber yielding a steeper and more narrow profile for $v(z)$. This was also found to be the case in [Pricking *et al.* 2010]. Here they used a slightly different form of the continuity equation and discussed the problem in terms of a "deformability" $\Theta(z)$ of the fiber instead of the velocity. However, if we identify:

$$\Theta(z) = \frac{\mathrm{d}}{\mathrm{d}z}\frac{v(z)}{v_\infty}, \tag{7.13}$$

it can be shown that their model corresponds to the model considered here. By parameterizing $\Theta(z)$ they empirically determined it for their heating device; a propane-butane-oxygen flame. They found $\Theta(z)$ to not only depend on their heater but also on the pull length of the fiber or equivalently the fiber shape. This would explain why the inferred velocity profiles obtained for two different pull lengths yields differ from each other. In Fig. 7.5 it became evident that the symmetric short pull $v(z)$ fails to quantitatively model the measured fiber shape of a longer symmetrically pulled fiber as well as an asymmetric pulled fiber, Fig. 7.8. Finally, inferring $v(z)$ from an asymmetrically pulled fiber directly gave a failure of the model predicting un-physical results for the velocity profile. For the asymmetric pull we note that the fiber shape is significantly different inside the hot zone than for a symmetric pulled fiber where the shape stays near cylindrical. If the fiber velocity depends on the current fiber shape this explains why the model perform worse for the asymmetric case than for the symmetric. We therefore conclude this chapter by asserting that the velocity profile cannot be regarded as a stationary function in time for our heater but depends on the momentary fiber shape.

[3]For l_- it would perhaps be more appropriate to call it a push length in this specific case. Note that $l = l_+ - l_-$.

Chapter 8

Fluid mechanics

From the preceding chapter it is evident that the assumption $v(z,t) = v(z)$ is not justified. When including time dependence in the fiber longitudinal velocity the continuity equation no longer has an analytic solution and has to be solved numerically. To obtain a model for the fiber shape we therefore need a description of the fiber flow. For this we have to consider the fluid dynamics in our system.

In a fluid the longitudinal speed with which the particles move is determined by viscous forces governed by the Navier-Stokes equations. In this chapter we start by deriving these equations for an incompressible fluid. In order to apply them for the fiber they are recast in cylindrical form while assuming an axially dependent viscosity. Afterwards the equations are approximated for thin free fluid strings and solved in the limit of creeping flow. In the end we obtain a set of two+one equations from which we can accurately model the fiber shape.

8.1 Navier-Stokes equations

In this section the Navier-Stokes equations for a viscous flow is given, closely following the literature by [Landau *et al.* 1987] and [Lautrup 2011]. Throughout this and the remaining sections we will apply the following conventions for matrix calculus:

$$\text{inner (dot) product:} \qquad \mathbf{a} \cdot \mathbf{b} = \mathbf{a}^T \mathbf{b}\,, \tag{8.1a}$$

$$\text{outer (tensor) product:} \qquad \mathbf{a} \otimes \mathbf{b} = \mathbf{a}\mathbf{b}^T\,. \tag{8.1b}$$

with all vector quantities considered as column vectors and $\mathbf{a}^T$ being the transpose of $\mathbf{a}$.

We consider an incompressible fluid with constant mass density ϱ and volume element $\mathrm{d}V = \mathrm{d}x\,\mathrm{d}y\,\mathrm{d}z$, see Fig. 8.1a. The total force acting on the volume element is comprised of body forces, *e.g.*, gravity, and of contact forces acting only on the surface elements $\mathrm{d}\mathbf{S}^T = (\mathrm{d}S_x, \mathrm{d}S_y, \mathrm{d}S_z)$. The latter can be described by the stress tensor:

$$\boldsymbol{\sigma}\big(\mathbf{x}(t), t\big) \overset{\text{cart}}{=} \begin{pmatrix} \sigma_{xx} & \sigma_{xy} & \sigma_{xz} \\ \sigma_{yx} & \sigma_{yy} & \sigma_{yz} \\ \sigma_{zx} & \sigma_{zy} & \sigma_{zz} \end{pmatrix}, \tag{8.2}$$

here in Cartesian coordinates. In the following we use the short hand notation $\boldsymbol{\sigma} \equiv \boldsymbol{\sigma}\big(\mathbf{x}(t), t\big)$ but it should be kept in mind that the stress tensor always depends on the volume element's position $\mathbf{x}(t)$ and time t. The diagonal elements in $\boldsymbol{\sigma}$ describe the normal forces per unit area, such as tension and pressure. The off-diagonal elements describe the tangential forces per unit area called the shearing

forces. In Fig. 8.1a this is illustrated for the stress acting on the surface element $\mathrm{d}S_z$. The two tangential forces are given by $\mathrm{d}F_x = \sigma_{xz}\mathrm{d}S_z$ and $\mathrm{d}F_y = \sigma_{yz}\mathrm{d}S_z$, while

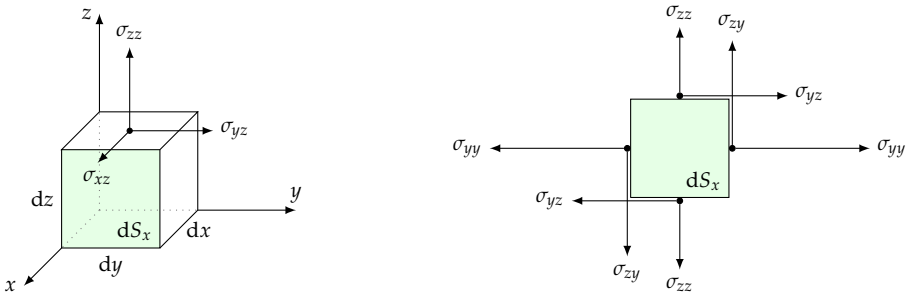

(a) Volume element $\mathrm{d}V$. Three force components is shown acting on the top surface $\mathrm{d}S_z$.

(b) Stress components acting on four faces of a volume element illustrating the symmetry of the stress tensor. Inspired by Fig. 31-9 in [Feynman *et al.* 2010].

Figure 8.1: *Stress tensor acting on a volume element* $\mathrm{d}V$ *of the fluid. The surface element* $\mathrm{d}S_x$*, marked in green in (a), is shown in front view in (b).*

the normal force is given by $\mathrm{d}F_z = \sigma_{zz}\mathrm{d}S_z$. The shearing forces arise from internal friction when the viscous fluid is flowing. From angular momentum conservation the stress tensor must be symmetric; $\boldsymbol{\sigma}^T = \boldsymbol{\sigma}$, see Fig. 8.1b. If the stress tensor were not symmetric we would have; $\sigma_{yz} \neq \sigma_{zy}$, and the resulting torque would make the volume element rotate.

From the above considerations the total force on the volume element can be written:

$$\mathbf{F} = \int_V \mathbf{f}\,\mathrm{d}V + \oint_S \boldsymbol{\sigma}\cdot\mathrm{d}\mathbf{S}\,, \tag{8.3a}$$

$$= \int_V \mathbf{f}\,\mathrm{d}V + \int_V \nabla\cdot\boldsymbol{\sigma}^T\,, \tag{8.3b}$$

where $\mathbf{f}^T = (f_x, f_y, f_z)$ is the body force density. It is convenient to describe the total force in terms of the effective force density instead; $\mathbf{F} = \int_V \mathbf{f}^*\,\mathrm{d}V$. We then have:

$$\mathbf{f}^* = \mathbf{f} + \nabla\cdot\boldsymbol{\sigma}^T\,, \tag{8.4a}$$

$$\begin{pmatrix} f_x^* \\ f_y^* \\ f_z^* \end{pmatrix} = \begin{pmatrix} f_x \\ f_y \\ f_z \end{pmatrix} + \begin{pmatrix} \partial_x\sigma_{xx} + \partial_y\sigma_{xy} + \partial_z\sigma_{xz} \\ \partial_x\sigma_{xy} + \partial_y\sigma_{yy} + \partial_z\sigma_{yz} \\ \partial_x\sigma_{xz} + \partial_y\sigma_{yz} + \partial_z\sigma_{zz} \end{pmatrix}, \tag{8.4b}$$

with the short hand notation for partial derivatives; $\partial_x = \partial/\partial x$, *etc.* In a viscous Newtonian fluid the shearing forces are proportional to the velocity gradients with the proportionality constant given by the viscosity[1] η [Lautrup 2011]. From symmetry we get for the off-diagonal elements, see Appendix D.1:

$$\sigma_{ij} = \sigma_{ji} = \eta\left(\frac{\partial u_i}{\partial x_j} + \frac{\partial u_j}{\partial x_i}\right) \quad \text{for } i,j = x,y,z \text{ and } i \neq j\,, \tag{8.5}$$

where $\mathbf{u}\big(\mathbf{x}(t), t\big)$ is the velocity field describing the motion of each volume element of the fluid. The forces normal to the surfaces originate from the pressure p. Additionally there can be friction due to compression modeled by the bulk

[1] Also called the shear viscosity or dynamic viscosity.

viscosity[2] ζ. We therefore get for the complete most general stress tensor:

$$\begin{aligned}\boldsymbol{\sigma} &= -p\mathbb{1} + \eta\Big(\nabla\otimes\mathbf{u} + (\nabla\otimes\mathbf{u})^T - \frac{2}{3}(\nabla\cdot\mathbf{u})\mathbb{1}\Big) + \zeta(\nabla\cdot\mathbf{u})\mathbb{1} \qquad (8.6)\\ &\overset{\text{cart}}{=} -p\mathbb{1} + \big(\zeta - \frac{2}{3}\eta\big)(\nabla\cdot\mathbf{u})\mathbb{1} + \eta\begin{pmatrix} 2\partial_x u_x & \partial_x u_y+\partial_y u_x & \partial_x u_z+\partial_z u_x)\\ \partial_x u_y+\partial_y u_x & 2\partial_y u_y & \partial_y u_z+\partial_z u_y)\\ \partial_x u_z+\partial_z u_x & \partial_y u_z+\partial_z u_y & 2\partial_z u_z\end{pmatrix}.\end{aligned}$$

Here the extra term $-\frac{2}{3}\eta(\nabla\cdot\mathbf{u})$ has been added to make $\boldsymbol{\sigma}$ traceless with respect to the viscosity η; $\mathrm{tr}\,(\boldsymbol{\sigma}) = -3(p - \zeta\nabla\cdot\mathbf{u})$. For an incompressible fluid we have; $\nabla\cdot\mathbf{u} = 0$, see Appendix D.2. Therefore all terms proportional to $\nabla\cdot\mathbf{u}$ vanish and $\mathrm{tr}\,(\boldsymbol{\sigma}) = -3p$. In this case:

$$\boldsymbol{\sigma} \overset{\text{cart}}{=} -p\mathbb{1} + \eta\begin{pmatrix} 2\partial_x u_x & \partial_x u_y+\partial_y u_x & \partial_x u_z+\partial_z u_x)\\ \partial_x u_y+\partial_y u_x & 2\partial_y u_y & \partial_y u_z+\partial_z u_y)\\ \partial_x u_z+\partial_z u_x & \partial_y u_z+\partial_z u_y & 2\partial_z u_z\end{pmatrix}. \qquad (8.7)$$

According to Newton's second law the volume element will be accelerated by the total forces acting on it. In terms of the effective force density this is given as:

$$\begin{aligned}\mathbf{f}^* &= \varrho\,\frac{\partial}{\partial t}\,\mathbf{u}\big(\mathbf{x}(t),t\big) &(8.8a)\\ &= \varrho\,\big(\partial_t + u_x\partial_x + u_y\partial_y + u_z\partial_z\big)\mathbf{u} &(8.8b)\\ &= \varrho\,\big(\partial_t + \mathbf{u}\cdot\nabla\big)\mathbf{u}\,. &(8.8c)\end{aligned}$$

Together with Eq. (8.4a) and Eq. (8.7) we obtain the Navier-Stokes equations for an incompressible fluid $\big(\nabla\cdot\mathbf{u} = 0\big)$:

$$\varrho\,\big(\partial_t + \mathbf{u}\cdot\nabla\big)\mathbf{u} = \mathbf{f} - \nabla p + \nabla\cdot\eta\Big(\nabla\otimes\mathbf{u} + (\nabla\otimes\mathbf{u})^T\Big)\,. \qquad (8.9)$$

From these three[3] equations the motion of any incompressible Newtonian fluid can be described as it equates the inertial forces (left hand side) to the body and viscous forces (right hand side) acting on each volume element. However, in general simple solutions do not exist. We therefore need to apply specific boundary conditions in order to obtain any useful description of the velocity field in the fiber.

8.1.1 Creeping flow

To simplify the Navier-Stokes equation we consider the Reynolds number *Re* of the fiber flow. This dimensionless parameter gives a measures of how viscous the flow is [Lautrup 2011, p. 253]:

$$\mathrm{Re} = \frac{\text{inertial forces}}{\text{viscous forces}}\,. \qquad (8.10)$$

A low Reynolds number thus indicate flow mainly dominated by internal friction, also known as creeping flow. In this viscous regime the flow is smooth and laminar with no turbulence. To estimate the Reynolds number the above formula can be approximated to:

$$\mathrm{Re} \approx \frac{\varrho\,\big|(\mathbf{u}\cdot\nabla)\mathbf{u}\big|}{\eta\,|\nabla^2\mathbf{u}|} \approx \frac{\varrho u L}{\eta}\,, \qquad (8.11)$$

[2] Also called the second viscosity, the volume viscosity or the expansion viscosity.
[3] Four when including $\nabla\cdot\mathbf{u} = 0$.

where $u = |\mathbf{u}|$ is the typical magnitude of the velocity over a region of the fluid with characteristic length scale L. In fiber pulling the viscous fluid is made of soft glass with $\varrho = 2.2\ \mathrm{g/cm^3}$ and $\eta = 100\ \mathrm{GPa \cdot s}$ at a temperature of $T = 1500^\circ C$ [Martienssen *et al.* 2006]. The fiber is typically pulled at speed $u = 100\ \mu\mathrm{m/s}$ and the oven length is $L = 20$ mm. This yields for the Reynolds number; $\mathrm{Re} \approx 10^{-14} \ll 1$, and we see that the fiber flow is highly viscous.

With the dominating force being the viscous forces, the inertial (acceleration-) forces acting on the volume elements can be neglected in the Navier-Stokes equations (8.9). The same is true for the only volume force present, namely gravity; $\mathbf{f} = \varrho\mathbf{g}$. The Navier-Stokes equations for an incompressible fluid thus reduce to:

$$0 = -\nabla p + \nabla \cdot \eta\Big(\nabla \otimes \mathbf{u} + (\nabla \otimes \mathbf{u})^T\Big)\,, \tag{8.12a}$$

$$0 = \nabla \cdot \mathbf{u}\,. \tag{8.12b}$$

This situation is referred to as Stokes flow. In such a flow the velocity field $\mathbf{u}\big(\mathbf{x}(t), t\big)$ is instantaneously determined by the boundary conditions alone.

8.1.2 Axisymmetric flow in cylindrical coordinates

In the following Eq. (8.12a) is written in cylindrical coordinates (ρ, ϕ, z), while assuming an axisymmetric flow; $\mathbf{u}\big(\rho(t), \phi(t), z(t), t\big) = \mathbf{u}\big(\rho(t), z(t), t\big)$ and $u_\phi = 0$. In cylindrical coordinates the basis vectors $\{\hat{\mathbf{e}}_\rho, \hat{\mathbf{e}}_\phi, \hat{\mathbf{e}}_z\}$ depend on the coordinates. Rewriting the Eq. (8.7) and Eq. (8.12a) is therefore a little cumbersome and can be done with *Mathematica*. To simplify the resulting expressions multiples of $\nabla \cdot \mathbf{u} = 0$ have been added to some of the expressions, and we have assumed that the viscosity alone depends on the longitudinal coordinate; $\eta(\rho, \varphi, z) = \eta(z)$. In cylindrical coordinates the stress tensor Eq. (8.7) takes the form[4]:

$$\boldsymbol{\sigma} \overset{\text{cyl}}{=} -p\mathbb{1} + \eta \begin{pmatrix} 2\partial_\rho u_\rho & 0 & \partial_z u_\rho + \partial_\rho u_z \\ 0 & \frac{2}{\rho} u_\rho & 0 \\ \partial_z u_\rho + \partial_\rho u_z & 0 & 2\partial_z u_z \end{pmatrix}. \tag{8.13}$$

From Eq. (8.12) we obtain the cylindrical form of the Navier-Stokes equations for Stokes-flow[5]:

$$0 = -\nabla p + \nabla \cdot \eta\Big(\nabla \otimes \mathbf{u} + (\nabla \otimes \mathbf{u})^T\Big) \tag{8.14a}$$

$$\overset{\text{cyl}}{=} \begin{pmatrix} \left(\eta\partial_\rho^2 + \eta\partial_z^2 + \eta'\partial_z - \frac{\eta}{\rho^2} + \frac{\eta}{\rho}\partial_\rho\right) u_\rho + \eta'\partial_\rho u_z - \partial_\rho p \\ 0 \\ \left(\eta\partial_\rho^2 + \eta\partial_z^2 + \eta'\partial_z + \frac{\eta}{\rho}\partial_\rho\right) u_z - \eta'\partial_\rho u_\rho - \frac{\eta'}{\rho} u_\rho - \partial_z p \end{pmatrix}, \tag{8.14b}$$

$$0 = \nabla \cdot \mathbf{u} \overset{\text{cyl}}{=} \left(\frac{1}{\rho} + \partial_\rho\right) u_\rho + \partial_z u_z\,, \tag{8.14c}$$

where $\eta' \equiv \mathrm{d}\eta/\mathrm{d}z$.

8.2 Solving the Navier-Stokes equations for the fiber

The Navier-Stokes equations obtained for an incompressible axisymmetric creeping flow (8.14) constitute a set of coupled non-linear partial differential equations

[4] This expression can also be found in [Landau *et al.* 1987, p. 48].

[5] Here and in the following sections all primes refer to the derivative with respect to z unless otherwise stated.

of the fiber velocity field $\mathbf{u}\big(\mathbf{x}(t),t\big)$. We want to solve these equations for the longitudinal flow component $v(z,t) = u_z(z,t)$, such that we can use it together with the continuity equation (6.3):

$$-\frac{\partial}{\partial t}A(z,t) = \frac{\partial}{\partial z}\Big(A(z,t)\,v(z,t)\Big)\,, \tag{8.15}$$

to model the fiber shape $A(z,t)$. In this section we show how to solve Eq. (8.14) by applying appropriate boundary conditions corresponding to the fiber pulling flow.

8.2.1 Surface forces

Let $r(z)$ describe the radius of the fiber as a function of the longitudinal position, see Fig. 8.2. Then the longitudinal-tangential $\hat{\mathbf{t}}$ and normal $\hat{\mathbf{n}}$ unit vectors with respect to the fiber surface are given by:

$$\hat{\mathbf{t}} \overset{\text{cyl}}{=} \frac{1}{\sqrt{1+r'(z)^2}}\begin{pmatrix} r'(z) \\ 0 \\ 1 \end{pmatrix}, \tag{8.16a}$$

and:

$$\hat{\mathbf{n}} \overset{\text{cyl}}{=} \frac{1}{\sqrt{1+r'(z)^2}}\begin{pmatrix} 1 \\ 0 \\ -r'(z) \end{pmatrix}, \tag{8.16b}$$

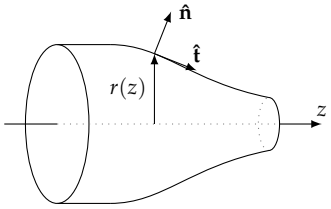

Figure 8.2: *The normal and longitudinal-tangential unit vectors on the fiber surface.*

We now follow closely the derivations in [Eggers *et al.* 1994]. To find the velocity field $\mathbf{u}\big(\mathbf{x}(t),t\big)$ we need to specify the boundary conditions of the flow. The tangential force is calculated by[6]:

$$\hat{\mathbf{n}}\cdot\boldsymbol{\sigma}\cdot\hat{\mathbf{t}} = \eta\frac{2r'(\partial_\rho u_\rho - \partial_z u_z) + (1-r'^2)(\partial_\rho u_z + \partial_z u_\rho)}{1+r'^2}\bigg|_{\rho=r} = 0\,, \tag{8.17a}$$

and the normal force by:

$$\hat{\mathbf{n}}\cdot\boldsymbol{\sigma}\cdot\hat{\mathbf{n}} = -p + 2\eta\frac{r'^2\partial_z u_z + \partial_\rho u_\rho - r'(\partial_z u_\rho + \partial_\rho u_z)}{1+r'^2}\bigg|_{\rho=r} = 0\,. \tag{8.17b}$$

The last equality in both expressions follows since fiber surface is free[7] and therefore neither tangential nor normal forces act on the surface (in contrast to [Eggers *et al.* 1994] we neglect surface tension in our treatment). Together with a Taylor expansion of the velocity field, derived in next section, these equations will be used in the cylindrical Navier-Stokes equations for Stokes flow. In this manner a simple expression for the longitudinal velocity component of the fiber flow can be obtained.

8.2.2 Thin fiber approximation

The optical fiber is a very thin and long cylinder. We can therefore express $u_\rho(\rho,z)$, $u_z(\rho,z)$ and $p(\rho,z)$ as a Taylor series in ρ about the fiber axis $\rho = 0$. In

[6] What is calculated is really the stress component pointing in the direction of the tangential force $\hat{\mathbf{t}}$ and acting on the surface element with normal vector $\hat{\mathbf{n}}$; $\sigma_{tn} = \mathrm{d}F_t/\mathrm{d}S_n = \hat{\mathbf{n}}\cdot\boldsymbol{\sigma}\cdot\hat{\mathbf{t}}$. Similarly for the normal component $\sigma_{nn} = \mathrm{d}F_n/\mathrm{d}S_n = \hat{\mathbf{n}}\cdot\boldsymbol{\sigma}\cdot\hat{\mathbf{n}}$.

[7] In the sense that the fiber is not flowing inside a tube.

the approximation of axisymmetric flow[8], we find for the velocity field:

$$\mathbf{u}(\rho,z) = \begin{pmatrix} u_\rho(\rho,z) \\ u_\phi(\rho,z) \\ u_z(\rho,z) \end{pmatrix} = \begin{pmatrix} -u_0'(z)\frac{\rho}{2} - u_2'(z)\frac{\rho^3}{4} \\ 0 \\ u_0(z) + u_2(z)\rho^2 \end{pmatrix} + \mathcal{O}(\rho^4), \tag{8.18}$$

with the Taylor coefficients given by:

$$u_n(z) = \frac{1}{n!}\partial_\rho^n u_z(\rho,z)\Big|_{\rho=0}. \tag{8.19}$$

Similarly we find for the pressure:

$$p(\rho,z) = p_0(z) + p_2(z)\rho^2 + \cdots. \tag{8.20}$$

The u_1-term proportional to ρ is set to zero in order to have $\partial_\rho u_z$ continuous and differentiable at all ρ, see Fig. 8.3. The latter is necessary since the stress tensor is given by the velocity gradients. The same holds for the p_1-term. Note that

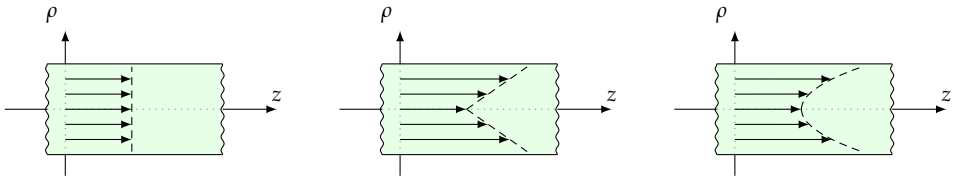

(a) $u_z(\rho,z) = u_0$. (b) $u_z(\rho,z) = u_0 + u_1\rho$. (c) $u_z(\rho,z) = u_0 + u_2\rho^2$.

Figure 8.3: *Longitudinal cross-section of the fiber illustrating the flow for the three lowest orders of the Taylor expansion. The horizontal arrows indicate the magnitude and direction of the velocity component along the fiber axis for laminar axisymmetric flow. The dashed lines give the dependence of u_z with respect to the radial component ρ, and are seen to be everywhere continuous and differentiable except in (b) where it is not diffentiable on the fiber axis.*

the expression in u_ρ is given in terms of the derivatives of the Taylor coefficients for the u_z expansion in Eq. (8.18). This complicated expression, containing only odd orders in ρ, is obtained by inserting the Taylor expansions of u_ρ and u_z into Eq. (8.14c) governing the fluid incompressibility for axisymmetric flow. The derivation can be found in Appendix D.3.

Exactly as in [Eggers *et al.* 1994] we now insert the Taylor expansions (8.18) and (8.20) into Eq. (8.17b) and Eq. (8.17a) for the normal and tangential surface forces. From Eq. (8.17b) we get an expression for $p_0(z)$ to lowest order in r:

$$p_0 = \frac{\eta}{1+r'^2}\Big(-u_0' + 2r'^2u_0' + rr'(u_0'' - 4u_2)\Big) \tag{8.21a}$$

$$\overset{\mathcal{O}(r,r')}{\approx} -\eta u_0', \tag{8.21b}$$

where we have made use of the gradual taper slopes; $r' \ll 1$, in the last equality. Similarly we can isolate $u_2(z)$ to first order in r and r' from Eq. (8.17a):

$$u_2 = \frac{3r'}{2r}\Big(1 - r'\Big)u_0' + \frac{7}{4}rr'(1-r'^2)u_2' + \frac{1}{4}u_0'' + \frac{r^2}{8}u_2'' \tag{8.22a}$$

$$\overset{\mathcal{O}(r,r')}{\approx} \frac{1}{2r}\left(3r'u_0' + \frac{1}{2}ru_0''\right). \tag{8.22b}$$

[8] That is, $\mathbf{u}\big(\mathbf{r}(t),t\big) = \mathbf{u}\big(\rho(t),z(t),t\big)$ and $u_\phi = 0$.

Eq. (8.21b) and Eq. (8.22b) can now be used to eliminate p_0 and u_2 from the z-component in the Navier-Stokes equations (8.14b) for Stokes flow. Inserting Eq. (8.18) and Eq. (8.20) with the above approximations we thus obtain, see Appendix D.4:

$$0 = 3\frac{(\eta r^2 u_0')'}{r^2}\,. \tag{8.23}$$

This differential equation for the longitudinal velocity of the fiber can be numerically solved together with the continuity equation (8.15) if the viscosity of the fiber $\eta(z)$ is known. To model the fiber shape we therefore need to obtain the axial viscosity of the fiber. In the work by [Baker *et al.* 2011] they solved the two equations by choosing the viscosity to be a uniform function. With this they found very good agreement between the modeled and measured shape of their fibers. However, a uniform viscosity implies a uniform temperature distribution, which we already saw in Fig. 5.2 does not describe the shape of our fibers. In fact, from the inferred velocity profile in Fig. 7.3 it seems more plausible that the inverse viscosity distribution of the oven is near that of a Gaussian. With this information we could choose the viscosity profile accordingly and solve Eq. (8.23) and Eq. (8.15) for the fiber shape. Actually, we can do a bit better. From Eq. (8.23) we can obtain an expression for the axial flow of the fiber, since:

$$0 = 3\frac{(\eta r^2 u_0')'}{r^2} \tag{8.24a}$$

$$\Rightarrow \eta r^2 u_0' = C(t)\,, \tag{8.24b}$$

where $C(t)$ is spatially constant but may depend on time. By simple integration of Eq. (8.24b) we find:

$$u_0(z,t) - u_0(z_0,t) = C(t)\int_{z_0}^{z} \frac{1}{\eta(\zeta) r^2(\zeta,t)}\,\mathrm{d}\zeta\,, \tag{8.25}$$

for arbitrary z_0. From this equation it is possible to infer $\eta(z)$ by applying the recursion formula (7.4) derived in Sec. 7.1. This is the main objective of Sec. 8.3. Knowing the viscosity of the fiber it can be used directly in Eq. (8.25) which together with the continuity equation (8.15) can be solved to yield the fiber shape for given boundary conditions.

8.3 Fiber viscosity

Before we show how to infer the axial distribution of the fiber viscosity we present a brief summary of what we did in the preceding sections. We started by deriving the general Navier-Stokes equations (8.9) for an incompressible fluid. The equations were then simplified by imposing the Stokes flow approximation and afterwards recast into cylindrical form while applying the approximation of axisymmetric flow. These reduced Navier-Stokes equations could then be solved by applying the boundary conditions of the fiber. This included free surface forces, negligible surface tension, and Taylor expansion of the pressure and velocity field about the fiber axis. To first order in the fiber radius we thus obtained the longitudinal velocity profile of the fiber $v(z,t) = u_z(\rho = 0, \phi, z, t) = u_0(z,t)$ as desired, Eq. (8.25):

$$v(z,t) = v(z_0,t) + C(t)\int_{z_0}^{z} \frac{1}{\eta(\zeta) r^2(\zeta,t)}\,\mathrm{d}\zeta\,. \tag{8.26}$$

We now show how the viscosity of the fiber can be inferred from this equation. We start by introducing a convenient function describing the "deformability" of

the fiber:

$$\tau(z) = \frac{\frac{1}{\eta(z)}}{\int_{-\infty}^{\infty} \frac{1}{\eta(\zeta)}\,\mathrm{d}\zeta}\,. \tag{8.27}$$

With this, and using the fiber cross-section $A(z,t) = \pi r^2(z,t)$, we rewrite Eq. (8.26):

$$v(z,t) = v(z_0,t) + \widetilde{C}(t)\int_{z_0}^{z} \frac{A_0}{A(\zeta,t)}\tau(\zeta)\,\mathrm{d}\zeta\,. \tag{8.28}$$

The constant of integration $\widetilde{C}(t)$ can be determined from the boundary conditions (6.4) by requiring; $v(z_\pm,t) = v_\pm$, at all times t:

$$\begin{aligned} v(z_+,t) - v(z_-,t) &= v_+ - v_- \\ &= \widetilde{C}(t)\left(\int_{z_0}^{z_+} \ldots\,\mathrm{d}\zeta - \int_{z_0}^{z_-} \ldots\,\mathrm{d}\zeta\right) \\ &= \widetilde{C}(t)\int_{z_-}^{z_+} \frac{A_0}{A(\zeta,t)}\tau(\zeta)\,\mathrm{d}\zeta\,. \end{aligned} \tag{8.29}$$

From this we obtain the longitudinal velocity profile of the fiber for all times t:

$$v(z,t) = v(z_0,t) + v_\infty \cdot \frac{\int_{z_0}^{z} \frac{A_0}{A(\zeta,t)}\tau(\zeta)\,\mathrm{d}\zeta}{\int_{z_-}^{z_+} \frac{A_0}{A(\zeta,t)}\tau(\zeta)\,\mathrm{d}\zeta}\,. \tag{8.30}$$

This expression, together with the continuity eqaution (8.15), are the central equations for modeling the fiber shape. In order to obtain the viscosity, or equivalently $\tau(z)$ in Eq. (8.27), we note that for $t = 0$ Eq. (8.30) reduces to:

$$v(z,0) = v(z_0) + v_\infty \int_{z_0}^{z} \tau(\zeta)\,\mathrm{d}\zeta\,. \tag{8.31}$$

Here we used that $\tau(z)$ is zero outside the range $[z_-, z_+]$, since the viscosity is infinitely large for the frozen fiber. The integral in the denominator of Eq. (8.30) can then be extended to the range $[-\infty,\infty]$ which is trivial to compute since $\tau(z)$ is normalized. Taking the derivative of Eq. (8.31) we find:

$$\tau(z) = \frac{\mathrm{d}}{\mathrm{d}z}\frac{v(z,0)}{v_\infty}\,. \tag{8.32}$$

For small times, or equivalently, for short fiber elongations, the fiber shape does not change significantly; $A(z, t \text{ small}) \approx A(z,0) = A_0$. From Eq. (8.30) the velocity profile can then be regarded as stationary in time; $v(z, t \text{ small}) \approx v(z)$, and inferred using the recursion formula (7.4). We can therefore infer $\tau(z)$ by applying the approximation:

$$\tau(z) \approx \frac{\mathrm{d}}{\mathrm{d}z}\frac{v(z)}{v_\infty}\,, \qquad \text{for small } t\,. \tag{8.33}$$

The result is shown as the blue solid curves in Fig. 8.4 using $v(z)$ inferred from a short symmetric pull, see Fig. 7.4. In Fig. 8.4b $\tau(z)$ has been smoothed by performing a moving average over 230 out of 10 000 data points and normalized by dividing the curve by its integral over the whole range. The red dashed line shows a Gaussian fit of $\tau(z)$ yielding $\sigma = 1.8$ mm. This is in agreement with the observations made in Fig. 7.3 for the inferred velocity profile. Here we suggested a Gaussian distribution with $\sigma = 1.7$ mm to resemble the inverse viscosity distribution. With this encouraging result for $\tau(z)$ we are ready to model the fiber shape in Sec. 8.4.

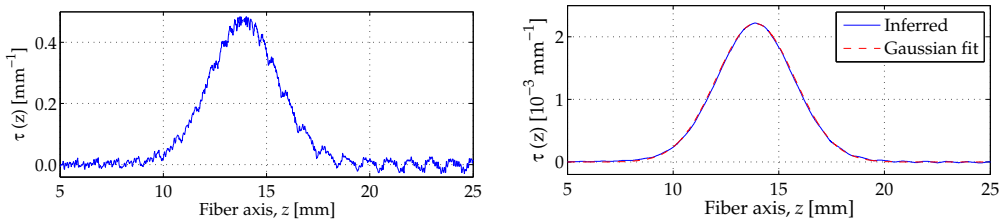

(a) Raw data. (b) Smooth and normalized.

Figure 8.4: *Inferred* $\tau(z)$.

8.4 Shape analysis

In the preceding sections we used fluid dynamics to generalize the fiber flow model to all times and axial positions of an arbitrary pulling procedure using constant pull speeds outside the hot zone. This was motivated first by the results obtained in Sec. 5.1, using the simple heat-and-pull model, and then in Sec. 7.3, with the model generalized to include the inferred axial velocity profile assumed stationary in time. While the latter qualitatively modeled the fiber shape it was clear that the assumption $v(z,t) = v(z)$ was invalid causing the model to fail in predicting the shape quantitatively.

Starting from the Navier-Stokes equations we have now obtained a flow model generalized to all times and axial positions to describe the fiber shape. This consists of the two equations:

$$-\frac{\partial}{\partial t}A(z,t) = \frac{\partial}{\partial z}\Big(A(z,t)\,v(z,t)\Big)\,, \tag{8.34a}$$

$$v(z,t) = v(z_0,t) + v_\infty \cdot \frac{\int_{z_0}^{z} \frac{A_0}{A(\zeta,t)}\tau(\zeta)\,\mathrm{d}\zeta}{\int_{z_-}^{z_+} \frac{A_0}{A(\zeta,t)}\tau(\zeta)\,\mathrm{d}\zeta}\,. \tag{8.34b}$$

The first equation is the continuity equation of the fiber shape derived in Sec. 6.1 and the second describes the longitudinal velocity profile of the fiber, Eq. (8.30). A solution for the fiber shape can now be obtained by solving these two equations numerically together with deformability $\tau(z)$ given by Eq. (8.33). In the following we will apply these equations to model the fiber shape and compare the results with the measured shape for different pulling conditions of the fiber given by $v_\pm$ and l. Unless otherwise stated all the modeled shapes are made using the smoothed and normalized curve for the inferred $\tau(z)$ in Fig. 8.4b. With this the two Eq. (8.34a) and Eq. (8.34b) are numerically solved in MATLAB using the `ode45`-function.

8.4.1 Linear velocity profile

It is always encouraging to test a model in a limit where the behavior is well known. We therefore start with a sanity check of the model by choosing $\tau(z)$ explicitly to be a box-shaped function, see inset in Fig. 8.5. This corresponds to a uniform viscosity profile which implies a box-shaped temperature distribution. This means that the velocity profile must be linear inside the hot side and constant outside as seen directly from Eq. (8.33) as well as in Sec. 2.2.1. The modeled shape should therefore reproduce the results obtained from the model by [Birks *et al.* 1992]. The width of $\tau(z)$ is set to the inferred hot zone length $L_0 = 3.6$ mm as found in Sec. 5.1. The blue curve in Fig. 8.5 is obtained from the same measured fiber as used in Sec. 5.1, that is, a fiber symmetrically elongated by $l = 15$ mm

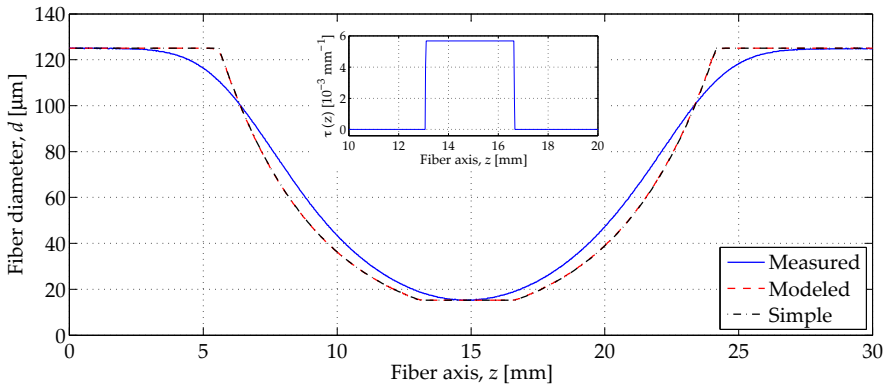

Figure 8.5: *Measured fiber diameter modeled by the continuity equation using a linear velocity profile like the simple heat-and-pull model.*

using $v_{\pm} = \pm 50$ μm/s. The red dashed line is the modeled curve from the above Eq. (8.34), while the black dashed-dotted line is obtained used Eq. (5.1) from the simple heat-and-pull model. The two modeled curves are observed to lie exactly on top of each other as expected. With the generalized model confirmed in the limit of stationary linear flow we continue the analysis using the inferred deformability $\tau(z)$ in Fig. 8.4b.

8.4.2 Symmetric pull

Using the same fiber as in Fig. 8.5 we now present the performance of the model generalized to all times and axial positions in Fig. 8.6. It is observed to follow

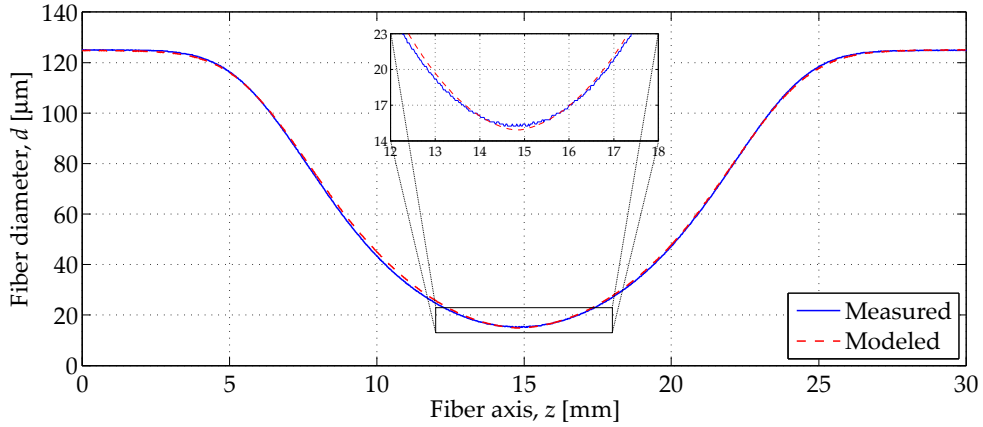

Figure 8.6: *Measured fiber diameter modeled by the continuity equation for a time-dependent axially varying velocity profile using Eq. (8.34) and $\tau(z)$ from Fig. 8.4b.*

the measured curve very closely over the whole range of the fiber. For the waist diameter the model yields; $\tilde{d}_w = 14.9$ μm, differing only 2% from the measured diameter; $d_w = 15.2$ μm. This is a significant improvement compared to the flow model using a stationary velocity profile where we found the modeled waist to be off by 30%, see Fig. 7.5.

8.4.3 Asymmetric pull

The model given by Eq. (8.34) is not restricted to symmetric pulls but can be applied to all boundary conditions with constant pull speeds. We therefore now consider the performance for an asymmetric pulled fiber like in Sec. 7.3.2. For the same fiber used in Fig. 7.8 we obtain the red dashed curve for the modeled

fiber shape in Fig. 8.7. Like the symmetric case considered in Fig. 8.6 the model

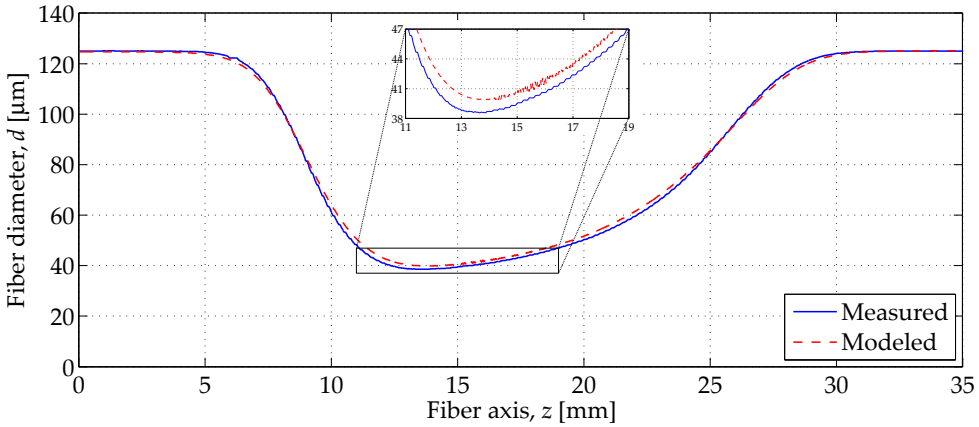

Figure 8.7: *Measured fiber diameter modeled by the continuity equation for a time and axially varying velocity profile. The fiber was asymmetrically elongated by* $l = 15$ mm *using pull speeds* $v_- = 10$ μm/s *and* $v_+ = 100$ μm/s.

follows the measured curve very closely and significantly better than the model for stationary $v(z)$. The waist sizes now only differ by 3% for the measured diameter $d_w = 38.6$ μm, and a modeled diameter of $\tilde{d}_w = 39.9$ μm, see inset. In comparison the model for stationary $v(z)$ gave a 24% discrepancy.

To test the consistency of the model we show in Fig. 8.8 another asymmetrically pulled fiber but with different boundary conditions. Again, we observe good agreement between the measured and modeled curves for the fiber shape. Note,

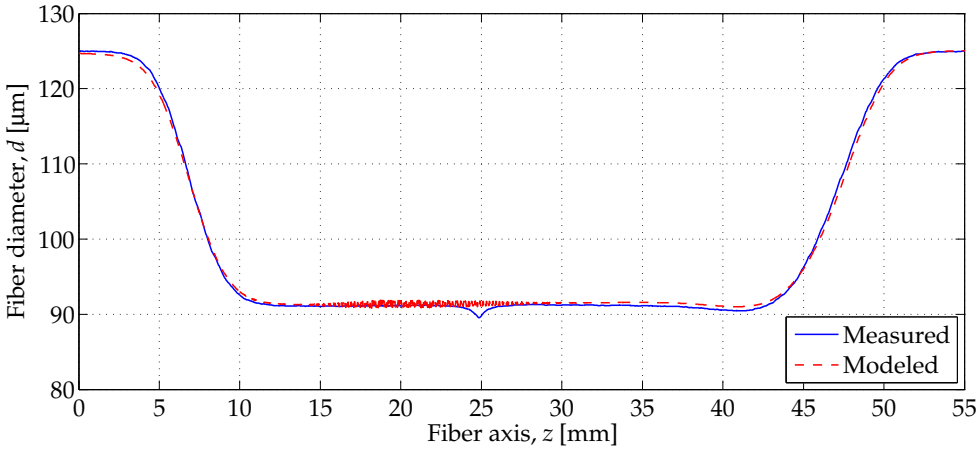

Figure 8.8: *Measured fiber diameter modeled by the continuity equation for a time-dependent velocity profile. The fiber was asymmetrically elongated by* $l = 19$ mm *using pull speeds* $v_- = 0.8$ mm/s *and* $v_+ = 1.5$ mm/s. *Note that the y-axis only goes down to* $d = 80$ μm. *The observed dip of the fiber diameter at* $z = 25$ mm *is most likely caused by a crack in the fiber.*

that the even though the fiber was elongated more than the fiber shown in Fig. 8.7 its final waist size is considerably larger. This can be explained by the ratio of the pull speeds. When a fiber is being "pushed-pulled", such that $v_\pm > 0$, a steady-state solution of the continuity equation can be applied; $\partial_t m = 0$. Meaning that the fiber mass entering the hot zone equals the mass leaving it. From Eq. (6.2) we thus find:

$$v_- A_- = v_+ A_+ \,, \tag{8.35}$$

where $A_\pm$ is the fiber cross-sectional areas on either side of the oven. From this an estimate of the waist diameter after the pulling procedure can be obtained, using $v_+ > v_- > 0$, $A_- = A_0 = \pi(d_0/2)^2$, and $A_+ = \pi(\tilde{d}_\mathrm{w}/2)^2$ we have:

$$\frac{\tilde{d}_\mathrm{w}}{d_0} = \sqrt{\frac{v_-}{v_+}}. \tag{8.36}$$

Both fibers considered in Fig. 8.7 and Fig. 8.8 were "pushed-pulled". Applying Eq. (8.36) we find:

$$\text{Fig. 8.7:} \qquad \tilde{d}_\mathrm{w} = 39.5\ \mu\mathrm{m}\,, \tag{8.37a}$$

$$\text{Fig. 8.8:} \qquad \tilde{d}_\mathrm{w} = 91.3\ \mu\mathrm{m}\,, \tag{8.37b}$$

in good agreement with the observed values.

8.4.4 Double pull

We now test the model further by applying it to a doubled pulled fiber according to the procedure in Table 8.1. The result for the measured fiber diameter is shown

Table 8.1: *Pulling procedure for a double pull.*

Step	Procedure
(i)	Drive oven in.
(ii)	Start 1st pull with; $v_- = -100\ \mu$m/s and $v_+ = -6\ \mu$m/s.
(iii)	After $l_1 = 2$ mm stop stages.
(iv)	Start 2nd pull with; $v_- = 6\ \mu$m/s and $v_+ = 100\ \mu$m/s.
(v)	After $l_2 = 33.3$ mm stop stages.
(vi)	Drive oven back.

as the blue curve in Fig. 8.9. The black dashed-dotted curve is the modeled shape after the first pull, whereas the red dashed curve is the modeled curve for the final fiber shape after step (v). The two pulls were performed right after each other and therefore the fiber shape after the 1st pull has not been measured. The model again show good agreement with the measured shape. For the right

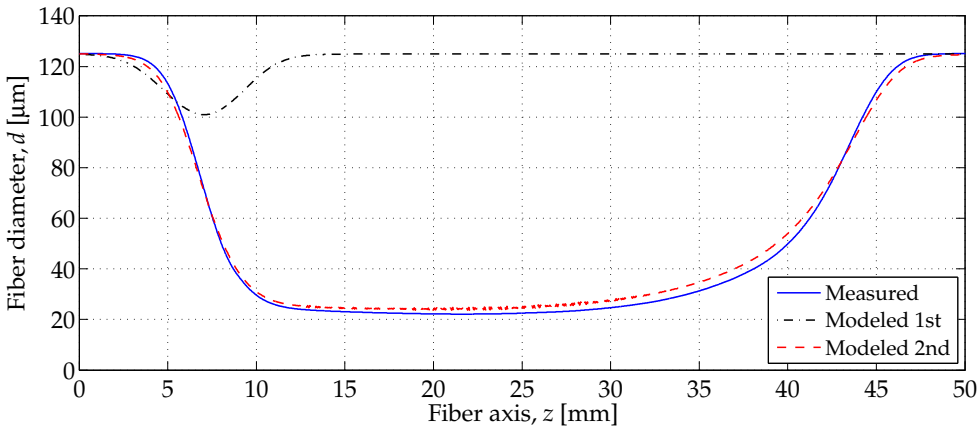

Figure 8.9: *Measured fiber diameter modeled by the continuity equation for a time-dependent velocity profile. The fiber was asymmetrically elongated twice.*

transition it is slightly off and predicts a less steep transition than measured.

8.5 Summary

In this chapter we started by obtaining the Navier-Stokes equations for an incompressible Newtonian fluid, Sec. 8.1. We next showed that the Reynolds is very small for the fiber flow. The Navier-Stokes equations could therefore be well-approximated by neglecting the inertial and body forces acting on the fluid. From this we obtained the equations governing Stokes flow, Sec. 8.1.1. To solve these equations they were first rewritten in the more appropriate frame of cylindrical coordinates under the assumption of axisymmetric flow, Sec. 8.1.2. By applying the boundary conditions of free surface forces and negligible surface tension of the fiber the equations for Stokes flow were further simplified, Sec. 8.2.1. The pressure and velocity field were then Taylor expanded about the fiber axis. This is valid for the long and thin cylindrical fluid we have for the fiber. Within these approximations the time-dependent longitudinal velocity profile were derived from the Stokes equations, Sec. 8.2.2. A model for the fiber shape was thus obtained consisting of the previously derived continuity equation and the velocity profile derived here, Eq. (8.34). If the fiber viscosity is a known function the model can be numerically solved to yield the fiber shape. Instead of approximating the viscosity with either a uniform or inverse Gaussian function we showed that it can be inferred by assuming the velocity profile to be stationary for short pulls of the fiber and by applying the method, developed in Sec. 7.1, for obtaining such a velocity profile, Sec. 8.3. Finally, we applied the model for various fibers pulled under different boundary conditions, Sec. 8.4. All the modeled curves for the fiber diameters were in good agreement with the measured fiber diameters obtained with the CCD imaging technique, Sec. 4.2.

Part III

Conclusion and outlook

Chapter 9

Conclusion

In this thesis we show how to produce sub-wavelength tapered optical fibers, characterize some of their important properties, and develop a model for the fiber shape, yielding very good agreement with the measured results. To produce the nanofibers we have implemented an all-computer controlled heat-and-pull rig. With this we can reproducibly make fibers tapered down to sub-micron diameters, confirmed by both CCD and SEM imaging.

An extensive analysis of their optical and spatial properties has been performed. The optical properties were obtained by analyzing the transmission signal of both a narrow- and broadband light source. Furthermore a frequency analysis of the transmission signal was carried out using the narrow-banded source. On average a 10% loss of the transmission is observed for fibers tapered down to ~ 0.5 μm from a fiber with an initial diameter of 125 μm. The main loss were ascribed to be caused by the excitation of higher-order cladding modes in the fiber when the fundamental mode undergoes the core-cladding transition. We therefore conclude that the tapers are not fully adiabatic and should be optimized according to the adiabatic criteria by [Love *et al.* 1986; Love *et al.* 1991]. For fully adiabatic tapers we expect to obtain transmissions well above 95%. Observing that the fibers start bending when pulled below 10 μm might also induce losses in the tapers. Therefore this effect should also be handled in future optimization of the adiabaticity. For the spatial properties the fiber shapes have been obtained from CCD images of the fiber using an edge-detection algorithm. The obtained results for the fiber shape have been confirmed by SEM images.

To model the resultant fiber shape after pulling we have applied three different models. Starting with the model by [Birks *et al.* 1992] we clearly observed that it does not predict the shape of our nanofibers. The failure is caused by the simplifying assumption of a uniform temperature distribution, implying a uniform viscosity and a linear axial velocity profile inside the hot zone, which do not apply to our heater.

In order to obtain a more general model for the fiber shape we derived the continuity equation by considering the flow of the fiber. Assuming a non-linear axially varying velocity profile stationary in time an analytic solution for the fiber shape was obtained. By inverting this solution we showed how to infer the longitudinal velocity of the fiber flow from the measured fiber shape. The inferred velocity profile could then be generalized according to the specific boundary conditions of a given pull and used to solve the continuity equation for the fiber shape. This gave a significant improvement of the modeled shape now qualitatively yielding the right shape in contrary to the model by [Birks *et al.* 1992]. However, for the prediction of vital parameters, such as the nanofiber waist size or the length of the tapers, the model performance was far from good

enough. We found the discrepancy to be caused by an invalid assumption of time-independent fiber flow.

In order to include the time-dependency in the velocity profile it is necessary to consider the fluid dynamical properties of the fiber. Starting from the Navier-Stokes equations we imposed the fiber pulling boundary conditions to obtain an approximate solution of the fiber motion. From this we could derive the now time-dependent longitudinal velocity profile of the fiber. This solution together with the continuity equation could now be solved to yield the fiber shape provided a known function of the viscosity exists. We showed that the viscosity can be inferred by assuming the velocity profile to be stationary in time for small elongation lengths of the fiber. This allowed us infer the velocity for this small pull using the method developed for modeling the fiber shape under the time-independent approximation for the model. The inferred function for the viscosity could now be inserted in the two main equations for the fiber shape; the axial shape-dependent velocity profile and the continuity equation. With this we obtained results for the modeled shape in very good agreement with the measured diameters of various fibers pulled under different boundary conditions. This model for the fiber shape is generalized to all times and axial positions along the fiber. It is therefore not limited to any specific pulling procedures, such as symmetric pulls or "push-pulls". This generally the case as other pull conditions can be obtained by stopping the pull and restart it with new boundary conditions that should then enter the model. In this scheme of making several consecutive pulls of the same fiber the shape can be modeled for any boundary conditions of axially pulling procedures.

Chapter 10

Outlook and perspectives

With a model capable of reproducing the shape of tapered nanofibers we are ready to take the next steps towards a light-atom quantum interface. In this chapter the future plans for making and applying nanofibers as a light-atom quantum interface are presented. In Sec. 10.1 the main interest will be put in the future development of the nanofibers themselves with focus on future application in quantum optics experiments. However, most of the considerations are relevant for other applications as well and this section thus provides a general discussion of future refinements of the nanofibers. In Sec. 10.2 we will turn to the more specific case of using the nanofibers as a light-atom interface and how we plan to implement this.

10.1 Next generation nanofibers

To use the nanofibers as a light-atom interface we need to optimize some of the parameters discussed in this work as well as explore more properties of the nanofibers. In the following we discuss how this will be carried out.

Designing fibers We have shown that we can predict the fiber shape after pulling using given boundary conditions of the initial fiber shape and the pull speeds. The next step is of course to obtain which boundary conditions are required to pull a desired shape of the nanofiber. In [Baker *et al.* 2011] they take the naive approach and apply Eq. (8.36); $\tilde{d}_w/d_0 = \sqrt{v_-/v_+}$, to obtain the ratio of the "push-pull" speeds needed to obtain the shape $\tilde{d}_w$. This is not only limited to these specific pulls but also fails in predicting the right settings of $v_\pm$ for a single pull. However, many consecutive pulls of the same fiber wash out the discrepancy between the designed shape and the produced shape. Making the approach fairly applicable. We would like to first test the same algorithm for designing the fiber shapes using it together with the generalized flow model presented in this work. Depending on the results of the designed shape versus the simulated and measured shape, we will have to consider if this naive approach can be improved further.

Adiabatic tapers In order to make the nanofiber more adiabatic, and thus increase its transmission, we need to improve the mode coupling between the unpulled fiber and the nanofiber. The task is twofold. The main loss of light was inferred to be caused by the excitation of the HE_{12} mode. In order to prevent this the adiabatic criteria discussed in Sec. 2.3.1 should be employed. We therefore plan to calculate the optimal fiber shape from the adiabatic criteria. Using this shape in the above algorithm would let us obtain the required settings of the boundary conditions needed to produce

the desired fiber. In reality we probably to not want the fiber shape solely predicted by the adiabatic transition. Depending on the application of the nanofiber a trade-off between adiabatic tapers and requirements for the waist size or other spatial parameters of the fiber might be necessary. In Sec. 4.2.2 we saw that the fibers start to bend when pulled thinner than about 10 μm. This means that higher order cladding modes with different azimuthal symmetry than the fundamental mode can be excited as observed in Sec. 4.1 causing additional losses at the tapers. Apart from applying the adiabatic criteria we should therefore also try to get rid of this effect. One possible solution might be to change the fiber mounts, as we have observed the V-grooves to be rather coarse which could be the origin of the transverse tension in the fibers causing them to bend.

Thermal properties For future use as light-atom interfaces we need to test the thermal properties of the nanofibers. One purpose is to observe how much power the nanofibers can withstand in vacuum. This can be acquired by simply increasing the power through the nanofiber until it breaks. Another purpose is to obtain the thermal expansion which induces a change in the optical path length, extensively studied in [Wuttke *et al.* 2013]. Placing the nanofiber in one arm of a Mach-Zehnder interferometer the change in optical path length can be detected by performing a differential homodyne measurement. With the nanofiber setup we currently have, a significant thermal expansion of the fiber of tens of micrometers has been observed already for a few milliwatts of transmitted power. For the two-color trapping scheme roughly 20 mW of power is required. Thermal effects of the nanofiber can therefore be expected to play a significant role in the probed results and should be well understood.

Looped resonators Although the nanofibers already provide an interface for strongly coupled light and atoms it can be further improved by placing it inside an optical resonator. This can be achieved in several ways. In the group of Rauschenbeutel they have obtained a $\mathcal{F} \approx 85$ finesse Fabry-Pérot cavity formed around the nanofiber by making two Bragg gratings in the fiber before tapering. From this they predicted that the strong coupling regime can be reached [Wuttke *et al.* 2012]. Another method would be to create a ring-resonator by looping the nanofibers. Here [Sumetsky *et al.* 2006] obtained a finesse of $\mathcal{F} \approx 40$ by bending the fiber such that the two tapered sections lie on top of each other. This constitutes a relatively stable loop held together by Van der Waals and electrostatic forces. Light can thus either propagate into the loop or couple directly into the other taper through the evanescent field. It is noteworthy that both solutions still yields an all-integrated and scalable system of "fiber-coupled atoms".

10.2 Light-atom quantum interface

Besides making the nanofibers ourselves we are currently realizing a setup using a nanofiber brought from Raushenbeutel's group. A magneto-optical trap (MOT) has been implemented and the two-color trap as well as a dispersive probing scheme inspired by [Lodewyck *et al.* 2009] are being setup[1]. With the knowledge and experience gained through this work we plan to use the nanofibers in a next generation setup. This is described in the following together with a list of main

[1]Mainly lead by Jean-baptiste Béguin and Eva Bookjans.

applications for the quantum interface between light and atoms provided by the nanofiber.

Quantum optics on a chip So far a nanofiber is usually placed, with great success, inside an ordinary MOT from where the atoms are loaded into the two-color fiber-based trap. [Vetsch *et al.* 2010; Goban *et al.* 2012]. We plan to extend this scheme by using a mirror MOT on a chip [Reichel *et al.* 2011]. Using a high-reflective plate a dipole trap can be established in the vicinity of the plate-vacuum interface by a double reflection from a single laser beam. The magnetic trap can be obtained by integrating a small U-shaped electrical circuit inside the plate providing a magnetic field above the plate. Together with an applied constant magnetic field this can create a minimum trapping potential for the atoms. With this system it is possible to place more than one nanofiber on the plate taking great advantage of their inherent small sizes. This offers a scalable all-integrated system ideal for realizing quantum networks [Cirac *et al.* 1997].

Quantum information With the atomic ensemble being an integrated part of an optical fiber the route to interactions between atomic ensembles is an obvious one to take. Quantum teleportion schemes between two atomic ensembles have already been carried out in our group [Krauter *et al.* 2013]. With this experience it is natural to extend the scheme for the atomic nanofiber-based trap as well. It is furthermore expected that the scalability provided by the nanofiber can extend the scheme to more than two atomic ensembles [Choi *et al.* 2010].

Exotic quantum states Besides from working with nanofibers we also have a setup consisting of a dipole trapped atomic ensemble placed in one arm of a Mach-Zehnder interferometer. With this setup we are implementing the creation of a non-classical state in the atomic ensemble [Kiesel *et al.* 2012]. For this projection noise limited measurements are a requirement. Classical noise scales quadratically with the number of atoms and quantum state engineering would therefore benefit from using smaller atomic ensembles. This can readily be achieved using nanofiber-based traps where [Goban *et al.* 2012] obtained optical depths above 60 for less than 1000 atoms. In contrast we need around 10^5 atoms in the dipole setup to achieve comparable optical depths.

Hybrid systems Quantum interactions mediated by light are also a promising prospect of the nanofibers. Having "fiber-coupled atoms", quantum interactions with other systems over a distance should be readily achievable. Such other quantum systems could be quantum dots, mechanical resonators, electrical resonators, or NV centers in diamonds, just to mention a few [Xiang *et al.* 2013].

Appendices

Appendix A

Oven circuit diagram

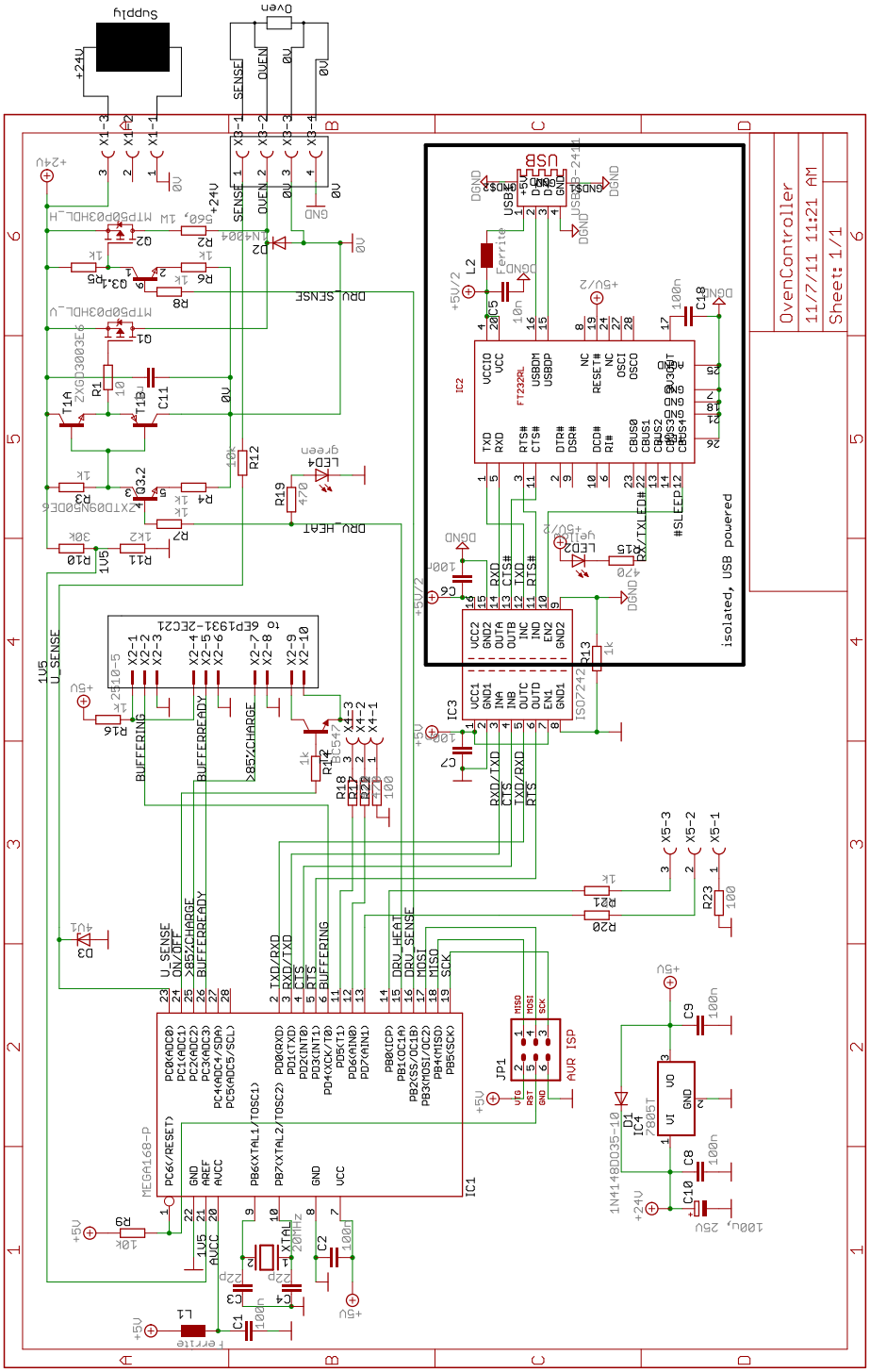

Appendix B

CCD imaging error analysis

B.1 The longitudinal conversion factor

We start by calculated the uncertainty on the longitudinal conversion factor, Eq. (4.6):

$$c_l = \frac{Ns}{N(w_i - o)} = \frac{x}{N(w_i - o)}\,, \tag{B.1}$$

where N is the number of images used to record the fiber, $s = 0.1$ mm is the distance the fiber is moved between each image, $w_i = 768$ pixels is the width of a single image, $o = 217$ pixels is the overlap of the images, and $x = Ns$ is the total length the fiber was moved during the imaging. There is no uncertainty on the number of images taken or the image width, from the error propagation formula for uncorrelated errors we therefore obtain:

$$\sigma_{c_l}^2 = \left(\frac{\partial c_l}{\partial x}\right)^2 \sigma_x^2 + \left(\frac{\partial c_l}{\partial o}\right)^2 \sigma_o^2 \tag{B.2a}$$

$$= \left(\frac{1}{N(w_i - o)}\right)^2 \sigma_x^2 + \left(\frac{x}{N(w_i - o)^2}\right)^2 \sigma_o^2 \tag{B.2b}$$

$$= c_l^2 \left(\frac{\sigma_x}{x}\right)^2 + \left(\frac{c_l}{w_i - o}\right)^2 \sigma_o^2\,. \tag{B.2c}$$

Using $N = 300$ for the fiber in Fig. 4.10, $\sigma_x = \pm 10$ μm from the stage specs, and an estimated error on the overlap $\sigma_o = \pm 1$ pixel, this gives $\sigma_{c_l} = 0.001$ μm/pixel. Note that the uncertainty on the longitudinal conversion factor increases for smaller travel lengths of the stage, however the dominating error is given by the second term, so even for small distances (1 mm) the uncertainty stays unchanged. Since both the imaging and the pulling is always done over tens of millimeters the uncertainty on c_l thus effectively stays unchanged.

B.2 The diameter

The measured diameter of the fiber is given by:

$$d = c_t w\,, \tag{B.3}$$

for the transverse conversion factor c_t and the measured width in pixels w. Where c_t is given by:

$$c_t = \frac{d_0}{\sqrt{A_0}}\,, \tag{B.4a}$$

$$A_0 = \frac{\int_{z_1}^{z_2} w^2(z)\,\mathrm{d}z}{z_2 - z_1 - l/c_l}\,. \tag{B.4b}$$

Here $d_0 = 125 \pm 2$ μm is the un-pulled fiber diameter, l is the total elongation length, and z_1 and z_2 are points on the fiber axis that have to be chosen outside the tapered range of the fiber. We note that c_t and w are not independent variables and therefore rewrite the diameter:

$$d = d_0 \frac{w}{\left(\int_{z_1}^{z_2} \widetilde{w}^2(z)\,\mathrm{d}z\right)^{1/2}} \left(z_2 - z_1 - l/c_1\right)^{1/2} . \tag{B.5}$$

Using the error propagation formula we find for the uncertainty on the measured diameter:

$$\sigma_d^2 = \left(\frac{\partial d}{\partial d_0}\right)^2 \sigma_{d_0}^2 + \left(\frac{\partial d}{\partial w}\right)^2 \sigma_w^2 + \left(\frac{\partial d}{\partial l}\right)^2 \sigma_l^2 + \left(\frac{\partial d}{\partial c_1}\right)^2 \sigma_{c_1}^2 \tag{B.6a}$$

$$\begin{aligned} &= d^2 \left(\frac{\sigma_{d_0}}{d_0}\right)^2 \\ &+ \left(c_t + \frac{d \int_{z_1}^{z_2} w\,\mathrm{d}z}{\int_{z_1}^{z_2} w^2\,\mathrm{d}z}\right)^2 \sigma_w^2 \\ &+ \left(\frac{d}{2c_1(z_2 - z_1 - l/c_1)}\right)^2 \sigma_l^2 \\ &+ \left(\frac{dl}{2c_1(z_2 - z_1 - l/c_1)}\right)^2 \left(\frac{\sigma_{c_1}}{c_1}\right)^2 . \end{aligned} \tag{B.6b}$$

The measured width in pixels w is found from the detected edges. Estimating the error on the edge detection to be; $\sigma_e = \pm 5$ pixels, gives the propagating error on w; $\sigma_w = \sqrt{2}\sigma_e$. For the pull length we use the fiber shown in Fig. 4.10 where we have $l = 15.00 \pm 0.01$ mm with the uncertainty given by the stage specs. For decreasing diameters the uncertainty grows on the detected edges due to

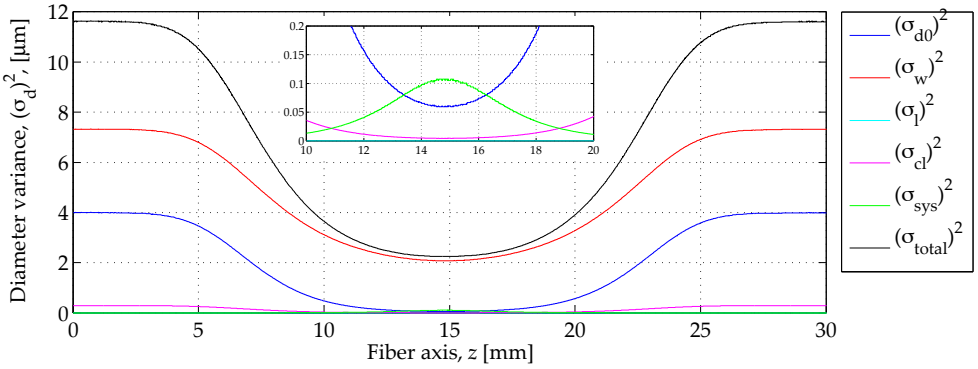

Figure B.1: *Different contributions to the variance of the diameter for the fiber shown in Fig. 4.10. The inset shows a zoom in the y-axis from $z = 10$ mm to $z = 20$ mm.*

systematic errors σ_{sys}. This is included in the error analysis by choosing σ_{sys} to scale inversely proportional with the diameter; $\sigma_{sys} = \kappa/d$, where κ is chosen such that the systematic error is 1 μm at $d = 1$ μm; $\kappa = 1$ μm^2. The total variance on the measured diameter in SI units is thus given by:

$$\sigma_d^2 = \sigma_{\text{prop}}^2 + \sigma_{\text{sys}}^2 \tag{B.7}$$

In Fig. B.1 we show the different contribution of the errors to the total error. The main contribution to the uncertainty in the measured diameter comes from the estimated error on the detected edges σ_w and the inherent error in the fiber diameter σ_{d_0}. With this we obtain the errorbars as shown in Fig. 4.15.

B.3 The transverse conversion factor

The transverse conversion factor is given by:

$$c_\mathrm{t} = \frac{d}{w} = \frac{d_0}{\left(\int_{z_1}^{z_2} \widetilde{w}^2(z)\,\mathrm{d}z\right)^{1/2}} \left(z_2 - z_1 - l/c_\mathrm{l}\right)^{1/2} . \tag{B.8}$$

Using the error propagation formula for uncorrelated errors this yields the uncertainty on c_t:

$$\sigma_{c_\mathrm{t}}^2 = \left(\frac{\partial c_\mathrm{t}}{\partial d_0}\right)^2 \sigma_{d_0}^2 + \left(\frac{\partial c_\mathrm{t}}{\partial w}\right)^2 \sigma_w^2 + \left(\frac{\partial c_\mathrm{t}}{\partial l}\right)^2 \sigma_l^2 + \left(\frac{\partial c_\mathrm{t}}{\partial c_\mathrm{l}}\right)^2 \sigma_{c_\mathrm{l}}^2 \tag{B.9a}$$

$$\begin{aligned} &= \left(\frac{1}{w}\right)^2 \left(\frac{\partial d}{\partial d_0}\right)^2 \sigma_{d_0}^2 \\ &+ \left(c_\mathrm{t} \frac{\int_{z_1}^{z_2} w\,\mathrm{d}z}{\int_{z_1}^{z_2} w^2\,\mathrm{d}z}\right)^2 \sigma_w^2 \\ &+ \left(\frac{1}{w}\right)^2 \left(\frac{\partial d}{\partial l}\right)^2 \sigma_l^2 \\ &+ \left(\frac{1}{w}\right)^2 \left(\frac{\partial d}{\partial c_\mathrm{l}}\right)^2 \sigma_{c_\mathrm{l}}^2 , \end{aligned} \tag{B.9b}$$

where all the differentials can be re-used from σ_d in Appendix B.2.

Appendix C

Stationary velocity profile

C.1 Determining $\mathcal{F}$

Assuming a stationary longitudinal velocity profile; $\frac{\mathrm{d}}{\mathrm{d}t}v(z,t) = 0$, the general solution of the continuity equation is given by Eq. (7.2):

$$\widetilde{A}(z,t) = \frac{1}{v(z)}\,\widetilde{\mathcal{F}}\left(\int_{z_0}^{z}\frac{1}{v(\zeta)}\,\mathrm{d}\zeta - t\right). \tag{C.1}$$

With no loss of generality we start by rewriting Eq. (C.1):

$$A(z,l) = A_0\,\frac{v_\infty}{v(z)}\,\mathcal{F}\left(\int_{z_0}^{z}\frac{v_\infty}{v(\zeta)}\,\mathrm{d}\zeta - l\right), \tag{C.2a}$$

with:

$$\mathcal{F}(x) = \frac{1}{v_\infty A_0}\widetilde{\mathcal{F}}\left(\frac{x}{v_\infty}\right), \tag{C.2b}$$

and:

$$A(z,l) = \widetilde{A}(z, v_\infty t)\,. \tag{C.2c}$$

It is now given in terms of the more relevant variable; $l = v_\infty t$, for the total elongation length of the fiber. By imposing the boundary condition of an initially uniform fiber; $A(z,0) = A_0$, $\mathcal{F}$ can determined. To show this we start by introducing a new variable:

$$q(z) \equiv \int_{z_0}^{z}\frac{v_\infty}{v(\zeta)}\,\mathrm{d}\zeta\,, \tag{C.3}$$

where:

$$q'(z) \equiv \frac{\mathrm{d}q}{\mathrm{d}z} = \frac{v_\infty}{v(z)}\,. \tag{C.4}$$

Eq. (C.2a) can then be rewritten to:

$$\frac{A(z,l)}{A_0} = q'(z)\mathcal{F}\big(q(z) - l\big)\,. \tag{C.5}$$

Now, we define B such that $B' = \mathcal{F}$:

$$\frac{A(z,l)}{A_0} = \frac{\partial}{\partial z}B\big(q(z) - l\big)\,. \tag{C.6}$$

Imposing the condition that the fiber-cross sectional area is initially uniform and only changes for $l \neq 0$, we must have:

$$\frac{A(z,0)}{A_0} = 1 \quad \Rightarrow \quad \frac{\mathrm{d}}{\mathrm{d}z}B\big(q(z)\big) = 1\,. \tag{C.7}$$

Therefore; $B(q) = z$, up to an arbitrary constant, and we recognize B as the inverse function of $q(z)$; $B = q^{-1}$. Finally, we obtain the general solution for the cross-sectional area of the fiber:

$$A(z,l) = A_0 \frac{\partial}{\partial z} q^{-1}\big(q(z) - l\big)\,, \tag{C.8}$$

as can be directly verified by inserting it into the continuity equation.

Here we obtained $A(z,l)$ in the limiting case where the initial fiber shape is uniform. A more general expression can be obtained by letting the initial fiber shape be a non-uniform function of the axial position; $A_0(z)$,. This is given by:

$$A(z,l) = A_0\big(y(z,l)\big) \frac{\partial}{\partial z} y(z,l)\,. \tag{C.9}$$

with $y(z,l) \equiv q^{-1}\big(q(z) - l\big)$. From this the model can be applied to more than one pull of the same fiber. Again, this expression can be directly verified by inserting it into the continuity equation.

C.2 Deriving the recursion formula for $v(z)$

Starting from the general solution of the continuity equation for a stationary velocity profile, see Appendix C.1:

$$A(z,l) = A_0 \frac{\partial}{\partial z}\Big(q^{-1}\big(q(z) - l\big)\Big)\,, \tag{C.10a}$$

$$q(z) \equiv \int_{z_0}^{z} \frac{v_\infty}{v(\zeta)}\,\mathrm{d}\zeta\,, \tag{C.10b}$$

we want to invert it to yield a solution for the velocity profile of the fiber flow inside the hot zone, $z_- < z < z_+$. Outside the hot zone the velocity is known, such that we have:

$$v(z) = \begin{cases} v_- & \text{if } z \le z_-, \\ ? & \text{if } z_- < z < z_+, \\ v_+ & \text{if } z_+ \le z. \end{cases}$$

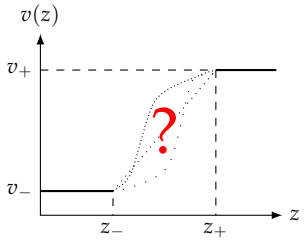

We rewrite Eq. (C.10a) for the fiber cross-sectional area by integrating it from z_x to z:

$$\int_{z_x}^{z} \frac{A(\zeta,l)}{A_0}\,\mathrm{d}\zeta = q^{-1}\big(q(z) - l\big) - q^{-1}\big(q(z_x) - l\big)\,, \tag{C.11}$$

for arbitrary z_x. If we choose $z_x = z_+ + v_+ t = z_+ + l_+$, and $z_0 = z_+$ in Eq. (C.10b), the integral in $q(z_x)$ will only be over constant velocities, since $v(z > z_+) = v_+$, and we get $q(z_x) = l$. From the definition of an inverse function, $q^{-1}\big(q(z)\big) = z$, the second term on the RHS in Eq. (C.11) will then be given by:

$$q^{-1}\big(q(z_x) - l\big) = q^{-1}(0) = z_+\,, \tag{C.12}$$

and Eq. (C.11) can be simplified to:

$$y(z,l) \equiv q^{-1}\big(q(z) - l\big) = \int_{z_+ + l_+}^{z} \frac{A(\zeta,l)}{A_0}\,\mathrm{d}\zeta + z_+\,. \tag{C.13}$$

We now apply $q(\cdot)$ on both sides of the first equality and take the derivative with respect to z:

$$q'\big(y(z)\big)\, y'(z) = q'(z)\,. \tag{C.14}$$

Finally, we use $q'(z) = \frac{v_\infty}{v(z)}$ from the definition of q and obtain the recursion formula:

$$v\big(y(z)\big) = \frac{A(z,l)}{A_0} v(z)\,. \tag{C.15}$$

C.3 Applying the recursion formula for $v(z)$

Here we describe the algorithm used to obtain $v(z)$ from the recursion formula.

We start by choosing a point on the fiber at a position $\tilde{z}$, far outside the hot zone, such that $v(\tilde{z}) = v_+$, as shown in Fig. C.1. This is Step 1 in the algorithm, see Table C.1. "Method" refers to how the entries for $v(z)$ is obtained and Method I is thus the initialization of the algorithm.

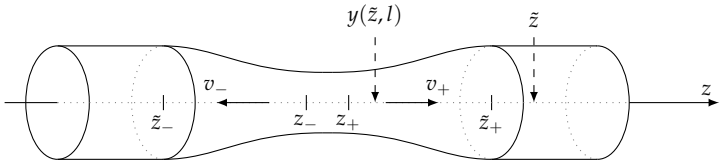

Figure C.1: *Sketch illustrating how far the point $y(\tilde{z},l)$, of the up-pulled fiber, has moved after elongating the fiber by $l = v_\infty t$. The new point is denoted by $\tilde{z}$.*

In Step 2 Eq. (C.13) is applied to obtain $y(\tilde{z},l)$ as the new z-value. Using the recursion formula (C.15), $v\big(y(\tilde{z},l)\big)$ is calculated. Here it is important that $\tilde{z}$ has been chosen sufficiently far away from the hot zone, such that $y(\tilde{z},l)$ is also outside the hot zone yielding the same value for $v\big(y(\tilde{z},l)\big)$ as for $v(\tilde{z})$:

$$y(\tilde{z},l) > z_+ \quad \Rightarrow \quad v\big(y(\tilde{z},l)\big) = v(\tilde{z}) = v_+\,. \tag{C.16}$$

This can be ensured if $\tilde{z} > \tilde{z}_+$ as seen from Eq. (C.13) where we find;

$$y(\tilde{z} > \tilde{z}_+, l) = \int_{z_+ + l_+}^{\tilde{z}} \frac{A(\zeta,l)}{A_0}\,\mathrm{d}\zeta + z_+ = \tilde{z} - l_+ > z_+\,. \tag{C.17}$$

After obtained $v\big(y(\tilde{z},l)\big)$ Table C.1 is sorted according to the z-values. Applying the recursion formula and sorting the z-values are thus referred to as Method II. In step 3 we decrease z by a small amount δz. Using `interp1` in MATLAB

Table C.1: *Algorithm for obtaining $v(z)$ from the "+" side.*

Step	Method	z	$v(z)$
1	I	$\tilde{z}$	$v(\tilde{z}) = v_+$
2	II	$y(\tilde{z})$	$v\big(y(\tilde{z})\big)$
3	III	$\tilde{z} - \delta z$	$v(\tilde{z} - \delta z)$
4	II	$y(\tilde{z} - \delta z)$	$v\big(y(\tilde{z} - \delta z)\big)$

we infer $v(\tilde{z} - \delta z)$ by linearly interpolating the entries of z and $v(z)$ in Table C.1. This is referred to as Method III. In Step 4 Method II is repeated. That is, a new z-value is calculated by applying Eq. (C.13) on the value of z used in the previous step; $y(\tilde{z} - \delta z)$. Thereafter $v\big(y(\tilde{z} - \delta z)\big)$ is calculated using Eq. (C.15) and the

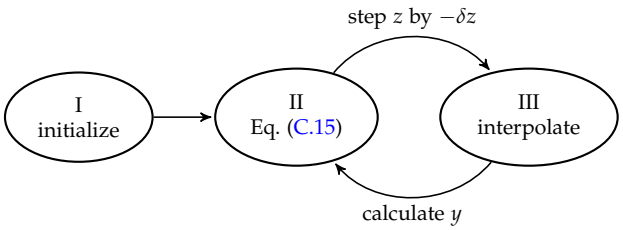

Figure C.2: *Recursion algorithm for obtaining $v(z)$ from the "+" side.*

table is then sorted according to the z-values. The methods III and II are now cycled to yield Steps 5 and 6, 7 and 8, *etc.*, see Fig. C.2. When $y(z-\delta z) > z$ or no more data points are available the procedure is stopped.

We have here shown how to apply the recursion formula from the "+" side, *i.e.*, when starting the algorithm with a point $\tilde{z} > \tilde{z}_+$. The analysis can of course also be applied from the "-" side. This is, *e.g.*, necessary for symmetric pulls where;

$$y(z,l) > z \text{ if } z < z_c, \tag{C.18a}$$
$$y(z,l) < z \text{ if } z > z_c, \tag{C.18b}$$

for the hot zone center z_c, see Sec. 7.1.1. In order do apply the recursion formula from the "-" side it becomes necessary to invert the y-function to obtain $z(y,l)$. This is easy to do numerically and from here the analysis follows the above recipe.

Appendix D

Fluid mechanics

D.1 Symmetric stress tensor

To see that the stress tensor σ must be symmetric due to angular momentum conservation we consider a uniform rotation of the fluid. In this case no internal friction is present and the shear stress must vanish, *i.e.*, we have $\sigma_{ij} = 0$ for $i \neq j$. The most general shear stress tensor can therefore be composed of the linear combination;

$$\sigma_{ij} = \eta(\partial_j u_i + \partial_i u_j)\,, \tag{D.1}$$

since these elements vanish for a uniform rotation, where; $\mathbf{u} = \boldsymbol{\omega} \times \mathbf{x}$ for the angular frequency $\boldsymbol{\omega}$. We thus have:

$$u_i = \omega_j x_k - \omega_k x_j\,. \tag{D.2a}$$

$$\Rightarrow \quad \partial_j u_i + \partial_i u_j = -\omega_k + \omega_k = 0\,. \tag{D.2b}$$

D.2 Incompressible fluid

We want to show that an incompressible fluid necessarily means; $\nabla \cdot \mathbf{u} = 0$. We consider the mass current flowing into and/or out of an enclosed volume V with surface element $\mathrm{d}\mathbf{S}$:

$$i_m = -\oint_S \varrho \mathbf{u} \cdot \mathrm{d}\mathbf{S}\,. \tag{D.3}$$

The negative sign corresponds to a negative change in mass which is the case if the mass flow through the surface is positive; $\mathbf{u} \cdot \mathrm{d}\mathbf{S} > 0$. The total mass inside the volume is given by:

$$m = \int_V \varrho \mathrm{d}V\,. \tag{D.4}$$

The rate of change of mass in V is of course equal to the mass current:

$$\frac{\partial m}{\partial t} = i_m\,. \tag{D.5}$$

If the fluid is incompressible then the mass density must be constant and ϱ can be taken out of the integral in Eq. (D.4); $m = \varrho V$. Inserting Eq. (D.3) and Eq. (D.4) into Eq. (D.5) and taking the limit of $V \to 0$ therefore gives:

$$\frac{\mathrm{d}\rho}{\mathrm{d}t} = \lim_{V \to 0} \left(\frac{1}{V} \oint_S \rho \mathbf{u} \cdot \mathrm{d}\mathbf{S} \right) = -\nabla \cdot \mathbf{u}\,, \tag{D.6}$$

where the last equality follows from the definition of the divergence operator [Riley *et al.* 2006, p. 398]. Since $\mathrm{d}\varrho/\mathrm{d}t = 0$ we thus obtain $\nabla \cdot \mathbf{u} = 0$.

D.3 Derivation of the u_ρ component

We want to derive u_ρ in Eq. (8.18):

$$u_\rho(\rho, z) = -u_0'(z)\frac{\rho}{2} - u_2'(z)\frac{\rho^3}{4} + \mathcal{O}(\rho^4). \tag{D.7}$$

We start by Taylor expanding u_ρ and u_z in ρ about the fiber axis $\rho = 0$:

$$u_\rho = u_{\rho,0} + u_{\rho,1}\rho + u_{\rho,2}\rho^2 + u_{\rho,3}\rho^3 + u_{\rho,4}\rho^4\,, \tag{D.8a}$$
$$u_z = u_0(z) + u_2(z)\rho^2\,. \tag{D.8b}$$

This we now want to insert in Eq. (8.14c):

$$0 = \left(\frac{1}{\rho} + \partial_\rho\right)u_\rho + \partial_z u_z\,, \tag{D.9a}$$
$$\Rightarrow \quad u_\rho + \rho\partial_\rho u_\rho = -\rho\partial_z u_z\,. \tag{D.9b}$$

Noting that $\rho\partial_\rho u_\rho = u_\rho - u_{\rho,0}$ we have to third order in ρ:

$$u_{\rho,0} + 2u_{\rho,1}\rho + 3u_{\rho,2}\rho^2 + 4u_{\rho,3}\rho^3 = -u_0'\rho - u_2'\rho^3\,, \tag{D.10}$$

and equating terms with the same order in ρ we find:

$$\mathcal{O}(\rho^0): \qquad u_{\rho,0} = 0\,, \tag{D.11a}$$
$$\mathcal{O}(\rho^1): \qquad u_{\rho,1} = -\frac{u_0'}{2}\,, \tag{D.11b}$$
$$\mathcal{O}(\rho^2): \qquad u_{\rho,2} = 0\,, \tag{D.11c}$$
$$\mathcal{O}(\rho^3): \qquad u_{\rho,3} = -\frac{u_2'}{4}\,. \tag{D.11d}$$

Inserting the coefficients into Eq. (D.8a) we thus obtain Eq. (D.7).

D.4 Derivation of the diffential equation for u_0

Here we show the derivation of Eq. (8.23):

$$0 = 3\frac{(\eta r^2 u_0')'}{r^2}\,. \tag{D.12}$$

We start by inserting the Taylor expansions of the pressure and velocity field Eq. (8.18) and Eq. (8.20):

$$u_\rho(\rho, z) = -u_0'(z)\frac{\rho}{2} - u_2'(z)\frac{\rho^3}{4}\,, \tag{D.13a}$$
$$u_z(\rho, z) = u_0(z) + u_2(z)\rho^2\,, \tag{D.13b}$$
$$p(\rho, z) = p_0(z) + p_2(z)\rho^2\,. \tag{D.13c}$$

into the z-component of the equation for Stokes flow (8.14b):

$$0 = \left(\eta\partial_\rho^2 + \eta\partial_z^2 + \eta'\partial_z + \frac{\eta}{\rho}\partial_\rho\right)u_z - \eta'\partial_\rho u_\rho - \frac{\eta'}{\rho}u_\rho - \partial_z p\,. \tag{D.14}$$

This yields:

$$\begin{aligned} 0 &= 4\eta u_2 + 2\eta' u_0' + 2\eta'\rho^2 u_2' - p_0' + \eta u_0'' + \eta\rho^2 u_2'' - \rho^2 p_2' \\ &\overset{\mathcal{O}(\rho)}{\approx} 4\eta u_2 + 2\eta' u_0' - p_0' + \eta u_0''\,. \end{aligned} \tag{D.15}$$

To eliminate u_2 and p_0 from this expression, such that it only contains terms of u_0 or its derivatives, we insert the approximations (8.22b) and (8.21b):

$$u_2 \approx \frac{1}{2r}\left(3r'u_0' + \frac{1}{2}ru_0''\right), \tag{D.16a}$$

$$p_0 \approx -\eta u_0', \tag{D.16b}$$

into the approximative z-component of the Stokes flow Eq. (D.15). This yields:

$$0 = 4\eta u_2 + 2\eta' u_0' - p_0' + \eta u_0'' \tag{D.17a}$$

$$= 6\frac{\eta r' u_0'}{r} + 3\eta' u_0' + 3\eta u_0'' \tag{D.17b}$$

$$= 3\frac{(\eta r^2 u_0')'}{r^2}. \tag{D.17c}$$

Bibliography

[Alton *et al.* 2010] D. J. Alton, N. P. Stern, T. Aoki, H. Lee, E. Ostby, K. J. Vahala, and H. J. Kimble (2010). Strong interactions of single atoms and photons near a dielectric boundary. *Nature Physics* **7.2**, pp. 159–165. DOI: 10.1038/nphys1837.

[Appel *et al.* 2009] J. Appel, P. J. Windpassinger, D. Oblak, U. B. Hoff, N. Kjærgaard, and E. S. Polzik (2009). Mesoscopic atomic entanglement for precision measurements beyond the standard quantum limit. *Proceedings of the National Academy of Sciences* **106.27**, pp. 10960–10965. DOI: 10.1073/pnas.0901550106.

[Bahl *et al.* 2013] G. Bahl, K. H. Kim, W. Lee, J. Liu, X. Fan, and T. Carmon (2013). Brillouin cavity optomechanics with microfluidic devices. *Nature Communications* **4**, pp. 1–6. DOI: 10.1038/ncomms2994.

[Baker *et al.* 2011] C. Baker and M. Rochette (2011). A generalized heat-brush approach for precise control of the waist profile in fiber tapers. *Optical Materials Express* **1.6**, pp. 1065–1076.

[Balykin *et al.* 2004] V. I. Balykin, K. Hakuta, F. Le Kien, J. Q. Liang, and M. Morinaga (2004). Atom trapping and guiding with a subwavelength-diameter optical fiber. *Phys. Rev. A* **70.011401** (1), p. 011401. DOI: 10.1103/PhysRevA.70.011401.

[Birks *et al.* 1992] T. A. Birks and Y. W. Li (1992). The shape of fiber tapers. *Journal of Lightwave Technology* **10.4**, pp. 432–438.

[Bojor 2005] L. Bojor (2005). *Fiber modes*. URL: http://www.mathworks.com/matlabcentral/fileexchange/9126-fiber-modes (visited on 08/15/2013).

[Boozer *et al.* 2007] A. Boozer, A. Boca, R. Miller, T. Northup, and H. Kimble (2007). Reversible State Transfer between Light and a Single Trapped Atom. *Physical Review Letters* **98**, p. 193601. DOI: 10.1103/PhysRevLett.98.193601.

[Brambilla 2010] G. Brambilla (2010). Optical fibre nanowires and microwires: a review. *Journal of Optics* **12.4**, p. 043001. DOI: 10.1088/2040-8978/12/4/043001.

[Brambilla *et al.* 2004] G. Brambilla, V. Finazzi, and D. J. Richardson (2004). Ultra-low-loss optical fiber nanotapers. *Optics Express* **12.1**, p. 2258. DOI: 10.1364/OPEX.12.002258.

[Camerer *et al.* 2011] S. Camerer, M. Korppi, A. Jöckel, D. Hunger, T. Hänsch, and P. Treutlein (2011). Realization of an Optomechanical Interface Between Ultracold Atoms and a Membrane. *Physical Review Letters* **107.22**, p. 223001. DOI: 10.1103/PhysRevLett.107.223001.

[Cassany 2009] G. S. Cassany (2009). *Cold atom physics using ultra-thin optical fibres*. PhD thesis. University of Bonn.

[Choi *et al.* 2010] K. S. Choi, A. Goban, S. B. Papp, S. J. van Enk, and H. J. Kimble (2010). Entanglement of spin waves among four quantum memories. *Nature* **468.7322**, pp. 412–416. DOI: 10.1038/nature09568.

[Cirac *et al.* 1997] J. Cirac, P. Zoller, H. Kimble, and H. Mabuchi (1997). Quantum state transfer and entanglement distribution among distant nodes in a quantum network. *Physical Review Letters* **78.16**, pp. 3221–3224.

[Ding *et al.* 2010] L. Ding, C. Belacel, S. Ducci, G. Leo, and I. Favero (2010). Ultralow loss single-mode silica tapers manufactured by a microheater. *Applied Optics* **49.13**, pp. 2441–2445.

[Eggers *et al.* 1994] J. Eggers and T. F. Dupont (1994). Drop formation in a one-dimensional approximation of the Navier-Stokes equation. *Journal of Fluid Mechanics* **262**, pp. 205–221. DOI: 10.1017/S0022112094000480.

[Fan *et al.* 2008] X. Fan, I. M. White, S. I. Shopova, H. Zhu, J. D. Suter, and Y. Sun (2008). Sensitive optical biosensors for unlabeled targets: A review. *Analytica Chimica Acta* **620.1-2**, pp. 8–26. DOI: 10.1016/j.aca.2008.05.022.

[Feynman *et al.* 2010] R. R. P. Feynman, R. B. Leighton, and M. M. L. Sands (2010). *The Feynman Lectures on Physics, Volume II: Mainly Electromagnetism and Matter*. Basic Books. ISBN: 9780465024162.

[Frawley *et al.* 2012] M. C. Frawley, A. Petcu-Colan, V. G. Truong, and S. N. Chormaic (2012). Higher order mode propagation in an optical nanofiber. *Optics Communications* **285.23**, pp. 4648–4654. DOI: 10.1016/j.optcom.2012.05.016.

[Fujiwara *et al.* 2011] M. Fujiwara, K. Toubaru, and S. Takeuchi (2011). Optical transmittance degradation in tapered fibers. *Optics Express* **19.9**, pp. 8596–8601. DOI: 10.1364/OE.19.008596.

[Garcia-Fernandez *et al.* 2011] R. Garcia-Fernandez, W. Alt, F. Bruse, C. Dan, K. Karapetyan, O. Rehband, A. Stiebeiner, U. Wiedemann, D. Meschede, and A. Rauschenbeutel (2011). Optical nanofibers and spectroscopy. *Applied Physics B* **105.1**, pp. 3–15. DOI: 10.1007/s00340-011-4730-x.

[Ghatak *et al.* 1998] A. Ghatak and K. Thyagarajan (1998). *An Introduction to Fiber Optics*. Cambridge University Press. ISBN: 9780521577854.

[Goban *et al.* 2012] A. Goban, K. Choi, D. Alton, D. Ding, C. Lacroûte, M. Pototschnig, T. Thiele, N. Stern, and H. Kimble (2012). Demonstration of a State-Insensitive, Compensated Nanofiber Trap. *Physical Review Letters* **109.3**, p. 033603. DOI: 10.1103/PhysRevLett.109.033603.

[Graf *et al.* 2009] J. C. Graf, S. A. Teston, P. V. de Barba, J. Dallmann, J. Lima, H. J. Kalinowski, and A. S. Paterno (2009). Fiber taper rig using a simplified heat source and the flame-brush technique. *Microwave and Optoelectronics Conference (IMOC), 2009 SBMO/IEEE MTT-S International*, pp. 621–624. DOI: 10.1109/IMOC.2009.5427507.

[Grellier *et al.* 1998] A. J. C. Grellier, N. K. Zayer, and C. N. Pannell (1998). Heat transfer modelling in CO 2 laser processing of optical fibres. *Optics Communications* **152.4**, pp. 324–328.

[Hammerer *et al.* 2010] K. Hammerer, A. S. Sørensen, and E. S. Polzik (2010). Quantum interface between light and atomic ensembles. *Reviews of Modern Physics* **82.2**, pp. 1041–1093. DOI: 10.1103/RevModPhys.82.1041.

[Hecht 2002] E. Hecht (2002). *Optics*. Addison-Wesley Longman, Incorporated. ISBN: 9780805385663.

[Karapetyan 2011] K. Karapetyan (2011). *Optical Fibre Toolbox*. URL: http://www.mathworks.com/matlabcentral/fileexchange/27819-optical-fibre-toolbox (visited on 08/15/2013).

[Kenny *et al.* 1991] R. P. Kenny, T. A. Birks, and K. P. Oakley (1991). Control of optical fibre taper shape. *Electronics letters* **27.18**, pp. 1654–1656.

[Kiesel *et al.* 2012] T. Kiesel, W. Vogel, S. L. Christensen, J.-B. Béguin, J. Appel, and E. S. Polzik (2012). Atomic nonclassicality quasiprobabilities. *Phys. Rev. A* **86** (4), p. 042108. DOI: 10.1103/PhysRevA.86.042108.

[Krauter *et al.* 2013] H. Krauter, D. Salart, C. A. Muschik, J. M. Petersen, H. Shen, T. Fernholz, and E. S. Polzik (2013). Deterministic quantum teleportation between distant atomic objects. *Nature Physics* **9.6**, pp. 1–5. DOI: 10.1038/nphys2631.

[Landau *et al.* 1987] L. D. Landau and E. M. Lifshitz (1987). *Fluid Mechanics, Volume 6 of Course of Theoretical Physics*. 2nd ed. Butterworth Heinemann. ISBN: 9780750627672.

[Lautrup 2011] B. Lautrup (2011). *Physics of Continuous Matter: Exotic and Everyday Phenomena in the Macroscopic World*. 2nd ed. Taylor and Francis. ISBN: 9781420077001.

[Le Kien *et al.* 2004] F. Le Kien, V. I. Balykin, and K. Hakuta (2004). Atom trap and waveguide using a two-color evanescent light field around a subwavelength-diameter optical fiber. *Physical Review A* **70.6**, p. 063403. DOI: 10.1103/PhysRevA.70.063403.

[Lee *et al.* 2011] T. Lee, Y. Jung, C. Codemard, G. Brambilla, and N. G. R. Broderick (2011). Third Harmonic Generation in Silica Microfibres. *Nonlinear Optics, OSA Technical Digest (CD) (Optical Society of America, 2011)*.

[Lee *et al.* 2012] T. Lee, Y. Jung, C. A. Codemard, M. Ding, N. G. R. Broderick, and G. Brambilla (2012). Broadband third harmonic generation in tapered silica fibres. *Optics Express* **20.8**, p. 8503. DOI: 10.1364/OE.20.008503.

[Lodewyck *et al.* 2009] J. Lodewyck, P. G. Westergaard, and P. Lemonde (2009). Nondestructive measurement of the transition probability in a Sr optical lattice clock. *Phys. Rev. A* **79** (6), p. 061401. DOI: 10.1103/PhysRevA.79.061401.

[Love *et al.* 1986] J. D. Love and W. M. Henry (1986). Quantifying loss minimisation in single-mode fibre tapers. *Electronics letters* **22.17**, pp. 912–914.

[Love *et al.* 1991] J. D. Love, W. M. Henry, W. J. Stewart, R. J. Black, S. Lacroix, and F. Gonthier (1991). Tapered single-mode fibres and devices. *IEE Proceedings-J, Optoelectronics* **138.5**, pp. 343–354.

[Martienssen *et al.* 2006] W. Martienssen and H. Warlimont (2006). *Springer Handbook of Condensed Matter and Materials Data*. Springer handbooks. Springer. ISBN: 9783540304371.

[Ovchinnikov *et al.* 1991] Y. B. Ovchinnikov, S. S V, and V. I. Balykin (1991). An atomic trap based on evanescent light waves. *Journal of Physics B: Atomic, Molecular and Optical Physics* **24.14**, pp. 3173–3178.

[Park *et al.* 2009] Y.-S. Park and H. Wang (2009). Resolved-sideband and cryogenic cooling of an optomechanical resonator. *Nature Physics* **5.7**, pp. 489–493. DOI: 10.1038/nphys1303.

[Pricking *et al.* 2010] S. S. Pricking and H. H. Giessen (2010). Tapering fibers with complex shape. *Optics Express* **18.4**, pp. 3426–3437. DOI: 10.1364/OE.18.003426.

[Reichel *et al.* 2011] J. Reichel and V. Vuletic (2011). *Atom Chips*. Wiley. ISBN: 9783527407552.

[Riley *et al.* 2006] K. K. F. Riley, M. P. Hobson, and S. S. J. Bence (2006). *Mathematical Methods for Physics and Engineering*. Cambridge University Press. ISBN: 9780521861533.

[Shi *et al.* 2006] L. Shi, X. Chen, H. Liu, Y. Chen, Z. Ye, W. Liao, and Y. Xia (2006). Fabrication of submicron-diameter silica fibers using electric strip heater. *Optics Express* **14.12**, pp. 5055–5060. DOI: 10.1364/OE.14.005055.

[Snyder *et al.* 1983] A. W. Snyder and J. Love (1983). *Optical Waveguide Theory*. Science Paperbacks, 190. Springer. ISBN: 9780412099502.

[Stiebeiner *et al.* 2010] A. Stiebeiner, R. Garcia-Fernandez, and A. Rauschenbeutel (2010). Design and optimization of broadband tapered optical fibers with a nanofiber waist. *Optics Express* **18.22**, pp. 22677–22685. DOI: 10.1364/OE.18.022677.

[Sumetsky *et al.* 2004] M. Sumetsky, Y. Dulashko, and A. Hale (2004). Fabrication and study of bent and coiled free silica nanowires: Self-coupling microloop optical interferometer. *Optics Express* **12.15**, pp. 3521–3531. DOI: 10.1364/OPEX.12.003521.

[Sumetsky *et al.* 2006] M. Sumetsky, Y. Dulashko, J. M. Fini, A. Hale, and D. J. DiGiovanni (2006). The microfiber loop resonator: theory, experiment, and application. *Journal of Lightwave Technology* **24.1**, pp. 242–250. DOI: 10.1109/JLT.2005.861127.

[Tong *et al.* 2003] L. Tong, R. R. Gattass, J. B. Ashcom, S. He, J. Lou, M. Shen, I. Maxwell, and E. Mazur (2003). Subwavelength-diameter silica wires for low-loss optical wave guiding. *Nature* **426.6968**, pp. 816–819. DOI: 10.1038/nature02193.

[Tong *et al.* 2010] L. Tong and M. Sumetsky (2010). *Subwavelength and Nanometer Diameter Optical Fibers*. Springer-Verlag Berlin Heidelberg.

[Vetsch *et al.* 2010] E. Vetsch, D. Reitz, G. Sagué, R. Schmidt, S. T. Dawkins, and A. Rauschenbeutel (2010). Optical Interface Created by Laser-Cooled Atoms Trapped in the Evanescent Field Surrounding an Optical Nanofiber. *Physical Review Letters* **104.20**, p. 203603. DOI: 10.1103/PhysRevLett.104.203603.

[Ward *et al.* 2006] J. M. Ward, D. G. O'Shea, B. J. Shortt, M. J. Morrissey, K. Deasy, and S. G. Nic Chormaic (2006). Heat-and-pull rig for fiber taper fabrication. *Review of Scientific Instruments* **77.8**, p. 083105. DOI: 10.1063/1.2239033.

[Warken *et al.* 2008] F. Warken, A. Rauschenbeutel, and T. Bartholomäus (2008). Fiber Pulling Profits from Precise Positioning. **42.3**, p. 73.

[Wilk *et al.* 2007] T. Wilk, S. C. Webster, A. Kuhn, and G. Rempe (2007). Single-Atom Single-Photon Quantum Interface. *Science* **317.5837**, pp. 488–490. DOI: 10.1126/science.1143835.

[Wuttke *et al.* 2012] C. Wuttke, M. Becker, S. Brückner, M. Rothhardt, and A. Rauschenbeutel (2012). Nanofiber Fabry-Perot microresonator for nonlinear optics and cavity quantum electrodynamics. *Optics Letters* **37.11**, pp. 1949–1951. DOI: 10.1364/OL.37.001949.

[Wuttke *et al.* 2013] C. Wuttke and A. Rauschenbeutel (2013). Thermalization via heat radiation of an individual object thinner than the thermal wavelength. *Physical Review Letters* **111.2**, p. 024301. DOI: 10.1103/PhysRevLett.111.024301.

[Xiang *et al.* 2013] Z.-L. Xiang, S. Ashhab, J. Q. You, and F. Nori (2013). Hybrid quantum circuits: Superconducting circuits interacting with other quantum systems. *Reviews of Modern Physics* **85.2**, pp. 623–653. DOI: 10.1103/RevModPhys.85.623.

[Xiao *et al.* 2011] Y. Xiao, C. Meng, P. Wang, Y. Ye, H. Yu, S. Wang, F. Gu, L. Dai, and L. Tong (2011). Single-Nanowire Single-Mode Laser. *Nano Letters* **11.3**, pp. 1122–1126. DOI: 10.1021/nl1040308.